

Design and Analysis Techniques for Cavity Beam Position Monitor Systems for Electron Accelerators

Nirav Yashvantray Joshi

Department of Physics
Royal Holloway, University of London




A thesis submitted to the University of London for the degree of Doctor of Philosophy

January, 2013

Declaration of authorship

I, Nirav Yashvantray Joshi, hereby declare that this thesis and the work presented in it is entirely my own. Where I have consulted the work of others, this is always clearly stated.

Signed:  _____

Date: January 21, 2013.

Abstract

Beam position monitors are required in all accelerators for the measurement and optimization of the beam parameters. Cavity beam position monitors (CBPM) offer the possibility of measurement of beam centroid positions at the nanometer scale. These devices can be and typically are used at electron accelerator facilities, both existing light sources and test facilities proposed for future linear colliders, such as the International Linear Collider (ILC) and Compact Linear Collider (CLIC). The requirements for the CLIC main linac are to measure the beam position using approximately 5000 beam position monitors (BPM) with 50 nm resolution, at every 50 ns. The high resolution, enormous scale of the system and the small bunch separation of 0.5 ns present many challenges and demand innovative approaches for the design and operation of the CBPM system. A cylindrical cavity BPM system has been designed in collaboration with the Diamond Light Source, in the C-Band frequency region. The design ideas, which will be beneficial to CLIC BPM and other designs, such as the deliberate separation of modes coupled to the x and y position measurements and the cavity operation without mechanical tuning are tested in the design. The major resonance modes of the cavity are simulated using Eigenmode simulation. The coupling and isolation characteristics are simulated using S -parameter simulations, while the beam coupling is studied through time domain simulations. Four cavities were fabricated according to the design discussed in this thesis. Their coupling and isolation were tested through S -parameter measurements. The dipole modes are separated by more than 5 MHz in frequency. The values of the quality factors were measured using the impedance method. The field orientation of the dipole and quadrupole modes were measured using the bead-pull perturbation technique and found to be rotated by 12° and 3° from

x -axis respectively. The initial beam studies were carried out at the Diamond Light Source and at the ATF2 beam line, and are presented in this thesis. The techniques for position determination of temporally closely spaced bunches are studied. A method was developed to remove the errors in the position determination, due to the overlap of the signals from the previous bunches, by subtracting the decayed phasors from the previous bunch. The method is applied to the signals from the CBPM system on the ATF2 beam line, in the two and three bunch mode operation. The overestimation in position determination of the second bunch is reduced from more than 67% to less than 2%. Position resolution of better than 3 μm is demonstrated for the second bunch. The observed phase difference between the consecutive bunches is studied for different bunch spacing. The performance of the code is verified against simulated data.

Acknowledgments

It gives me immense pleasure to dedicate this thesis to my parents, late Shree Yashvantray Joshi and Shreemati Binduben Joshi, and family members for being the constant source of motivation and support during not only this work, but also my entire life.

I owe my deepest gratitude to my supervisor, Dr. Stewart Boogert, for his guidance, support and his help in development of my technical, scientific thinking and soft skills. This thesis would not have been possible without his guidance, provided through serious conversations at work, as well as informal chit-chats at coffee.

I would like to express my sincere thanks to Prof. Grahame Blair for providing me an opportunity to carry this research at physics department of Royal Holloway, University of London. I feel indebted to Dr. Alexey Lyapin for providing invaluable help and advice during course of this study. I wish to thank Dr. Stephen Molloy (now at ESS, Sweden) and Dr. Pavel Karataev for informative scientific discussions and advice. I am grateful to all my colleague at Royal Holloway for their help and support throughout my stay.

It gives me immense pleasure to acknowledge the scientific inputs and support I received from Dr. Guenther Rehm and Mr. Alun Morgan at the Diamond Light Source in UK, during a collaboration project about development of a CBPM system. The thorough study of CBPM presented in this thesis would not have been possible without their inputs and prompt actions on EM simulations and fabrication of the CBPMs.

I would like to thank all member of ATF, at KEK in Japan, for their support during my stay. I am grateful to Prof. Junji Urakawa for allowing me to carry my experiments at ATF. I offer my special thanks to Prof. Philip Burrows and members of FONT group at JAI at University of Oxford, UK, for providing machine information and support to carry my experiment during their machine shifts on ATF.

I am grateful to Dr. Thibaut Lefevre and Dr. Lars Soby from CERN in Switzerland, Dr. Steve Smith from SLAC in USA, and other members of CLIC main beam cavity BPM collaboration for their scientific inputs and support during my stay at CERN.

I would like to thank my colleagues and friends, Konstantine Lekomtsev, Dr. Maximilian Micheler, Francis Cullinan, William Shields, Robert Ainsworth and Thomas Aumeyr for creating a very live and pleasant working environment during my stay at Royal Holloway.

I would also like to acknowledge the training and funds provided by the DITANET scientific network, under FP7 frame work, which supported me and my visits for research, meetings and various conferences.

Contents

1	Introduction	17
1.1	Particle colliders	18
1.1.1	Synchrotron radiation and limitation on circular collider	19
1.1.2	Linear colliders	20
1.2	Storage rings and free electron lasers as a light source	27
2	Introduction to beam position monitor systems	29
2.1	Diagnostics for beam position measurement	29
2.1.1	Shoe-box BPM	30
2.1.2	Button BPM	31
2.1.3	Stripline BPM	32
2.2	Cavity beam position monitor	33
2.2.1	Theory and working principle	33
2.3	Advantages and applications of cavity BPMs	41
2.3.1	Beam based alignment	43
2.4	Overview of research chapters	43
3	Cavity BPM system for CLIC main linac	46
3.1	Frequency regions for CBPM design and electronic signal processing	47
3.2	Effect of CBPM frequency on bunch train signal	50
3.2.1	Design challenges	53
4	Multi-bunch signal processing	55
4.1	Accelerator Test Facility	56

4.1.1	Operation of the ATF in multi-train mode	58
4.2	Cavity BPM system at ATF2	58
4.2.1	Signal processing	60
4.2.2	Effect of temperature change on CBPM frequency	73
4.3	Signal simulation and calibration code	74
4.4	CBPM signal from multiple bunches and signal subtraction	76
4.4.1	Application of the algorithm on two bunch signals	80
4.4.2	Signal subtraction for three bunches	95
4.5	Summary	100
5	Cavity BPM with pre-aligned and separated dipole modes	101
5.1	Next Light Source	102
5.2	Diamond Light Source	102
5.2.1	Machine information	103
5.3	Cavity BPM design and EM simulations	105
5.3.1	Software packages for EM simulations and post-processing	106
5.3.2	Resonant cavity	109
5.3.3	Waveguide adapter with coaxial coupler	114
5.3.4	Deliberate orientation of dipole modes using asymmetric slots	119
5.3.5	Simulation of complete cavity BPM geometry	122
5.4	Fabrication	130
5.5	Benchtop RF measurements	131
5.5.1	Test instruments	131
5.5.2	S-parameter measurements	132
5.5.3	Calculation of Q-values using impedance method	135
5.5.4	Field orientation measurements.	139
5.6	Study of fabrication errors by simulation reconstruction	145
5.6.1	Coupling slots shifted from its axis	145
5.6.2	Performance degradation due to rotated slots	147
5.6.3	performance degradation due to misalignment of the enclosing cap	149
5.7	Beam testing at ATF2 beam line	152
5.7.1	Cavity response measurements using diode	153
5.8	Summary	157

6	Conclusions and discussion	159
6.1	Summary of multi-bunch signal processing study	159
6.2	Summary of CBPM design study	160
6.3	Discussion of open research questions	163
A	Multibunch Signal calculation	164

List of Figures

1.1	Layout of ILC facility for 500 GeV CME design [8].	22
1.2	Proposed layout of CLIC for a design with 3 TeV CM energy [12].	25
2.1	Simplified drawing of a shoe-box BPM, showing two plate electrodes and corresponding segments of a beam trajectory (in red) superimposed.	30
2.2	Simplified vertical cross-section drawing of a button BPM, showing the two electrodes at radius a inside a beam pipe.	31
2.3	A simplified section through a stripline BPM in the beam direction.	32
2.4	Three dimensional and plan diagrams to explain the working principle of a cylindrical cavity BPM.	33
2.5	Simulated typical CBPM signal, induced by a bunch in a cavity with dipole mode frequency of 6 GHz and Q_L of 250.	40
3.1	Resonance frequencies of major TM modes and signal processing scheme of a CBPM with dipole mode frequency f_{110} near 6 GHz.	48
3.2	Resonance frequencies of major TM modes and signal processing scheme of a CBPM with dipole mode frequency f_{110} near 18 GHz	49
3.3	Simulated CBPM signal induced by a bunch train in a cavity with dipole mode at 6 GHz and Q_L of 250, showing the change in signal amplitude as a function of time.	50
3.4	Simulated CBPM signal induced by a bunch train in a cavity with dipole mode at 6.1 GHz and Q_L of 250, showing the change in signal amplitude as a function of time.	51

3.5	Simulated CBPM signal induced by a bunch train in a cavity with dipole mode at 7 GHz and Q_L of 250, showing the change in signal amplitude as a function of time.	52
3.6	Change in signal pollution with change in Q_L values of a cavity with dipole mode at 6 GHz	53
4.1	Layout of the ATF and ATF2 extraction line [37].	57
4.2	Enlarged layout of ATF2 extraction line showing accelerator beam optics components and cavity BPMs [37].	59
4.3	Block diagram of typical a typical single channel analog and digital processors.	62
4.4	Block diagram of the test setup to measure the gain and bandwidth of a CBPM electronics card.	63
4.5	Linearity and bandwidth measurements of an electronic card to process CBPM signals	64
4.6	Digitised raw IF signal in time and frequency domains.	64
4.7	Mixed signal in the time and frequency domains	66
4.8	Convolution weights for a Gaussian filter with $f_c/f_s = 0.08$	67
4.9	Filter characteristics comparison	68
4.10	Processed signal after application of the Gaussian digital LPF, showing a sample t_s where the I and Q phasors are calculated	69
4.11	Phase of the down-converted IF signal as a function of sample number, for two different digital LO frequencies.	70
4.12	Calibration plots showing IQ diagram, phase rotation, position scale determination and residual histogram.	72
4.13	Change in the resonance frequency of a CBPM as a function of temperature.	74
4.14	Layout of the simulation and analysis code.	75
4.15	Simulated digitised IF signals from two bunches separated by 187.6 ns	77
4.16	Processed amplitude and phase, with sample location for position determination for each bunch.	81
4.17	Calibration of MQM13FF in a multi-train mode without signal subtraction.	82
4.18	CBPM system calibration in a multi-train mode with signal subtraction.	83

4.19	Processed phases of the IF signals from cavities MQM13FF and REFC1, induced by two bunches.	85
4.20	IQ plots of subtracted phasors from calibrations of MQM13FF along the y -axis, for two different bunch separations Δt_b	86
4.21	IQ diagram from a calibration run of MQM11FF, without signal subtraction.	87
4.22	IQ diagrams from a calibration run of CBPM MQM11FF, with signal subtraction, showing second bunches arriving at different position to the first bunch	88
4.23	Plots showing correlation with SVD based prediction, and reduction in position residual after SVD based jitter subtraction.	90
4.24	Determination of the bunch arrival time t_b and its variation.	92
4.25	Variation in DDC phase.	93
4.26	Effects of the digital LPF of different cutoff frequencies on the convolution window and signal amplitude.	94
4.27	Effects of digital LPF with different cutoff frequencies on signal processing and resolution.	95
4.28	Digitised raw signal and processed amplitude induced by three bunches.	96
4.29	IQ plots from experimental and simulated signals induced by three bunches.	97
4.30	Histogram of jitter from experimental and simulated signals induced by three bunches.	98
4.31	Plot of signal amplitude ratio, separated by 16 samples, as function of amplitude at the first point.	99
4.32	Gain at different digitised output signal amplitudes	99
5.1	Model schematic layout of the Diamond Light Source.	104
5.2	Simulation workflow and distribution of software on various computer systems.	107
5.3	Transit time factor α_{TT} for the monopole and dipole modes of a pillbox cavity with different lengths.	111
5.4	Simulation model of pillbox cavity.	111
5.5	Geometry model of a pillbox cavity with beam pipes, solved using Omega3P.	113

5.6	Simulation model of a waveguide adapter with coaxial coupler, showing dimensions and ports.	115
5.7	Simulated S-parameter responses of the waveguide adapters with coaxial beads of different radius r_c , at constant gap g_c	118
5.8	Simulated S-parameter responses of the waveguide adapters with different gap (g_c), for constant bead radius (r_c)	118
5.9	Simulation model to study effects of asymmetric coupling slots along x and y axes.	119
5.10	Simulation results from the study of the separation of the dipole modes using asymmetric coupling slots along the x and y axes	121
5.11	Simulation model of complete CBPM geometry.	123
5.12	Cavity dipole frequency and Q_0 as function of number of mesh elements.	123
5.13	Field orientation of the lowest four frequency resonant modes derived from the Eigenmode simulations of complete CBPM model.	124
5.14	Results of S-parameter simulations of a complete CBPM geometry using S3P.	126
5.15	Results from time domain simulation of a complete CBPM geometry using T3P.	129
5.16	One of the four fabricated cavity BPMs for the Diamond Light Source.	130
5.17	Block diagram of remote hardware control scheme for RF measurements.	132
5.18	Experimental setup to measure the S-parameters of a CBPM, and measurement results.	133
5.19	Cavity equivalent circuit reduced to a single port connection.	135
5.20	Rotation of the S-parameter traces during calculation of Q values using impedance method. Red circles represent the peak (resonant frequency) points on the S-parameter traces. The black circle represents $R=0$ circle.	136
5.21	Traces shifted to match calculated Q_L values to those from the transmission curves	137
5.22	Experimental setup for field orientation measurements.	140
5.23	GUI interface screen of the LabVIEW program for field orientation measurement scan.	141

5.24	Program flow of the LabVEIW sequence for field orientation measurement scan.	142
5.25	Measurement of dipole field orientation using phase of the reflected signal.	143
5.26	Measurement of quadrupole field orientation using phase of the reflected signal.	144
5.27	Simulation of S-parameter response of CBPM models with two slots shifted from their ideal positions.	146
5.28	Effect slots rotated around cavity axis.	148
5.29	Simplified drawings of a CBPM showing an uneven gap between cavity and enclosing cap in a simulation model to reconstruct the fabrication errors.	149
5.30	Rotation of the dipole fields due to the enclosing cap rotated by angle $\Delta\phi = 45^\circ$	150
5.31	Results from Eigenmode simulations to study the effects of a misaligned cavity cap on the field orientation and resonance frequencies of the dipole modes	151
5.32	NLS cavity installation at ATF2.	153
5.33	Block diagram of a connection setup for beam measurement of the CBPM with diode, and diode sensitivity at different load impedances.	154
5.34	Typical cavity output signal detected using diode and reverse calibration curve for diode.	155
5.35	Calibration of CBPM along x and y axes, the cavity outputs were detected using Schottky barrier diodes.	156

List of Tables

1.1	Set of major machine parameters of ILC for a proposed design with 500 GeV CME [8].	21
1.2	Major parameters of the main linacs and beams for the 3 TeV design of CLIC. [12, 14]	27
3.1	BPM requirements for CLIC main linac.	47
4.1	Typical operation values of the major parameters of the ATF.	56
4.2	Parameters and functions of BPM cavities on ATF2.	60
4.3	Definitions of mathematical variables used for multi-bunch signals.	77
4.4	Frequency and decay time of the cavity triplet used for the studies of the CBPM signals from multiple bunches.	80
4.5	Systematic error in bunch position measurement due to signal pollution, and removal of signal pollution using signal subtraction algorithm	84
4.6	IQ rotation angle difference $\Delta\Theta_{IQ}$ between the first and second bunch phasors, for different bunch separations Δt_b	85
4.7	Comparison of the change in the amplitude of position signal for second bunch, with and without signal subtraction	87
4.8	Error in position measurement after SVD based beam position jitter subtraction.	91
4.9	RMS position jitter measured for three bunches	100
5.1	Major parameters of the Diamond Light Source storage ring.	105

5.2	Resonant frequency of a pillbox cavity calculated using different Eigenmode solver packages.	112
5.3	Internal quality factor Q_0 of a pillbox cavity derived using different Eigenmode solver packages.	112
5.4	Eigenmode simulation results of a model with cavity and beam pipes. .	114
5.5	Simulation parameters used for study of waveguide adapter	117
5.6	Parameters of the simulation model to study mode separation	120
5.7	Results of the Eigenmode simulations of the complete CBPM model, using Omega3P.	125
5.8	Results of S-parameter simulations of the complete CBPM model. . . .	127
5.9	Parameters used for the time domain simulation of the complete CBPM geometry.	128
5.10	Results of S-parameter measurements.	134
5.11	Q values calculated using impedance method.	138
5.12	Variation in frequency and isolation of the CBPMs with slots shifted by different position offsets.	147
5.13	Change in frequency and $x - y$ isolation for slots rotated by different angles.	148
5.14	Results of beam measurements with signal detection using diodes. . . .	156
6.1	Error in position measurement after SVD based beam position jitter subtraction.	160

Chapter 1

Introduction

Particle accelerators, from the simple cathode ray tube (CRT) in televisions to the Large Hadron Collider (LHC) with a 27 km circumference, have played a very important role in scientific, technological and social development. With the demonstration of the nitrogen nucleus disintegration by natural alpha particles in 1917, Rutherford fueled enthusiasm in the new field of particle physics [1]. The need for a source of artificially accelerated particles was soon expressed and realised by Rutherford in front of the Royal Society in 1927.

High energy particle accelerators have been designed to accelerate various particles for versatile applications. From the development of CRT in 1870, it took six decades to develop the first 80 keV cyclotron in 1931 [2]. The development of accelerators happened in many stages. The requirement for even higher energy particles has never stopped and so the development in accelerator concepts [1]. The first accelerators using direct voltage reached their practical limits by using big spherical electrodes and better insulation, while avoiding voltage breakdown by dividing voltage in multiple stages.

In the next stage of accelerators, such as the cyclotrons and early linear accelerators, the problem of voltage break down was resolved by passing the particles multiple times through a smaller potential drop in resonance with an oscillating electric field. The third stage of accelerators were developed by applying the concept of phase stable accelera-

tion, which started the area of synchro-accelerators [1]. The particles were accelerated by an oscillating electromagnetic (EM) field in resonant structures, synchronised at a specific phase. In this way the limitation of direct current (DC) breakdown could be overcome by using the localized energy stored in a resonant cavity. In this way radio frequency (RF) resonant cavities have played a very important role in development of the accelerators.

Particle accelerators are developed for different purposes ranging from pure fundamental research in particle physics, to user facilities for high-intensity high-energy light. As discussed in the following sections, the accelerators can be classified based on their applications and layout.

1.1 Particle colliders

The field of particle and atomic physics has evolved with the contributions of many people. With the discovery of the electron by J. J. Thomson in 1897, the prevailing belief that a Hydrogen atom is the basic element of matter was broken. The experiments to break an atom by bombarding it with accelerated particles required an artificial source, other than radioactive nuclei. The accelerators, such as Bevatron [3] at Lawrence Berkeley National Laboratory (LBNL) in the USA, were built to artificially generate particles, such as antiprotons, in 1955. The Bevatron was a weak-focusing proton synchrotron accelerating the beam to energies more than 6.2 GeV. The energy and intensity of accelerated beams continued to rise throughout the 20th century, with the synchrotron as the work horse of high energy physics.

At the Fermi National Accelerator Laboratory (FNAL), the quest for elementary particles proceeded with the Tevatron high energy particle collider. The Tevatron was a proton-antiproton collider with a 6.2 km circumference, and it accelerated the beams up to 1 TeV. Two detectors, CDF and DØ, recorded the particles generated from the collisions of the beams. The Tevatron announced the discovery of top quark in 1995. Within 2006 to 2008, the experiments detected two types of baryon. The last collisions from the Tevatron were recorded in September 2011. On July 2, 2012, the Tevatron an-

nounced sets of analysis results for its collision data, showing no statistically significant evidence for the Higgs boson.

The Large Hadron Collider (LHC) built by European Organization for Nuclear Research (CERN) is situated near Geneva, on the border of Switzerland and France. It is designed to accelerate proton beams up to 7 TeV. To bend such a high energy beam of protons, the LHC uses 1600 superconducting magnets generating magnetic field up to 8.3 T. The particles generated from the collisions of the beams are detected by two general purpose detectors, ATLAS and CMS. The other two detectors, ALICE and LHCb, are designed to investigate quark-gluon plasma and missing antimatter respectively. The LHC reported to produce quark-gluon plasmas during 2010 operation. In 2011, the LHC experiments started search for the Higgs boson, the primary physics research goal of the machine. LHC experiments could not find any sign of the Higgs boson in the higher mass range. Finally on July 4, 2012, the ATLAS and CMS teams at CERN announced the discovery of a boson with mass of $125.3 \text{ GeV}/c^2$, with a significance of 4.9 sigma, which is consistent with the Higgs boson [4, 5].

1.1.1 Synchrotron radiation and limitation on circular collider

In classical electrodynamics, when a charged particle is accelerated in a uniform vertical magnetic field, it emits energy in terms of electromagnetic radiation, which is called synchrotron radiation. The total radiated power P_{syn} by an accelerated electron is calculated as [6],

$$P_{\text{syn}} = \frac{e^4 \gamma^4}{6\pi \epsilon_0 m_e^4 c^5} B^2, \quad (1.1)$$

where e is the charge of the electron, γ is the relativistic Lorentz factor, ϵ_0 is the permittivity of free space, m_e is the rest mass of the electron, c is the speed of light and B is the magnetic field strength.

The radiated power is proportional to γ^4 . It also means that a lighter particle will emit more radiation compared to a heavier particle with the same energy. An electron will emit 6.19×10^9 times more energy than a proton with the same total energy. This limits the energy up to which the electrons and positrons can be accelerated

efficiently in a circular machine. To reduce the radiation loss, the magnetic field should be weaker, which decreases the bending angle and increases the overall size of the machine. To overcome this limitation, linear accelerators can be used to accelerate and collide electrons and positrons at high energies.

1.1.2 Linear colliders

The SLAC Linear Collider (SLC), situated at the SLAC National Accelerator Laboratory, California, was a 3.2 km long electron-positron collider, designed for 91 GeV center of mass (CM) energy [7]. It was the first linear collider; designed solely to collide electrons and positrons to study the Z^0 particle. Based on the experiences acquired during the design and operation of this machine, future linear colliders such as the International Linear Collider (ILC) and Compact Linear Collider (CLIC), were proposed.

a) International Linear Collider

International Linear Collider (ILC) is a proposed electron-positron collider with 200-500 GeV center of mass energy (CME), with a provision to upgrade it to 1 TeV [8]. ILC is proposed to provide a peak luminosity of $2 \times 10^{34} \text{ cm}^{-2}\text{s}^{-1}$. A set of parameters for the ILC design with 500 GeV CME is listed in Table 1.1. The energy range of ILC should provide an opportunity to study the physics of top-quarks and Higgs boson with better precision. The physics and engineering concepts and techniques required for ILC are being developed by different collaborators, and it will also benefit from the experience gained from other accelerators developed in past and present.

A layout of ILC facility for the design with 500 GeV CME is shown in Fig. 1.1. A polarised electron source will use a laser illuminating photo-cathode gun to produce electron beams [8]. The beam will be bunched and accelerated up to 76 MeV using normal conducting acceleration structures. The bunched beam will be further accelerated to 5 GeV in a superconducting linac. Before injecting into a damping ring (DR), the spin vectors of the electrons will be rotated in the vertical direction using a superconducting solenoid, and the corresponding energy will be compensated using additional accel-

Table 1.1: Set of major machine parameters of ILC for a proposed design with 500 GeV CME [8].

Parameters	Value	Unit
Center of mass energy	200-500	GeV
Peak luminosity	2×10^{34}	$\text{cm}^{-2}\text{s}^{-1}$
Charge per bunch	1.6 - 3.2	nC
Bunch length σ_z	0.3	mm
Number of bunches per train	2625	
Bunch spacing	369	ns
Pulse repetition rate	5	Hz

ation structures. The positrons will be generated using photo-production techniques, by directing the photons emitted by the accelerated electrons on to a rotating target of Titanium. The positrons generated from the target will be captured and accelerated up to 5 GeV, while the electrons and photons will be dumped. The spin vectors of the positrons will also be rotated in the similar way as of the electrons and the energy will be compensated. The beams will then be injected into the corresponding damping rings.

ILC will have separate damping rings for electron and positron beams, each with a circumference of 6.7 km, divided into six arcs and straight sections [8]. The straight sections will have focusing defocusing (FODO) cells, and the arc sections will contain theoretical minimum emittance (TME) cells. The damping ring should be able to reduce the horizontal and vertical emittances to the desired lower values, of $8.0 \mu\text{m}$ and 20 nm respectively, within a short duration of 200 ms. The damping rings are proposed to use superferric wigglers with a peak field of 1.67 T. The superconducting RF acceleration system will provide an acceleration voltage of 24 MV at 650 MHz for energy compensation [8]. The DR should be able to suppress the larger jitters in the injected beam, and facilitate a fast feedback system to control the bunch instabilities. Because the bunch separation in the main linac section is larger than in the damping rings, it should be possible to extract a bunch individually without affecting the emittance of the other bunches. The bunches will be extracted using the short RF pulse field in a stripline kicker.

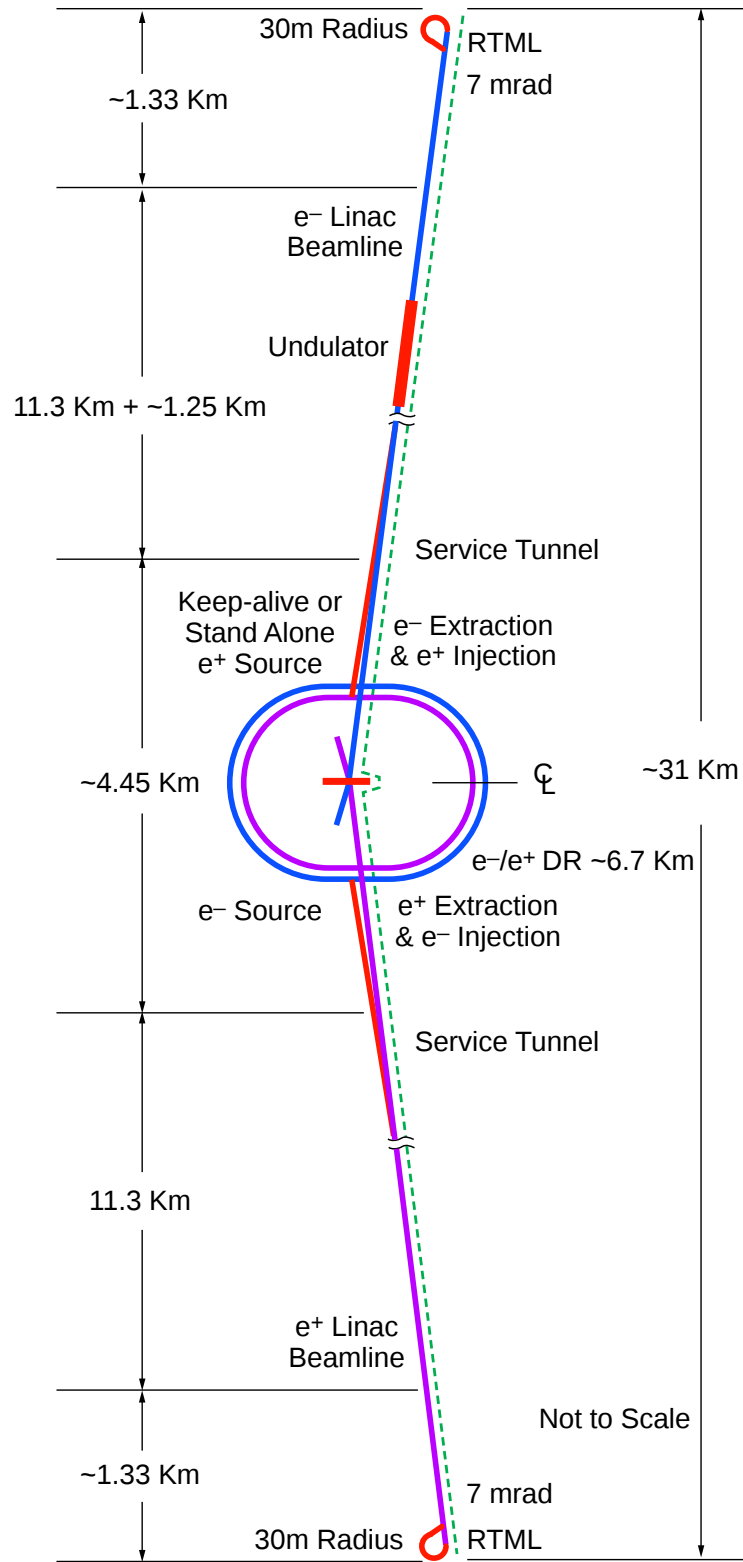


Figure 1.1: Layout of ILC facility for 500 GeV CME design [8].

The bunches extracted from the DRs will be transported to the main linacs through ring to main linac (RTML) sections. In RTML, the longer bunches from the damping rings will be compressed in two stages, by a factor of 30 to 45, to $300\ \mu\text{m}$ [8]. In RTMLs, the beams will also be accelerated up to 15 GeV from the 5 GeV energy at DR extraction. In addition to bunch compression and acceleration, the beam will also be collimated and the spin rotation angles of the electrons and positrons will be rotated as per requirements at the interaction point (IP).

The 15 GeV beams of electrons and positrons from the RTMLs will be further accelerated to their final target energy of 250 GeV in two separate main linacs [8]. The combined length of both main linacs will be 23 km. Both linacs will use nine cell superconducting standing wave cavities, which will provide an average acceleration gradient of 31.5 MV/m at 1.3 GHz. Each of the 14560 superconducting radio frequency (SRF) cavities is proposed to have fill time of 596 μs and internal Q values higher than 0.8×10^{10} . The main linac will use weak focusing FODO optics with one quad per RF unit. The lattice and accelerator components are designed to restrict the emittance growth to less than 10 nm in the vertical direction.

The parameters of the beams accelerated in the main linacs will be verified in the beam delivery system (BDS) [8]. The parameters will be matched to the requirements at the IP. It will also remove any beam-halo and mis-steered beams, to prevent damage to the detectors and to minimise the background in the detectors. The final focus (FF) optics blows the beam size and make it almost parallel at the entrance of the final doublet (FD) of strong quadrupoles. The FD will demagnify the beam, and the required chromatic corrections will be applied using additional sextupoles. Two beams will then collide at the interaction point at a nominal angle.

The ILC BDS will be equipped with different beam diagnostics systems such as beam current monitors, beam loss monitors, laser wires, optical transition radiation (OTR) screens and beam position monitor (BPM) systems. The beam position will be measured along the beam line using three different types of BPMs, based on the principles of striplines, buttons and resonant cavities. Their working principles are explained in Chapter 2. The ILC BDS will use 312 cavity BPMs, working in the L, S and C fre-

quency bands, depending on the beam size in different sections of the beam line. Other than BDS, cavity BPMs will also be used in the RTML and main linac sections of the ILC.

***b)* Compact Linear Collider**

The Large Hadron Collider (LHC), at CERN in Geneva, will explore the TeV energy range by colliding beams of hadrons. One should not expect from the LHC experiments answers to all questions concerning new physics. For example, any Higgs boson other than those detected by the LHC experiments can be interesting. If super-symmetry is the working principle, then the LHC may not be able to measure all super partners. A lepton-antilepton collider can answer many of the residual questions. In lepton-antilepton collisions, all of the center of mass energy is available for the production of elementary particles [9].

To address some of the open questions, a multi-TeV lepton collider, called the Compact Linear Collider (CLIC), has been proposed. It will collide bunches of electrons and positrons with a 3 TeV center of mass (CM) energy [10], with a provision to increase it up to 5 TeV. The machine will be upgraded in steps to the final energy.

Some of the major physics topics for research at CLIC will be to investigate the contribution of a lighter Higgs boson to the muon mass, and to study the heavy Standard Model (SM) Higgs boson, super-symmetric Higgs boson and Charge Parity (CP) violation [10, 11]. In addition CLIC should also provide precise measurements of gluinos and strongly interacting quarks. At CLIC it should be possible to fully utilize its high center of mass energy to test the Standard Model and some new physics beyond the Standard Model.

The proposed design of CLIC can be divided into different subsystems. A block diagram of a proposed machine layout for the design with 3 TeV CM energy is shown in Fig. 1.2. The electrons and positrons will be accelerated up to 200 MeV in different pre-injector linacs before injecting into a common injector linac, which will further accelerate them up to 2.86 GeV [12]. In the common injector linac, the bunch repetition frequency

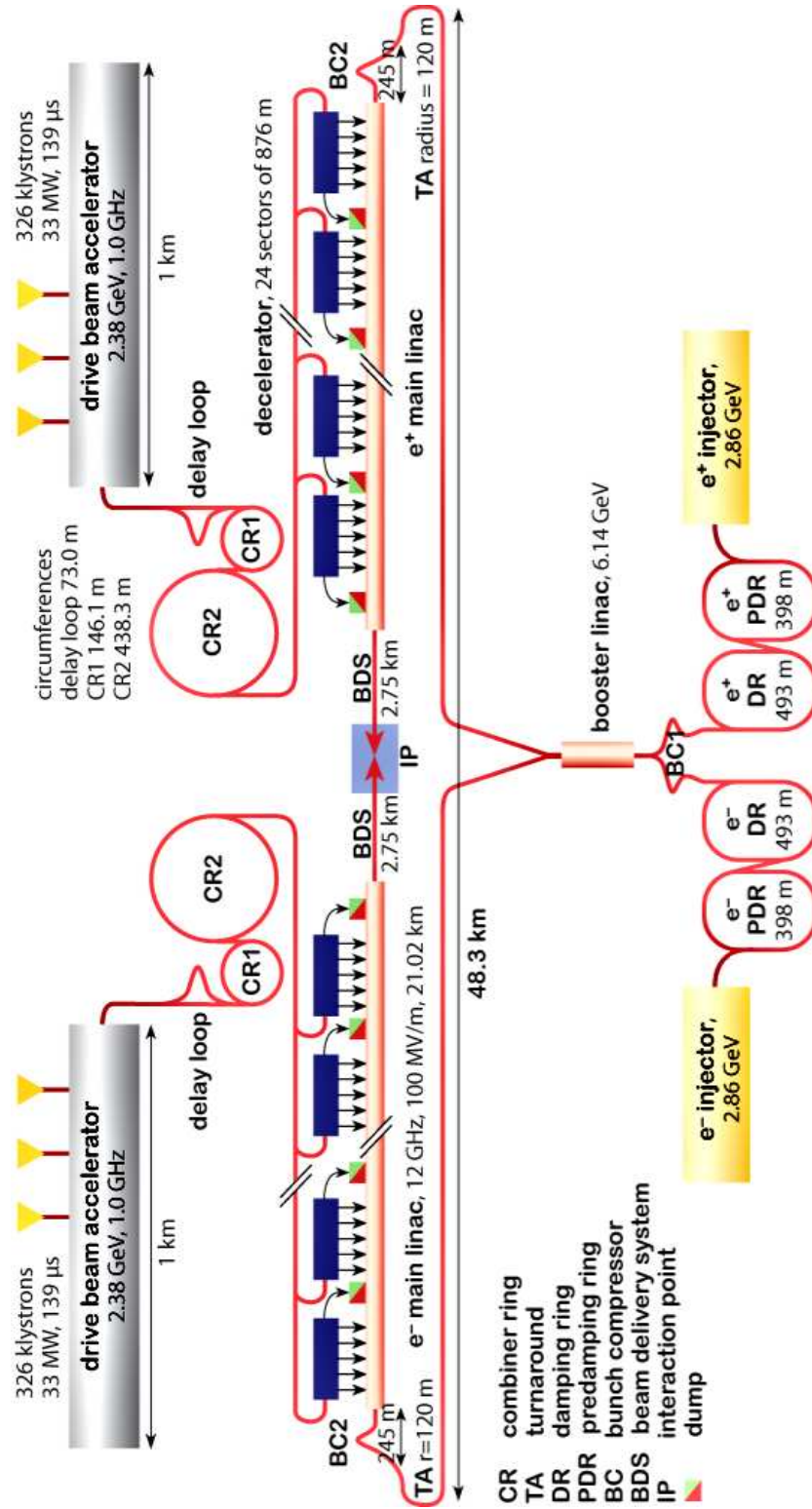


Figure 1.2: Proposed layout of CLIC for a design with 3 TeV CM energy [12].

will be 1 GHz, while the accelerating structures will use an RF voltage at 2 GHz. The accelerated e^- and e^+ bunches will be separated and injected into the separate pre-damping rings.

The damping rings will cool the injected e^- and e^+ beams, by radiation damping, to reduce their emittances to the smaller values required for collisions [12]. The beams will be cooled in two stages. Two damping rings are required because of the large emittance of the beams coming from injector and the high bunch repetition rate. The normalised beam emittances at the output of the injector, of 100 and 7000×10^3 nm.rad for the e^- and e^+ beams respectively, will be reduced to 500 nm.rad by the process of radiation damping. To cool the beams, pre-damping and damping rings will use the wigglers with peak magnetic fields of 1.9 and 2.5 T respectively. The delay loops are used to create the required 2 GHz bunch train structure.

The beams extracted out of the damping rings will be transferred to the main linacs, through Ring To Main Linac (RTML) sections [12]. In RTML the beams will be accelerated to 9 GeV, which is the proposed particle energy at the injection to the main linacs.

The major proposed parameters of the main linacs are listed in Table 1.2. A CLIC main linac will be based on the Two Beam Acceleration (TBA) scheme, in which the RF power extracted from a high current low energy drive beam will be used to accelerate a low current main beam [12, 13].

The drive beam will be formed of 24 bunch trains which are separated by $5.85 \mu\text{s}$. The bunch trains with a bunch repetition frequency of 0.5 GHz, accelerated up to 2.37 GeV by the drive beam linac, will then enter the Drive Beam Recombination Complex (DBRC). Using a delay line and two combiner rings, the bunch trains will be compressed to increase the bunch repetition frequency to 12 GHz, which will increase its average current to 100 A. Each of the 244 ns long bunch trains will be made of 2928 bunches of 8.4 nC charge each.

The power stored in the drive beam will be extracted using Power Extraction and Transfer Structures (PETS), which will be transferred to the main beam running alongside

it. A single tunnel will house the beam lines for both of the main beam and drive beam.

Table 1.2: Major parameters of the main linacs and beams for the 3 TeV design of CLIC. [12, 14]

Parameter	Symbol	Value	Unit
Center of mass energy	E_{cm}	3	GeV
Overall linac length	l_{linac}	42.16	km
Number of drive beam sectors	N_{unit}	24	
Main linac RF frequency	f_{RF}	11.994	GHz
Gradient (loaded)	G	100	MV/m
Luminosity	L	5.9	$\times 10^{34} \text{ cm}^{-2}\text{s}^{-1}$
Drive beam			
Beam energy	$E_{\text{in,dec}}$	2.4	GeV
Beam pulse current	I_{dec}	100	A
Number of bunch train in a beam	$N_{\text{train,dec}}$	24	
Train separation	$\Delta t_{\text{train,dec}}$	5.8	μs
Bunch repetition frequency	$f_{\text{b,dec}}$	11.994	GHz
Bunch charge	$q_{\text{b,dec}}$	8.4	nC
Main beam			
Number of bunches per train	N_b	312	
Beam pulse current	I	1.5	A
Bunch repetition frequency	f_b	2	GHz
Bunch charge	q	> 0.6	nC
Bunch length	σ_s	44	μm

The main beams will be accelerated from 9 GeV to 1.5 TeV, using an RF acceleration voltage of 100 MV/m at 11.994 GHz [12, 13]. A total peak RF power of 9.2 TW will be required for both linacs. The main beams will be formed of the bunch trains with a train repetition frequency of 50 Hz. Each bunch train will be 156 ns long, producing a pulse current of 1.5 A. Each train will have 312 bunches of 0.6 nC, separated by 0.5 ns.

1.2 Storage rings and free electron lasers as a light source

A storage ring is a circular accelerator used to store an accelerated beam, for longer duration while extracting its energy in the form of electromagnetic radiation. Because the electrons are easy to produce and lighter than other charged particles, synchrotron light sources typically use electron beams. The potential of synchrotron radiation

for research and measurement was realized in the 1950's and light sources, such as the Cosmotron at Brookhaven National Laboratory (BNL) in the USA, were commissioned. The technology and design of magnets have since then developed and third generation synchrotron light sources at present use special magnets known as undulators and wigglers (insertion devices) to produce the synchrotron radiation. Unlike simple dipole magnets, the insertion devices are made from pairs of north and south poles arranged alternatively [15, 6]. The radiation extracted is collimated and transported through beam lines to user areas, where it is used for different research techniques. The extracted radiation is typically in the wavelength range from visible to X-rays, and can be stacked as short pulses of high intensity. The fourth generation of light sources are linear accelerator facilities known as free electron lasers (FEL).

Synchrotron radiation from light sources is used over a broad range of research areas ranging from condensed matter, archaeology, crystallography, electronics and material science to biology and medical applications. The radiation is used for optical analysis techniques, such as electromagnetic (EM) spectroscopy and imaging techniques based on absorption, emission, diffraction and scattering mechanisms. The short and high intensity pulses from a light source make it possible to take high speed images with higher resolution.

Introduction to beam position monitor systems

With the development of acceleration techniques, beam diagnostics have also evolved to provide more precise and faster measurements. The accurate measurements of beam positions make it possible to study the beam trajectory, dynamics and verify machine optics. In this chapter, various techniques to determine the beam position of different particle beams with different parameters are discussed. After brief introduction to the working and applications of different beam position monitor (BPM) systems, the working principle of a cavity beam position monitor (CBPM) is explained in detail. The advantages and drawbacks of a CBPM system are discussed briefly.

2.1 Diagnostics for beam position measurement

BPM diagnostics are normally non-destructive. They can be based on different principles, such as capacitive, inductive, traveling wave and resonant structure techniques. Short introductions to the working principles of these techniques are given in the following sections.

2.1.1 Shoe-box BPM

A shoe-box BPM uses capacitive pickup from the beam. As shown in Fig. 2.1, a typical shoe-box BPM contains a rectangular conductor plate, of width $2a$ and length l , with a diagonal cut in it.

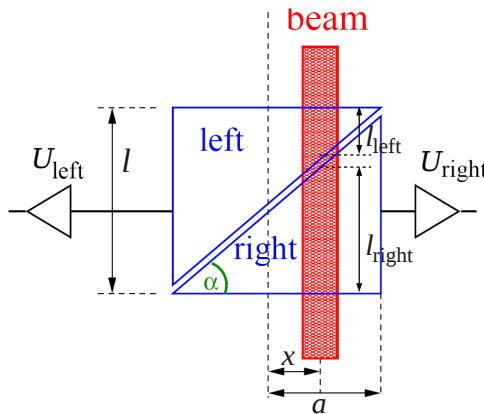


Figure 2.1: Simplified drawing of a shoe-box BPM, showing two plate electrodes and corresponding segments of a beam trajectory (in red) superimposed.

For any beam trajectory at a specific position x , the beam trajectory segments within each of the plates are of different lengths. The capacitively induced voltage on each of the plates is proportional to the lengths of the segments. The beam position is proportional to the difference between the voltages induced on the two plates, calculated as [16, 17],

$$x = a \frac{l_{right} - l_{left}}{l_{right} + l_{left}} = a \frac{U_{right} - U_{left}}{U_{right} + U_{left}} = a \frac{\Delta U}{\sum U}, \quad (2.1)$$

where l_{left} and l_{right} are the lengths of segments and U_{left} and U_{right} are the induced voltages on the left and right plates respectively.

The major advantage of the shoe-box technique is the linear dependence of the output signal on the position offset. It is generally used for ion beams with bunches longer than the plates. The output signal has a very small dependence on the frequency. The system can operate at a bandwidth between direct current (DC) and 100 MHz, and

has a typical position resolution of the order of a few μms .

2.1.2 Button BPM

A button BPM is another example of a capacitive BPM. As shown in Fig. 2.2, the two button electrodes are kept at a same distance a from the centre of the beam pipe. They are kept electrically isolated from the beam pipe.

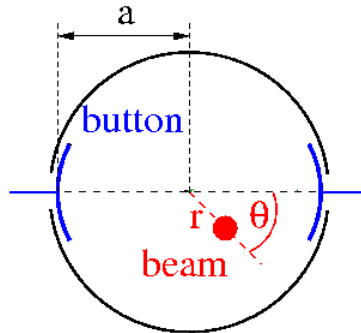


Figure 2.2: Simplified vertical cross-section drawing of a button BPM, showing the two electrodes at radius a inside a beam pipe.

The image current induced on a button electrode, by a bunch passing at a radial distance r and angle θ , will induce a voltage across the impedance between the electrode and beam pipe. From the induced voltages on both electrodes, the beam position x can be derived as [18, 17],

$$x = r \cos(\theta) = \frac{1}{S} \frac{\Delta U}{\sum U}, \quad (2.2)$$

where ΔU and $\sum U$ are respectively the difference and sum of the induced voltages on the electrodes. S is the sensitivity constant derived from system calibration.

The amplitudes of the voltages induced on the buttons have a non-linear dependence on the position of the beam. In comparison to the shoe-box type BPMs, the button BPMs have smaller capacitance and can operate at 50Ω . Button BPMs are generally used for high energy electron accelerators and light sources where the bunches are shorter or of the same length of the button electrodes. The button BPMs can measure the beam

position with a resolution of 10 to 100 μm , at a bandwidth up to 1 GHz.

2.1.3 Stripline BPM

A stripline BPM works on the principle of a traveling wave. Fig. 2.3 shows a simplified drawing of a stripline BPM made of two striplines of length l and characteristic impedance Z_{strip} . A bunch of relativistic charged particles passing by the striplines induces an electromagnetic (EM) pulse on the striplines [17]. Half of the induced pulse generates voltage across a resistance R_1 at port 1 of the stripline, while other half of the induced pulse travels along the stripline. On arrival at port 2, the half of the traveling pulse gets reflected and returns to port 1, while the other half generates a voltage across a resistance R_2 .

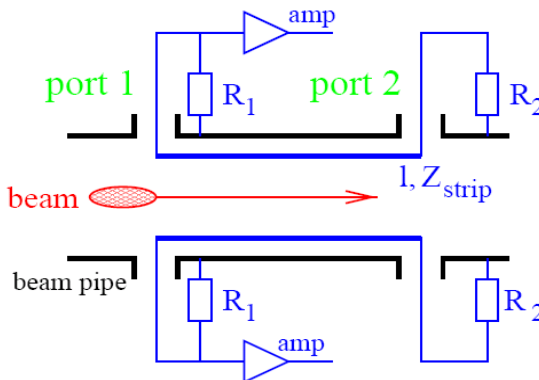


Figure 2.3: A simplified section through a stripline BPM in the beam direction.

The impedance Z_{strip} of the stripline must be matched carefully to the load. Machining and installation of the stripline is relatively complex. The length of the stripline should be chosen such that the reflected pulse from port 2 should not cancel the signal induced by the next bunch at port 1. At any instance of time t , the induced voltage U_1 at the port 1 can be calculated as,

$$U_1(t) = \frac{1}{2} \frac{\alpha}{2\pi} R_1 [I_b(t) - I_b(t - 2l/c)], \quad (2.3)$$

where I_b is the beam image current, α is the angular width of the stripline, l is the length of the stripline and c is the speed of light. In the case of relativistic short

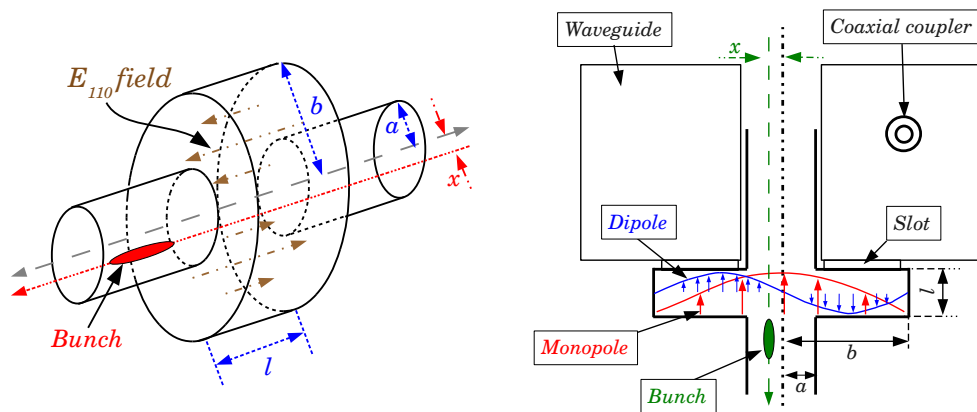
pulses, the signal will appear as two pulses out of phase and separated in time by $2l/c$. Stripline BPMs are generally used on electron machines to measure the position of short relativistic bunches. They typically have a position resolution of $10 \mu\text{m}$. As the measurements with striplines are sensitive to the direction of beam propagation, they are very useful to distinguish between the signals induced by two beams rotating in opposite directions.

2.2 Cavity beam position monitor

A cylindrical cavity is a cylindrical metallic pipe of radius b and length l , enclosed at both ends by conducting plates. As shown in Fig. 2.4(a), the beam is allowed to pass by the beam pipe of radius a connected via holes in the end plates.

2.2.1 Theory and working principle

Because a cavity is a single conductor structure, the electric and magnetic fields at all locations inside a cavity are always orthogonal to each other. The values of the EM



(a) Three dimensional view of a simple cylindrical cavity geometry showing a bunch and direction of the induced dipole electric field E_{110} with respect to the bunch.

(b) A simplified cross section in the beam direction of a CBPM showing cavity, coupling slots, waveguides and coaxial coupler, along with the induced electric fields in the monopole and dipole modes.

Figure 2.4: Three dimensional and plan diagrams to explain the working principle of a cylindrical cavity BPM.

field components inside the cavity can be calculated by solving Maxwell's equations and applying appropriate boundary conditions at the cavity walls [19, 20]. These conditions limit the EM field to oscillate with specific field distribution patterns, known as the resonant modes of the cavity. Based on the direction of the EM field components, the resonant modes can be classified in either a transverse electric (TE) type mode, with its electric field perpendicular to the cylindrical axis of the cavity, or a transverse magnetic (TM) type mode, with its electric field aligned parallel to the cavity axis. The electric field distribution of the two primary TM modes of interest, first monopole (TM₀₁₀) and dipole (TM₁₁₀), are shown in Fig. 2.4(b). In the notation TM_{mnp}, the m , n and p are the mode numbers along ϕ , r and z axes of the cavity respectively. The m , n and p can be seen as a number of electric field poles (peaks) within the half range along the respective coordinate axis, e.g. m shows the number of peaks within 0 to π angle along the ϕ -axis.

When a bunch of high energy charged particles passes through a resonant cavity, some of its energy gets coupled in the cavity and induces oscillating electromagnetic (EM) fields over the different resonant modes. Among all TM modes, the amplitude of the induced dipole mode (TM₁₁₀) is proportional to the charge and position offset of the bunch from the centre of the cavity, hence it can be used to measure the beam position. On the other hand for a small position offset, the amplitude of the induced monopole mode (TM₀₁₀) does not depend on the bunch position, but it is sensitive to the bunch charge. It can be used to provide reference measurements for the bunch charge and bunch arrival time. The induced EM fields in the modes oscillate with time at the resonant frequencies of the modes. The resonant frequency f_{mnp} of a transverse magnetic mode TM_{mnp} of an empty cavity is given by [19],

$$f_{mnp} = \frac{\omega_{mnp}}{2\pi} = \frac{1}{2\pi \sqrt{\mu_0 \epsilon_0}} \sqrt{\left(\frac{j_{mn}}{b}\right)^2 + \left(\frac{p\pi}{l}\right)^2}, \quad (2.4)$$

where μ_0 and ϵ_0 are the permeability and permittivity of the free space respectively, m , n and p are the mode numbers in the cylindrical coordinates ϕ , r and Z respectively. The ω_{mnp} is the angular resonant frequency, j_{mn} is the n^{th} zero of the Bessel function of order m . The resonant frequency of a mode is inversely proportional to the radius

of the cavity.

The minimum radius of the cavity is limited by the radius of the beam pipe. The cavity radius should be large enough to allow resonances, and to support the power extraction mechanism. As the beam pipe acts as a circular waveguide and high pass filter, the resonant frequencies of the strongly coupled modes of the cavity should be less than the cut-off frequency of the beam pipe to restrict their propagation into the beam pipe. The cut-off frequency of a transverse electric (TE) propagation mode of a circular waveguide is calculated as [19],

$$f_{c,mn} = \frac{c \times j'_{mn}}{2\pi a}, \quad (2.5)$$

where j'_{mn} is the n^{th} root of the derivative of the m^{th} order Bessel function J_m . Among all TE modes, TE₁₁ mode has the lowest cut-off frequency. All these factors put a lower limit on the cavity radius and an upper limit on the resonant frequency of the dipole mode.

On the other hand, the resonant frequency of the dipole mode should be high enough to have enough EM cycles between two consecutive bunches. Increasing the size of the cavity and overall BPM structure reduces the resonant frequency. These factors put an upper limit on the radius of the cavity and a lower limit on the dipole frequency.

Even after the bunch has passed, the induced EM field in a mode keeps oscillating, with its amplitude decaying exponentially in time. The amplitude decay constant τ of the field of a mode can be calculated as,

$$\tau = \frac{2Q_L}{\omega_{mnp}}, \quad (2.6)$$

where Q_L is the loaded quality factor for the cavity mode, which is calculated as,

$$Q_L = \frac{\omega_{mnp} W_{\text{stored}}}{P_{\text{loss}}}, \quad (2.7)$$

where W_{stored} is the EM energy stored inside the cavity at an instance of time, P_{loss} is the energy lost per unit time. The energy stored inside a cavity can be lost in

two ways; by internal resistive losses in the cavity walls, or it can be extracted out of the cavity. The quality factor can be divided into the internal quality factor Q_0 and external quality factor Q_{ext} . The three Q values are related to each other via,

$$\frac{1}{Q_L} = \frac{1}{Q_0} + \frac{1}{Q_{ext}}. \quad (2.8)$$

The quality factor is a material dependent parameter. To compare the effects of only cavity geometry, a material independent factor known as the normalised shunt impedance R/Q is used. The amount of energy coupled into the cavity from the beam depends on this factor. The R/Q of the TM_{mnp} mode for an x_0 beam position is calculated as,

$$\left(\frac{R}{Q}\right)_{mnp}(x_0) = \frac{V_{mnp}^2(x_0)}{\omega_{mnp} W_{mnp}} = \frac{\left(\int_{-l/2}^{l/2} E_{mnp}(x_0) dz\right)^2}{\omega_{mnp} \frac{\epsilon_0}{2} \oint_{V_{cavity}} |E_{mnp}(r, \phi, z)|^2 dV}, \quad (2.9)$$

where $V_{mnp} = \int_{-l/2}^{l/2} E_{mnp}(x_0) dz$, $E_{mnp}(x_0)$ is the electric field along the beam trajectory, and V_{cavity} is the cavity volume.

Because of the oscillating nature of the EM fields, the field inside the cavity changes while the bunch is still passing through the cavity. It reduces the effective power coupled from the bunch into the cavity, compared to its peak value. This factor is called the transit time factor α_{TT} , which is calculated as,

$$\alpha_{TT}(\beta) = \frac{\sin\left(\frac{\omega_{mnp} l}{\beta c}\right)}{\frac{\omega_{mnp} l}{\beta c}}, \quad (2.10)$$

where $\beta = v/c$ and v is the speed of the bunch. The α_{TT} is used later in this chapter, while calculating CBPM signal amplitude using Eqn. 2.18.

From Eqn. 2.9, the power coupling from the beam to the cavity is limited by the length of the cavity. A very thin cavity will not couple enough power which can be detected. If the cavity is very long, then the transit time factor will reduce the effective coupled voltage. The effects of a slanted orbit or bunch also start to be dominant in a longer

cavity. Choosing the cavity parameters is a trade off between better power coupling and these limiting factors.

The EM field induced inside the cavity is coupled out for detection using different coupling mechanisms, such as a capacitive probe or a magnetic loop. In present designs, slot coupled waveguides are used as shown in the Fig. 2.4(b). The voltage difference across the slot edges generates an oscillating dipole voltage inside the slot. The field inside the cavity is coupled into the waveguides through slots. A rectangular waveguide is preferred as a capacitive coupling probe is more effective with a rectangular structure. The fixed orientation of the EM field in the rectangular waveguide improves the selection of the dipole field of a specific orientation inside the cavity. In addition, the rectangular shape makes the design compact and it is easier to mount a coupling probe on the rectangular surface. The waveguide inherently acts as a high pass filter. The cut-off frequency of a TE_{mn} mode of a rectangular waveguide is given by,

$$f_{c,mn} = \frac{1}{2\pi\sqrt{\mu_0\varepsilon_0}} \sqrt{\left(\frac{m\pi}{A}\right)^2 + \left(\frac{n\pi}{B}\right)^2}, \quad (2.11)$$

where, m and n are the mode numbers, A and B are the longer and shorter dimensions of the rectangular waveguide cross-section respectively.

All frequencies below the cut-off will be attenuated exponentially along the waveguide length. The TE_{10} mode is the fundamental mode of the rectangular waveguide with lowest cut-off frequency, and is utilised as the coupling mode. The dimension of the waveguide is chosen such that the cut-off frequency of the waveguide is higher than the monopole frequency of the cavity, but it is lower than the dipole frequency, which should propagate without any attenuation. So the monopole signal is filtered out in the waveguide itself. In addition, the slots and waveguide adapters can be designed such that, the position signals for x and y (transverse) axes get slightly separated in frequency. This provides an additional opportunity to filter the contribution due to the position offset along the orthogonal axis. This coupled signal is then extracted to a coaxial line for further processing. The coaxial coupler can also be designed to act as a filter for better performance of the system.

a) Beam loading in a cylindrical resonant cavity

The amplitude of the extracted position signal induced by a bunch inside a cavity can be calculated using the fundamental theorem of beam loading. The energy lost in the dipole mode of the cavity W_{110} by a bunch, can be calculated as [21],

$$W_{110} = V_{110}(x) q, \quad (2.12)$$

where V_{110} is the voltage seen by the bunch inside the cavity and q is the bunch charge.

According to the fundamental theorem of beam loading, the bunch sees only half of the voltage induced by it. By rearranging the terms in equation 2.12 and using the theorem of beam loading we get,

$$V_{110} = \frac{\omega_{110}}{2} \frac{V_{110}^2}{\omega_{110} W_{110}} q. \quad (2.13)$$

The internal quality factor for the dipole mode $Q_{0,110}$ can be calculated as,

$$Q_{0,110} = \frac{\omega_{110} W_{110}}{P_{110,\text{loss}}}, \quad (2.14)$$

where $P_{100,\text{loss}}$ is the power dissipated in the cavity walls.

From the definition of the power and Eqn. 2.14, we get the relation between the normalised shunt impedance and induced voltage as,

$$\left(\frac{R}{Q}\right)_{110} = \frac{V_{110}^2}{\omega_{110} W_{110}}. \quad (2.15)$$

From Eqn. 2.13 and 2.15, the induced voltage in the dipole mode V_{110} is,

$$V_{110}(x) = \frac{\omega_{110}}{2} \left(\frac{R}{Q}\right)_{110} (x) q. \quad (2.16)$$

From the definition of external quality factor Q_{ext} and Eqn. 2.15 and 2.16, the power coupled out $P_{110,\text{coupled}}$ from the dipole mode in the cavity, through the waveguide

adapter, into the coaxial line can be calculated as,

$$P_{110,\text{coupled}} = \frac{\omega_{110}^2}{4Q_{110,\text{ext}}} \left(\frac{R}{Q} \right)_{110} (x) q^2, \quad (2.17)$$

where $Q_{110,\text{ext}}$ is the external quality factor for the dipole mode.

If the impedance of the coaxial line is Z_{coax} , the amplitude $V_{110,\text{offset}}$ of the extracted EM oscillating signal, induced due to bunch position offset, can be calculated as [22],

$$V_{110,\text{offset}}(x, t) = \frac{\omega_{110}}{2} \sqrt{\frac{Z_{\text{coax}}}{Q_{110,\text{ext}}} \left(\frac{R}{Q} \right)_{110}} (x_0) q \frac{x}{x_0} \alpha_b \alpha_{TT} e^{-t/2\tau} \sin(\omega_{110}t), \quad (2.18)$$

$$\propto x e^{-t/2\tau} \sin(\omega_{110}t), \quad (2.19)$$

where x_0 is the bunch position for which R/Q is known, α_b is the attenuation factor due to the variation in the induced oscillating EM field over the bunch length, which can be calculated for a bunch with a Gaussian charge distribution along its length as,

$$\alpha_b = e^{\left(-\frac{\sigma_b^2 \omega_{110}^2}{2c^2} \right)}, \quad (2.20)$$

where σ_b is the root mean square length of the charge of the charge distribution.

As shown in the above equation, the amplitude of the CBPM signal is linearly proportional to the beam position offset. The signals induced by bunches with their positions on the opposite side of the cavity centre will be out of phase by 180° with each other. In this way, the amplitude of the CBPM signal gives the value of the bunch position offset, and the phase of the signal gives the direction of the offset with respect to the electromagnetic centre of the cavity.

A typical CBPM signal, calculated using Eqn. 2.18, induced by a single bunch is shown in Fig. 2.5. A CBPM with $R/Q(1\text{ mm})$ of 0.8, and Q_L and Q_{ext} of 250 and 20000 respectively, is considered. A single bunch of electrons, carrying 0.6 nC of charge, passing at 1 mm position offset was considered as a beam. The attenuation due to the transit time and bunch length are neglected. As shown in Fig. 2.5(a) and 2.5(b), the EM signal oscillates at the cavity dipole frequency. The signal has maximum amplitude at the beginning, and it decays exponentially with time.

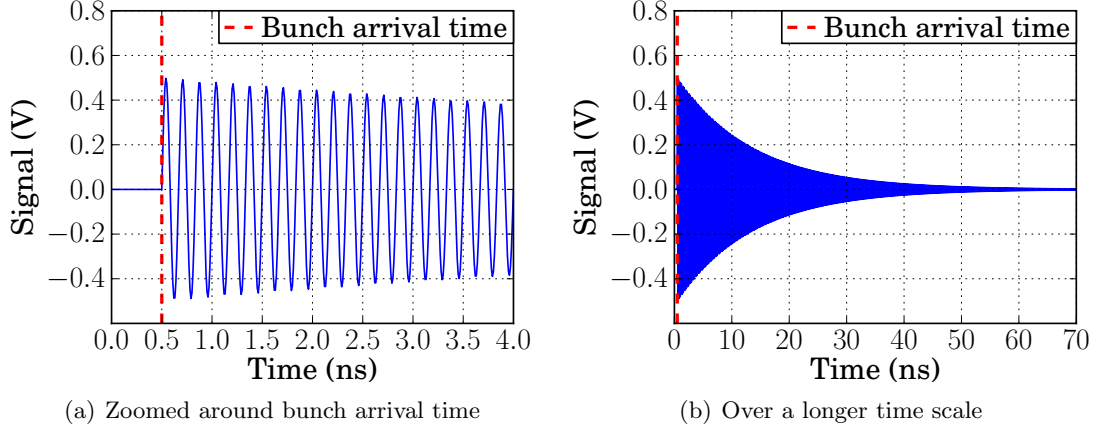


Figure 2.5: Simulated typical CBPM signal, induced by a bunch in a cavity with dipole mode frequency of 6 GHz and Q_L of 250.

Now considering a bunch trajectory passing through the centre of the cavity, but at a small angle θ with respect to the cylindrical axis. In the limit of a shorter cavity, the signal induced by the tilt reduces to [22],

$$\begin{aligned}
 V_{\theta,110}(t) &\cong \frac{\omega_{110}}{2} \sqrt{\frac{Z}{Q_{ext}} \left(\frac{R}{Q}\right)_{110}} (x_0) \alpha_b \frac{q \tan \theta}{lx_0} \\
 &\times e^{-t/2\tau} \cos(\omega_{110}t) \left\{ \frac{2c^2 \cos^2 \theta}{\omega_{110}^2} \sin\left(\frac{\omega_{110}l}{2c \cos \theta}\right) - \frac{lc \cos \theta}{\omega_{110}} \cos\left(\frac{\omega_{110}l}{2c \cos \theta}\right) \right\}, \\
 &\propto \theta e^{-t/2\tau} \cos(\omega_{110}t). \tag{2.21}
 \end{aligned}$$

Similarly if a bunch passes with its centroid moving along the z -axis, but the bunch is tilted by an angle α to the z -axis, a signal $V_{\alpha,110}$ will be induced. The signal induced by such a bunch can be calculated by slicing the bunch along the z -axis and calculating the signals induced by the fractional charge stored in each slice. The net signal calculated by vector addition of the individual signals can be written as [22],

$$\begin{aligned}
 V_{\alpha,110}(t) &\cong -\frac{\omega_{110}}{2} \sqrt{\frac{Z}{Q_{ext}} \left(\frac{R}{Q}\right)_{110}} (x_0) \frac{q\omega_{110}\sigma_z^2 \tan(\alpha)}{x_0 c} \\
 &\exp\left(-\frac{\omega_{110}^2 \sigma_z^2}{2c^2}\right) e^{-t/2\tau} \cos(\omega_{110}t), \\
 &\propto -\alpha e^{-t/2\tau} \cos(\omega_{110}t). \tag{2.22}
 \end{aligned}$$

It is clear from equations 2.18, 2.21 and 2.22 that the signals generated by the position offset and angular tilts are 90° out of phase with each other. The total signal will be the linear combination of the position and tilt signals. Generally for a small tilt angles, the position signal is dominant.

For smaller values of position offset, the amplitude of the field induced by a bunch in the monopole (TM_{010}) mode of a cylindrical cavity is only sensitive to the charge and length of the bunch, not the position offset. The BPM signal is normalised for its dependence on the bunch charge and length with the monopole signal from a reference cavity. The reference cavity is designed such that the resonant frequency of its monopole mode is equal to the dipole frequency of the position cavity.

Cavity BPMs are normally used in high energy electron colliders and light sources. In as early as 1999, V. Balakin *et al* tested a cavity BPM triplet setup and showed position resolution of 150 nm [23]. While testing their design, V Sargsyan and collaborators faced problems with the low available bunch charge and large beam jitter, and could extract resolution of $470 \mu\text{m}$ [24]. M. Slater *et al* tested many BPMs during their experiments on a prototype energy spectrometer and recorded minimum resolution of 170 nm [25]. S. Boogert *et al* recorded consistent position resolution of 200 nm and the highest resolution of 27 nm over a shorter time spans [26]. These are the resolutions measured for cavities with relatively higher Q_L values of the order of 5000 and moderate beam coupling strength. Cavities with lower Q_L values of the order of 50 are also designed for faster measurements. H. Maesaka *et al* reported development of a cavity BPM for XFEL/SPRING-8, with Q_L of 50 and measured position resolution of 230 nm [27]. Y. Honda *et al* from KEK reported design of low Q_L cavity BPM to use near the interaction point of ATF2 and tested its resolution to 8.7 nm [28], which is the best resolution recorded till today.

2.3 Advantages and applications of cavity BPMs

The major advantage of a CBPM is its linear response to the beam position offset. Linear response improves the accuracy of the measurement interpretation and system

calibration. For a cavity with relatively higher Q_L value, the cavity signal is available for a longer time which makes it possible to efficiently isolate the dipole signal. The other techniques involve subtraction of two large signals even near the BPM centre, which limits their measurement resolution.

The beam positions measured by the CBPMs can be used to determine and verify the parameters of machine lattice components. For example, if the beam trajectories before and after a dipole magnet can be calculated accurately, the magnetic strength can be determined and compared to the expected value. If the power supply of a magnet becomes unstable during beam operation, the amplitude of beam position jitter in the down stream CBPMs will increase, which can be used to find the faulty magnet and supply. If any transverse wakefield has build up in the accelerating cavities, it will also kick the beam and increase beam emittance. The kick due to the wakefield can also be measured as a position change in the down stream CBPMs. The variation in beam energy due to errors in the acceleration units, or beam arrival time, can be measured using an energy spectrometer [25], in which the difference in bunch position and trajectory measured at the CBPMs situated downstream from a dipole magnet are used to determine the variation in the beam energy.

The beam positions determined from the CBPMs can be given to a position and angle feedback system to correct the trajectories of the following bunches, in the same [29] or next bunch train. If the parameters of machine lattice components are kept constant, the trajectories of a bunch can be predicted for different initial positions and angles, as their values before and after the lattice components can be related by their well defined transfer functions [6]. In circular particle accelerators, the bunch positions measured during a revolution are used to calculate the amount of kick required to correct its trajectory during the next revolution [30]. In linear accelerators, the measured positions of the bunches at the beginning of a train are used to correct the trajectories of the following bunches in the same train, or in the next train. The intra-train feedback systems are limited by the amount of time required to calculate the bunch positions and to generate the corresponding kick.

2.3.1 Beam based alignment

In an accelerator, specially those using low emittance beams, it is essential to align the optics elements accurately to satisfy the requirements of small emittance dilution and orbit distortion. The dipole field kick errors experienced by a beam while passing through quadrupole magnets at off-centre positions deviate the beam from its ideal orbit and increase the emittance of the beam [31, 32]. To improve the relative alignment of the machine optical elements and correct for fabrication and mechanical alignment errors, the elements are aligned using a beam-based alignment (BBA) technique [33, 34, 35].

Quadrupole and sextupole magnets have field patterns, such that a beam passing through their centre will not experience any dipole field. In this case, changing the strength of the magnet should not affect the beam trajectory. If the beam is passing off centre through the magnet, the beam experiences kick accordingly. The amount of kick the beam experience is linearly and non-linearly proportional to the distance from the magnetic centre of the quadrupole and sextupole respectively. The change in the trajectory is measured by BPM(s) situated down stream from the magnet. For a beam passing at a constant position offset through the magnet, changing the magnet strength changes the amount of kick experienced by the beam, which changes the position reading in the BPM. To align the magnet, the magnet position is scanned, and at each magnet position the magnet strength is varied. The amount of kick experienced for each magnet strength is recorded as a position variation in the BPM. The magnet position where the variation in the BPM output is minimum, for the variation in magnet strength, gives the magnetic centre. Because a cavity BPM can differentiate smaller position changes, it can measure the smaller trajectory variations with more accuracy, and hence improve the accuracy of alignment.

2.4 Overview of research chapters

The goals of this research were to develop design and analysis techniques for cavity beam position monitor systems for future high energy electron accelerators. The studies presented in this thesis are motivated towards development of a CBPM system for the

main linac section of the proposed CLIC collider.

The proposed layout and working principle of CLIC are discussed briefly at the beginning of chapter 3. The constraints applied by the machine parameters on the choice of the design parameters and signal analysis techniques for the CBPM system are explained. The effects of cavity parameters on the CBPM signals are discussed. The key research areas, such as overlapping of signals from closely spaced bunches and requirement for a simpler and efficient CBPM design, are identified. As CLIC was still in technical design stage, the identified topics were studied through collaborative projects with the institutions having operational accelerator facilities, such as Accelerator Test Facility (ATF) at KEK in Japan, and Diamond Light Source in UK. Most of the beam testing presented in this thesis was carried at ATF to benefit from an already operational CBPM system and stable beam with shorter bunches.

In chapter 4, a method developed to analyze CBPM signals induced by closely spaced bunches is discussed. After explaining the layout and working principles of the ATF, the CBPM system installed on the ATF2 extraction line is discussed. A signal processing method for CBPM signals induced by an individual bunch is explained in detail. The development of a CBPM signal induced by multiple bunches, closely spaced in time, is explained. The working principle of a method to remove the signal pollution from previous bunches is discussed. Results from testing of the method on the CBPM signals induced by beam and simulated signals are presented in this chapter. A code to simulate the signals induced in a CBPM by a bunch train is presented in this chapter. The effects of the signal processing parameters on the performance of the method are discussed in detail. A study of the effects of temperature variation on the cavity parameters is also presented in that chapter.

The design ideas for a large scale CBPM system are discussed in chapter 5. Different ideas are tested individually by EM simulations before testing them together on a complete CBPM geometry. The results of EM simulations of the CBPM structures are compared in this chapter. The RF test measurements of a fabricated cavity are presented and their results are compared to the simulation results. The possible reasons for the differences between the parameters of a fabricated cavity and those predicted

from the EM simulations are explored using simulation reconstructions of various fabrication errors. Results from the initial beam tests carried at ATF2 are also presented in the chapter.

The results from the development and testing of a multi-bunch signal processing method and CBPM prototype are summarised in chapter 6. The effects of additional information and advantages brought by these studies to the CBPM design, signal processing and applicability of the high Q CBPMs on various accelerators are discussed in the chapter. The research topics, identified during the course of the presented work, for further studies are discussed at the end of the chapter.

Cavity BPM system for CLIC main linac

In the CLIC main linac, the bunch trains will be accelerated from 9 GeV to 1.5 TeV. Each train will have 312 bunches of 0.6 nC, separated by 0.5 ns. The main linac is designed to fulfil very stringent restrictions on beam emittance growth. The beam emittances at the output of damping rings will be 500 and 5 nm along the x and y axes respectively. The target luminosity for CLIC is $2 \times 10^{34} \text{ cm}^{-2}\text{s}^{-1}$. To achieve this goal, the beam emittance in x (ε_x) and y (ε_y) will need to be maintained below 660 and 20 nm [12] respectively. This leaves little room for the total emittance growth in the RTML and main linac sections. The emittance growth windows of 30 and 5 nm in x and y are for the static (errors in alignment of quadrupole magnets and BPMs etc), and dynamic (fluctuations in quadrupole magnet current etc) errors.

The primary alignment of various machine components in the main linac section will be carried out using a Metrologic Reference Network (MRN). The MRN will use overlapping wires to align the machine components over a 200 m length, with an accuracy of 5-20 μm . The alignment in the main linac section will further be improved using the BBA techniques [12], as discussed in section 2.3.1.

To apply BBA techniques, the main linac will be instrumented with 4196 BPMs, one BPM attached to almost every magnet. As explained in section 2.3.1, the BBA techniques require precise position measurements down-stream to a magnet. The main

requirements and important machine parameters for the BPM system on the main linac are listed in Table 3.1. The required position resolution of the order of 50 nm has already been demonstrated by the existing CBPM systems [26, 36].

Table 3.1: BPM requirements for CLIC main linac.

Parameter	Value	Unit
Resolution	50	nm
Accuracy	5	μm
Bandwidth	100	MHz
Number of BPM required	4196	
Drift tube diameter	8	mm

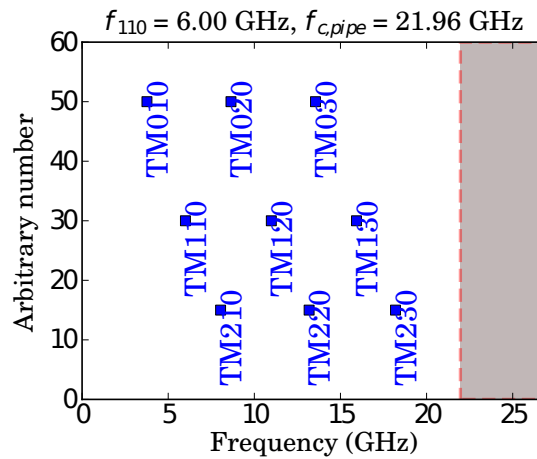
The CLIC main linac will have beam accelerating structures consuming several megawatt of power at 12 GHz and an RF signal of the same frequency will be distributed along the linacs for the purpose of synchronisation of different devices. The same RF signal can be used in the electronic processing of the cavity BPM signals. Using that signal will provide a stable phase relation with the machine RF, which is essential for position measurement. It will be beneficial to keep the CBPM frequency at, or near, a harmonic or sub-harmonic of the machine RF frequency.

3.1 Frequency regions for CBPM design and electronic signal processing

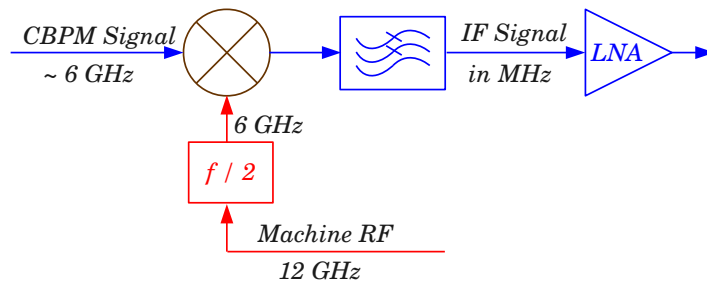
In the proposed design, the CBPMs will sit next to the accelerating structures operating at MW power levels. Detecting the μW power induced inside a CBPM at the same frequency can be difficult in the presence of the noise due to possible RF power leakage from the accelerating cavities and power distribution system. The frequency region near 12 GHz should be avoided as a CBPM frequency to reduce the background noise signal and for the safety of the processing electronics.

As discussed in the chapters 2 and 5, the maximum value of a CBPM frequency is limited by the cutoff frequency of the beam pipe attached to it. From Eqn. 2.5, a beam pipe with 4 mm radius will have a cutoff frequency $f_{c,\text{pipe}}$ of 21.96 GHz. Fig. 3.1(a)

shows the frequencies of the major TM modes of a pillbox cavity, calculated using Eqn. 2.4, designed to set its dipole mode at 6 GHz. All of the first three monopole, dipole and quadrupole modes are well below the cutoff frequency of the beam pipe. Neither of these modes will propagate along the beam pipe, nor will they affect the beam passing through the beam pipe. Fig. 3.1(b) shows a block diagram of a simple signal processing scheme for CBPM signals near 6 GHz. The functions of every circuit components in the diagram are explained in section 4.2.1 further in this thesis. The 12 GHz reference signal from the machine can be converted to 6 GHz using an $f/2$ frequency divider. To process the signals in a homodyne mode, the cavity should be designed at exactly 6 GHz. To process the signals in a heterodyne mode, the cavity can be detuned from 6 GHz, and the down converted Intermediate Frequency (IF) signal of few MHz frequency can be digitised for further digital processing.



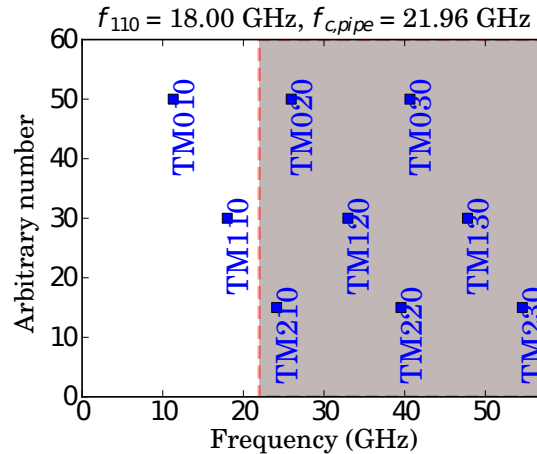
(a) Resonance frequencies of major TM modes in comparison to beam pipe cutoff frequency $f_{c,pipe}$.



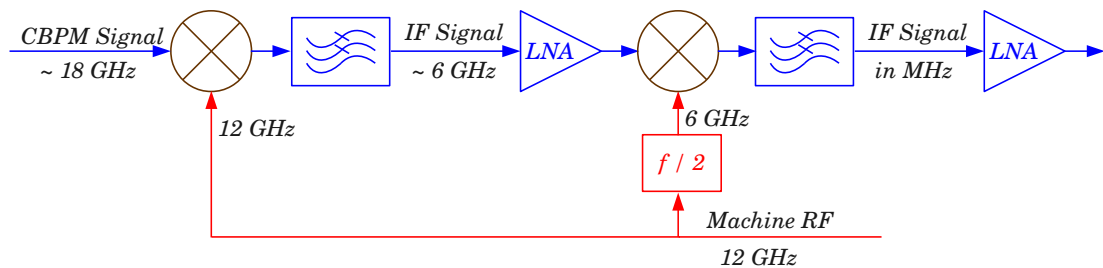
(b) Basic diagram of a signal processing scheme.

Figure 3.1: Resonance frequencies of major TM modes and signal processing scheme of a CBPM with dipole mode frequency f_{110} near 6 GHz.

Above the machine RF frequency, the next convenient frequency to design the CBPM system can be 18 GHz. Fig. 3.2(a) shows the resonant frequencies of the TM modes, calculated using Eqn. 2.4, of a pillbox cavity with its dipole at 18 GHz. All TM modes above the dipole will have resonant frequencies higher than the cutoff frequency of the beam pipe, and may affect the beam while propagating along it.



(a) Resonance frequencies of major TM modes in comparison to beam pipe cutoff frequency $f_{c,pipe}$



(b) Basic diagram of signal processing scheme

Figure 3.2: Resonance frequencies of major TM modes and signal processing scheme of a CBPM with dipole mode frequency f_{110} near 18 GHz

A signal at 18 GHz can be down converted in two stages, or in a single stage. A scheme with two stages of electronic down conversion is shown in Fig. 3.2(b). In this scheme the CBPM signal at 18 GHz will be mixed with the machine RF reference signal at 12 GHz to down convert it to 6 GHz. In the next stage of processing, the 12 GHz machine reference signal will be converted to 6 GHz using a frequency divider, and will be used as an LO signal to further down convert the 6 GHz IF signal. If a CBPM is designed exactly at 18 GHz, the second stage will act as a homodyne down converter.

For a detuned CBPM, the IF signal is in the MHz frequency range, the second stage IF can be digitised for further processing. Frequencies between 6 and 18 GHz and their processing schemes are also being investigated for the project.

3.2 Effect of CBPM frequency on bunch train signal

The EM fields induced in a cavity by individual bunches can be linearly added to get the resultant signal. The possible cavity BPM signals induced by a CLIC bunch train in the CBPMs of different frequency and Q values can be predicted using the signal simulation code discussed in the Section 4.3. If the signal amplitude grows with time, it can saturate the processing electronics. In such a case the signal has to be attenuated in advance, or actively during the bunch train. Attenuating the signal degrades the system resolution. To limit the amplitude growth, the effects of the cavity frequency and Q values on the relative amplitude growth of the net signal are studied and presented below in this section.

Fig. 3.3(a) and 3.3(b) shows the signal induced by a bunch train, with a constant position offset, in a cavity with dipole mode at 6 GHz and Q_L of 250. Because of the smaller bunch separation of 0.5 ns, the next bunch arrives before the signal induced by

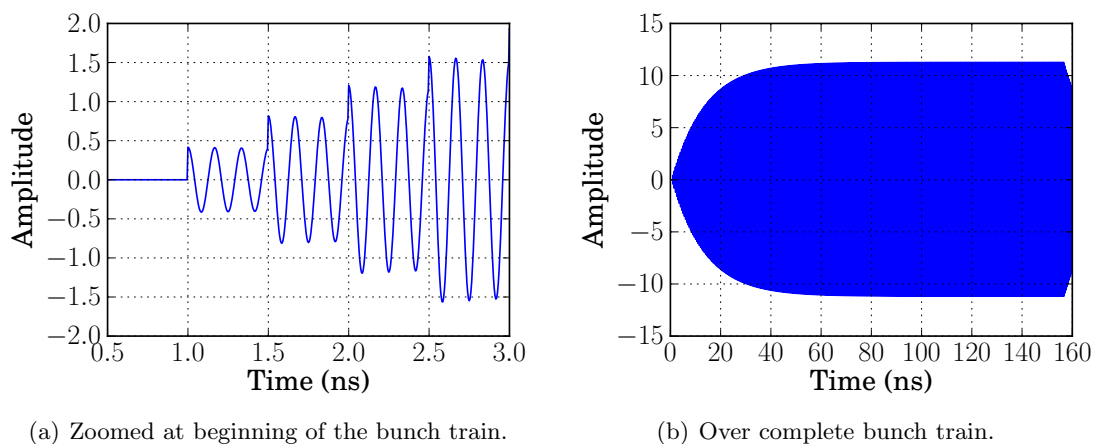


Figure 3.3: Simulated CBPM signal induced by a bunch train in a cavity with dipole mode at 6 GHz and Q_L of 250, showing the change in signal amplitude as a function of time.

a bunch has decayed. Because 6 GHz is a harmonic of the bunch repetition frequency (2 GHz), the fields induced by each bunch will add constructively, so the net signal amplitude will grow. The rate of signal amplitude growth decreases with number of bunch passage, because the amplitude of signals induced by previous bunches decay with time. The amplitude stops growing after some time depending on the Q_L of the cavity.

If the dipole frequency is detuned by 100 MHz from the exact harmonic frequency of 6 GHz, as shown in Fig. 3.4, the signals induced by the two consecutive bunches will be at a phase difference of 0.31 radian. Because of the phase difference, the net signal amplitude after two bunches will be lower than in the 6 GHz case. With this phase difference, the signal from bunch one will be out of phase with the signal from bunch six. As shown in Fig. 3.4(b), the net signal amplitude will oscillate before stabilizing towards end of the bunch train.

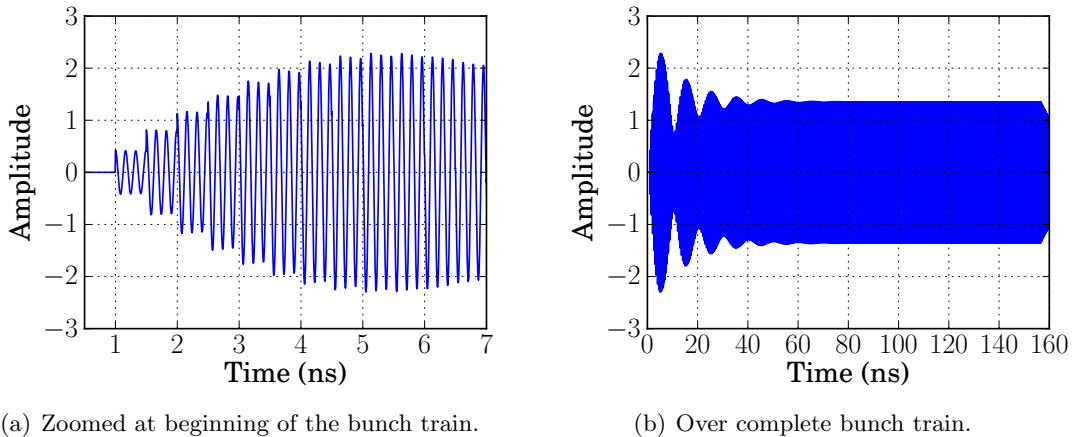


Figure 3.4: Simulated CBPM signal induced by a bunch train in a cavity with dipole mode at 6.1 GHz and Q_L of 250, showing the change in signal amplitude as a function of time.

The cavity signal looks completely different if the cavity is designed with a dipole frequency at 7 GHz. The signals induced from consecutive bunches will be out of phase with each other. As shown in Fig. 3.5(a), the signals from consecutive bunches adds destructively and the signal amplitude decreases with each bunch passage. In this case, the signal amplitude can get very small for alternate bunches, reducing the measurement accuracy. The signal amplitude growth can be restricted by choosing an

appropriate resonance frequency for any mode. The same principle can be used to restrict the growth of the monopole field inside the cavity. As the monopole modes are much more strongly coupled to the beam, the cavity must be designed such that the induced wake-fields in the monopole mode by different bunches do not add constructively, and disrupt the beam itself.

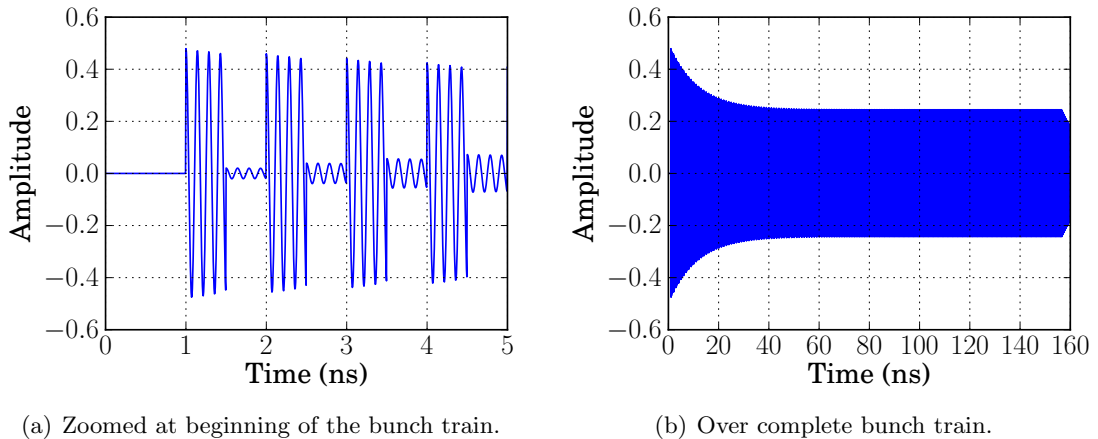
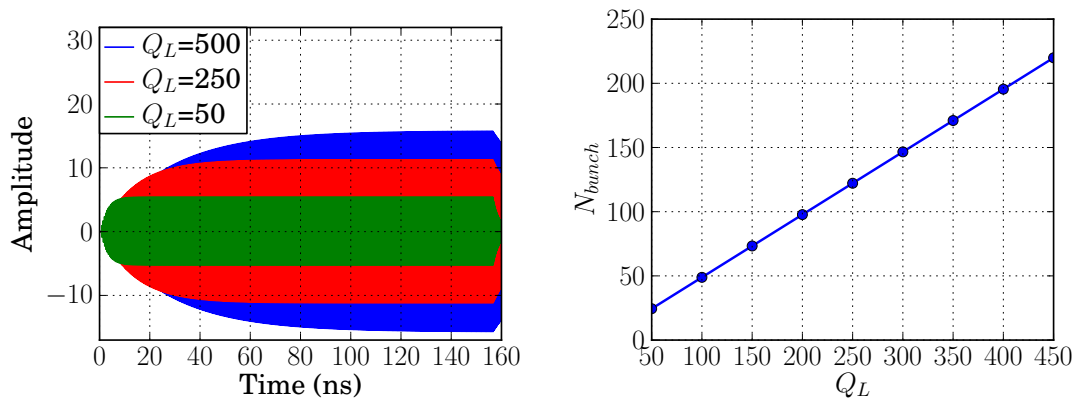


Figure 3.5: Simulated CBPM signal induced by a bunch train in a cavity with dipole mode at 7 GHz and Q_L of 250, showing the change in signal amplitude as a function of time.

The growth of the signal amplitude can also be restricted by damping the field induced inside the cavity. As discussed in Section 2.2.1, the induced power can be damped in the cavity walls (Q_0) and it can be extracted out of the cavity (Q_{ext}). Fig. 3.6(a) shows the signal induced by a bunch train inside a cavity with the dipole mode at 6 GHz, and different Q_L values. The smaller value of Q_L means that the field induced by a bunch will get damped rapidly and the maximum signal amplitude is lower. In addition, the signal amplitude stabilises quickly for a cavity with smaller Q_L . The same issue can be looked in terms of the signal pollution from previous bunches. Fig. 3.6(b) shows the number of previous bunches N_{bunch} whose induced signal has not decayed to lower than 1% of its initial amplitude. With decrease in the Q_L , the N_{bunch} also decreases, showing decrease in the signal pollution.

One of the reason why cavity BPMs can provide higher resolution is their relatively narrow band signal available for a longer time. When the Q values of a CBPM are reduced below certain level, it begins to lose these advantages. Decreasing the Q of a



(a) Simulated bunch train signal from a cavity with different Q values, $Q_0=Q_{ext}=2Q_L$.

(b) Number of previous bunches with amplitude pollution greater than 1%.

Figure 3.6: Change in signal pollution with change in Q_L values of a cavity with dipole mode at 6 GHz

cavity increases the frequency bandwidth of its modes, and hence the pollution from the tails of the monopole modes. A CBPM should be designed with sensible Q values, low enough to restrict the amplitude growth, but not permit too much contamination from monopole modes.

3.2.1 Design challenges

Even though the required position resolution of 50 nm has already been demonstrated by existing CBPM systems, the high beam current of 1.2 A, large scale of the system and compact bunch spacing of 0.5 ns at CLIC present unique challenges in terms of physics and engineering. The major research topics affecting the performance and design of the CBPM system were identified. Because CLIC is still in its design stage, most of the experimental studies were carried out in collaboration with other institutes with operational accelerators, such as ATF at KEK in Japan and Diamond Light Source in UK.

- The ambient temperature in the tunnel is estimated to change by 20 °C during start up of beam operations. The cavity geometry will change with the temperature due to the expansion and contraction of the metal. The variation in the

geometry will change the CBPM parameters, such as the resonant frequency and coupling. The effect of the temperature change on the frequency of a CBPM was studied using the CBPM system at ATF2, which is presented in Chapter 4.

- CLIC will accelerate a bunch train formed of 312 bunches separated by 0.5 ns in time. Because of such a small temporal bunch separation, the next bunch will arrive before the fields induced by previous bunches will have decayed. The CBPM signal from a bunch will be polluted by the signals induced from previous bunches. The CBPM signals from multiple bunches and a method developed to remove the signal pollution are discussed in detail in Chapter 4. The method was tested on the CBPM signals induced by multiple bunches in CBPMs at ATF2.
- The main linac section is proposed to have 4196 CBPMs. For a system with such a large number of cavities, the cost of fabrication, characterisation, optimisation and operation must be minimised by keeping the design of the CBPM simple. The features, such as mechanical tuning, causing vacuum and fabrication failures should be removed and the ways to work around them must be studied. These features were studied during a project to design a CBPM system for the NLS-Diamond Light Source, which are presented in Chapter 5.

Multi-bunch signal processing

The electromagnetic (EM) field induced by each bunch traversing through the cavity continues to oscillate even after the bunch has passed. The amplitude of the field decays exponentially with time. In the case of the CLIC main linac and beam delivery system, because of the smaller bunch spacing in time, the next bunch will arrive before the fields induced by the previous bunches will have decayed. The fields induced by many bunches will overlap and the output signal from a bunch will be polluted by the signals induced from the previous bunches. A bunch position determined from a signal polluted by the previous bunches signals will be erroneous. A method was developed to remove this signal pollution using a signal subtraction algorithm. The method was tested on the signals from the CBPM system at the Accelerator Test Facility (ATF) extraction line. The cavity signals induced by multiple bunches were simulated and the performance of the algorithm was verified.

In this chapter, after introducing the ATF and CBPM system on the ATF2 extraction line, the working principle of the signal subtraction algorithm is explained. The application of the method on the signals induced by multiple bunches in the CBPMs at ATF2 and on the simulated signals are presented. The effects of the system parameters and signal processing parameters on the performance of the multi-bunch analysis are also discussed.

4.1 Accelerator Test Facility

The ATF machine is designed to generate a beam with extremely small transverse emittance. It has successfully decreased the emittance to a level which makes it almost an ideal place to test the concepts for the proposed International Linear Collider (ILC). The ATF2 extraction line at the ATF is built as a continuation of the ILC research program [37], motivated by the excellent results obtained at the Final Focus Test Beam (FFTB) facility at SLAC [38]. Fig. 4.1(b) shows the layout of ATF machine with an enlarged view of the ATF2 extraction line shown in Fig. 4.1(a). Typical operation values of the major parameters of the ATF machine are listed in Table 4.1.

Table 4.1: Typical operation values of the major parameters of the ATF.

Parameter	Value	Unit
Linac		
Length	85	m
RF Frequency	2856	MHz
Accelerating field (nominal)	33	MV/m
Feed peak power	200	MW/structure
Number of bunches	1 - 20	
Bunch Separation	2.8	ns
Damping ring		
Energy	1.29	GeV
Revolution frequency	2.16	MHz
RF frequency	714	MHz
Bunch train repetition frequency	1.5	Hz
Extracted emittance $\gamma\epsilon_x$ & $\gamma\epsilon_y$	2 & 0.5	nm
Bunch charge (Number of electrons per bunch)	1.6 (10^{10})	nC (electrons)

A photo-cathode based RF electron gun [39] can produce a train of up to 20 bunches, with a bunch separation of 2.8 ns, which goes into a pre-injector. The pre-injector is designed to accelerate the electrons to form an 80 MeV beam made of a single or multiple bunches [40]. The buncher system consists of a subharmonic buncher at 357 MHz and a traveling wave buncher at 2856 MHz. The pre-injector linac is equipped with instruments for bunch by bunch measurements, including button BPMs for beam position measurement. The regular linac section consists of 16 accelerating structures

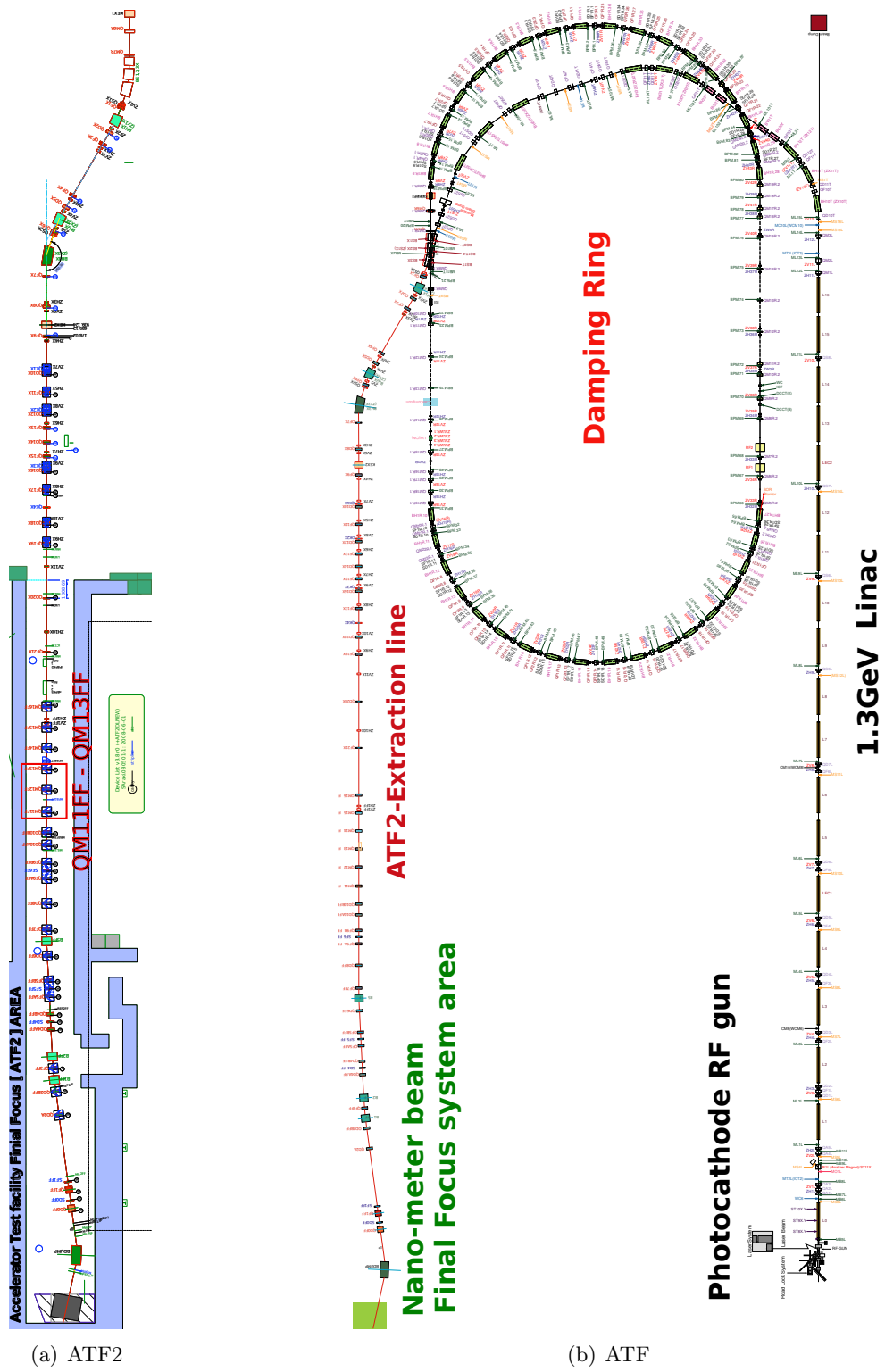


Figure 4.1: Layout of the ATF and ATF2 extraction line [37].

at 2856 MHz. Combined with the pre-injector, the ATF linac provides a nominal acceleration gradient of 33 MV/m.

The accelerated beam is injected into a damping ring (DR) to reduce the transverse emittance by radiation damping [41, 42]. The damping ring is designed to store up to 5 trains of 20 bunches. During the commissioning of the DR, the beam emittance could be reduced to 2 and 0.5 nm in x and y -axes respectively [42]. Two straight sections contain the RF cavities as well as the injection and extraction septa. Along with beam profile and synchrotron radiation monitors, the DR is equipped with 96 button BPMs.

4.1.1 Operation of the ATF in multi-train mode

For a 1.29 GeV beam of electrons, the revolution frequency in the DR is 2.16 MHz [43]. There are 330 buckets formed by the RF system operating at 714 MHz. The timing system is designed such that the 20 bunches in the train, with bunch separation of 2.8 ns, fill the alternate buckets. To study the processing of CBPM signals from multiple bunches at ATF, a bunch separation of order of 150 ns was required. To generate bunch separations of more than 2.8 ns, the machine was operated in a multiple train mode, where the DR was filled with bunch trains of a single bunch. The individual trains were timed to fill specific buckets, and could be separated in time by a value which is an integer multiple of 2.8 ns. Once damped, the bunches are extracted during a single extraction kicker pulse into the ATF2 extraction line.

4.2 Cavity BPM system at ATF2

ATF2 propagates a low emittance beam extracted from the DR of ATF [37]. It was built to study beam delivery systems (BDS) for ILC and CLIC. The design goals of the ATF2 are to demonstrate the following,

- feasibility for ILC type final focus system (FFS),
- 37 nm vertical beam size,

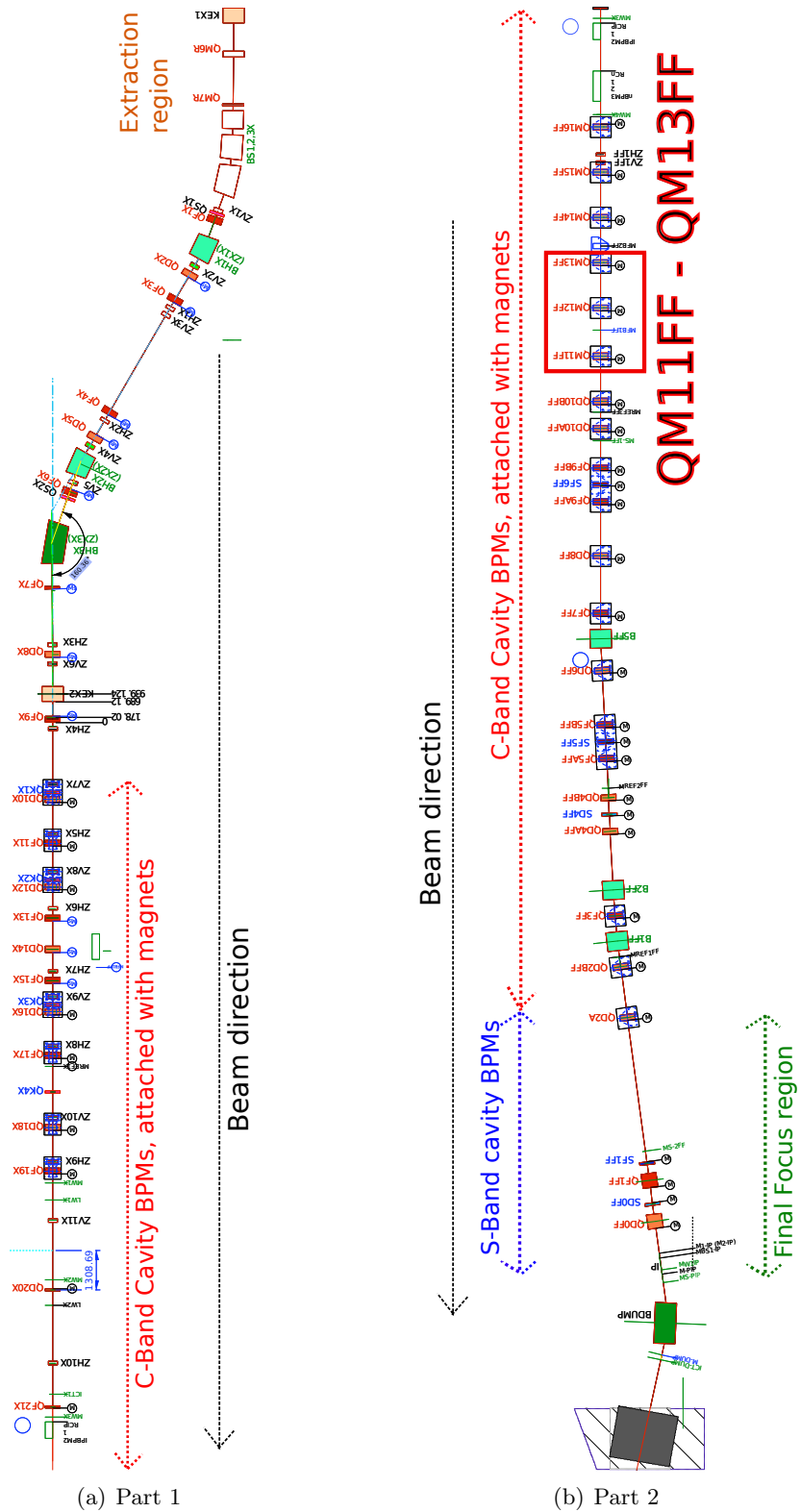


Figure 4.2: Enlarged layout of ATF2 extraction line showing accelerator beam optics components and cavity BPMs [37].

- optics, dispersion, coupling, beam based alignment (BBA) and nanometer level beam control.

To achieve these goals, along with the beam optics components, the ATF2 is equipped with state of the art diagnostics systems [44], including optical transmission radiation (OTR) screens [45], laser wire system [46], Shintake beam size monitor [47] and cavity BPMs [26].

As shown in Fig. 4.2, the CBPM system at the ATF2 has 41 cavities at C- and S-band frequencies, attached to the quadrupoles along the beam line. Among the 41 cavities, there are 36 dipole and 5 reference cavities. The main parameters of the cavities and their functions are listed in Table 4.2. The position signal is measured using a dipole cavity. A monopole cavity serves as a reference cavity; its signal is used to charge normalise the dipole signal and to provide a reference for bunch arrival time. All of the dipole cavities are rigidly mounted on the pole face of the magnets, and the magnets in the final focus system are mounted on precision mover systems. From each dipole cavity, both x and y position signals are recorded.

Table 4.2: Parameters and functions of BPM cavities on ATF2.

Frequency (GHz)	Mode	Measurement	Quantity (cavities)	Q_L approximate
6.42 (C-Band)	Dipole	Position	32	6000
	Monopole	Charge	4	7000
2.88 (S-Band)	Dipole	Position	4	1700
	Monopole	Charge	1	1400

4.2.1 Signal processing

A signal coupled out of a cavity can either be analysed in analog or digital form. Controlling the processing parameters in analog processing is complex due to RF phase locking, electronic non-linearities, environmental drifts and the fixed nature of electronic components. Changing a parameter in analog processing requires more time and it is more expensive compared to digital techniques. On the other hand, computation cost has reduced drastically due to advancements in computer technology. It is much

easier to choose and change the processing parameters digitally, compared with analog processing. Reprogramming capability and cost effectiveness makes digital processing the best choice for the final signal analysis.

The frequency of the output signal of a cavity is typically greater than 2 GHz. As no digitisers are available with such a high digitisation rate and high bit resolution (>10 bits), the high frequency RF signal can not be directly digitised. The output signal is processed in two frequency down conversion stages (heterodyne processing scheme). The first stage is analog, where the cavity output signal of GHz is down converted to a signal of MHz. Then the MHz signal is digitised and processed digitally.

a) Analog signal processing and frequency down conversion

Each cavity at ATF2 is processed by an individual processing card with two channels, a channel to process the x and y position signals each. The processing electronics for a single channel is shown in Fig. 4.3. In addition to the dipole mode, the signal coupled out of a cavity also contains the EM fields coupled from other resonant modes. Only the signal at the dipole frequency is selected using a band pass filter (BPF). The coupled RF signal is in the frequency range of many GHz. The coupled signal is down converted using a mixer driven by a local oscillator (LO), to an intermediate frequency (IF). The process can be described as,

$$2 \cdot \sin(\omega_{RF}t) \times \sin(\omega_{LO}t) = -\cos((\omega_{RF} + \omega_{LO})t) + \cos((\omega_{RF} - \omega_{LO})t), \quad (4.1)$$

where ω_{RF} and ω_{LO} are the angular frequencies of the cavity and LO signals.

The high frequency component $(\omega_{RF} + \omega_{LO})$, is removed using a low pass filter (LPF). A wider range of circuit components, such as filters with steep frequency response, are available at the IF (MHz) frequency range, which provide design flexibility and cost efficiency. To increase the sensitivity, the IF signal is amplified using a low noise amplifier (LNA). The higher frequency components generated due to the non-linearities in the amplifier can be filtered out using an additional IF low pass filter after the LNA.

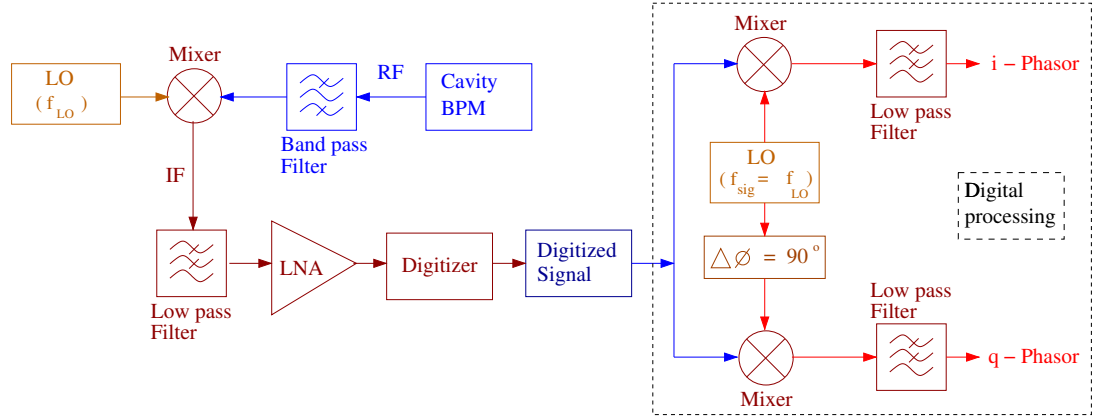


Figure 4.3: Block diagram of typical a typical single channel analog and digital processors.

The LO-frequency for C-band cavity signals is 6452 MHz and for S-Band it is 2856 MHz. The IF frequencies are of the order of 26 MHz for C-band and 34 MHz for S-Band cavities respectively. The filtered signals are digitised using 14 bit digitisers sampling at 104 MHz [26].

Every electronic system has inherent noise generated due to different effects. Based on their origin and distribution, most of the noise can be classified as thermal noise, shot noise or flicker noise [48]. The reduction in the signal to noise ratio at the output of the electronics system can be calculated from the total noise figure F_{total} as [19],

$$\frac{S_o}{N_o} = \frac{1}{F_{\text{total}}} \frac{S_i}{N_i}, \quad (4.2)$$

where S_o and N_o are the amplitudes of the signal and noise voltage at the output, while S_i and N_i are signal and noise voltage amplitudes at the input. The input thermal noise power can be calculated as [49],

$$v_n = \sqrt{4Rk_B T \Delta f}, \quad (4.3)$$

where R is input load resistance, k_B is the Boltzmann constant, T is the temperature of resistance and Δf is the frequency bandwidth. For a multi-element system with many stages, the total noise figure can be calculated as,

$$F = F_1 + \frac{F_2 - 1}{G_1} + \frac{F_3 - 1}{G_2 G_3} + \frac{F_4 - 1}{G_2 G_3 G_4} + \dots, \quad (4.4)$$

where the subscript numbers represent different elements of the circuit, while G is the gain or attenuation of the elements. From the above equation, the signal to noise ratio increases by factor G , except the first element. Because of this it is important to choose the first amplifier, and the components before that, with low noise.

One of the down-converter cards used to process the CBPM signals was tested for its noise and gain characteristics. A block diagram of the test instrument setup is shown in Fig. 4.4. The RF source (Hittite HMC-T2100) is connected to the input of the electronics through a variable attenuator.

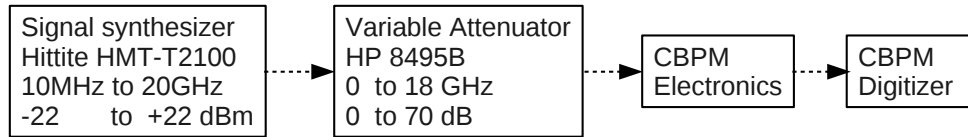
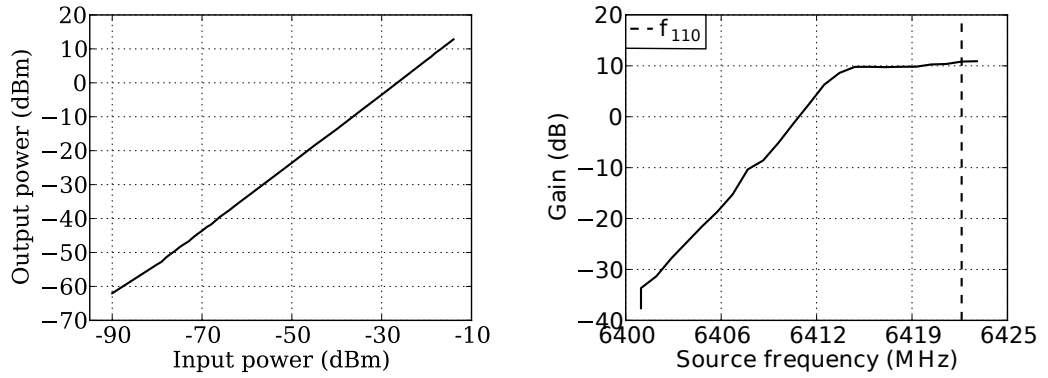


Figure 4.4: Block diagram of the test setup to measure the gain and bandwidth of a CBPM electronics card.

To measure the net system gain, the input power level was varied and the electronics output power was measured. The source power could be changed only between -20 to +20 dBm. The source frequency was set at 6423 MHz, which is a typical signal frequency for C-band CBPMs. A discrete 10 dB step attenuator was used to attenuate the source power up to a maximum of 70 dB. To obtain input power steps of less than 10 dB the source power output could be varied down to 0.1 dBm. Fig. 4.5(a) shows the output power for different input power levels. The plot shows that the noise floor of the electronics is less than -90 dBm. The output power varies linearly with input power, with gain of 27 dB.

To measure the bandwidth of the system the source frequency was changed while keeping the source power constant at -16 dBm. The source frequency was scanned from 6423 to 6403 MHz, and the output power was measured. The net gain observed with signals of different frequencies are plotted in Fig. 4.5(b). The system gain began to compress below 6415 MHz, and decreased by 3 dB at 6413 MHz. The signal frequencies for all CBPMs are above 6420 MHz, where the gain is constant. The cavity output signals are processed using these electronic channels and the down-converted IF signals



(a) Output power of an electronics for different input power

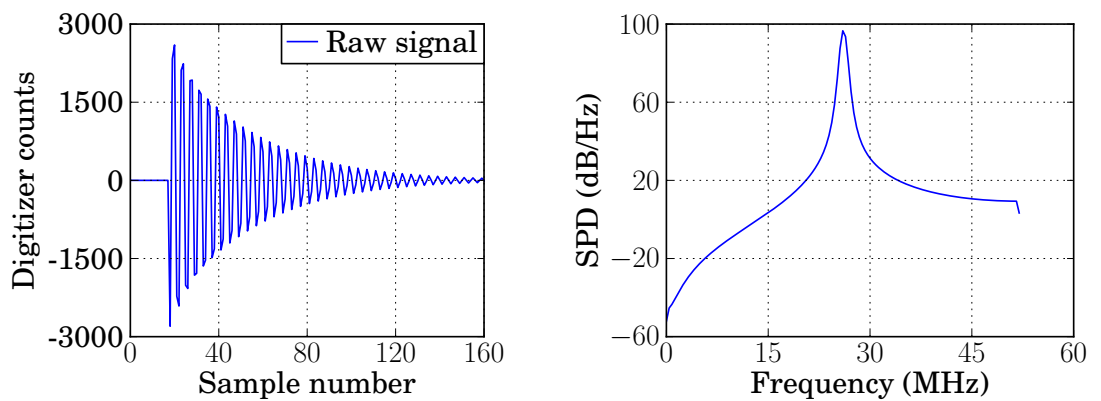
(b) Net gain at different input signal frequencies, showing a typical value of resonance frequency f_{110} of C-band CBPM

Figure 4.5: Linearity and bandwidth measurements of an electronic card to process CBPM signals

are digitised for further processing.

b) Digital signal processing

The second stage of frequency down conversion is performed digitally. Fig. 4.6(a) shows a simulated digitised CBPM signal, along with its spectral power density (SPD) in Fig. 4.6(b).



(a) Raw IF signal, digitiser samples connected by line to show signal shape.

(b) Spectral power density of raw signal with peak at approximate signal frequency.

Figure 4.6: Digitised raw IF signal in time and frequency domains.

The digitised IF signal is an oscillating signal with amplitude decaying in time, with a

time constant τ (Eqn. 2.6). The signal at a sample time t_s can be written as,

$$\begin{aligned} V(t_s) &= V_0 + \Theta(t_s - t_b) A_{peak} e^{\left(-\frac{t_s - t_b}{\tau}\right)} e^{i(\omega t_s + \phi)} + V_{noise}(t_s) \\ &= V_0 + A e^{i(\omega t_s + \phi)} + V_{noise}(t_s) \end{aligned} \quad (4.5)$$

where V_0 is the DC offset, t_b is the bunch arrival time, τ is the decay constant, ω is the angular frequency of the IF signal, A_{peak} is the initial peak amplitude given by Eqn. 2.18, A is the decayed signal amplitude at sample time t_s , Θ is zero before bunch arrival ($t_s < t_b$), and 1 after a bunch has arrived ($t_s > t_b$), and V_{noise} is the noise voltage.

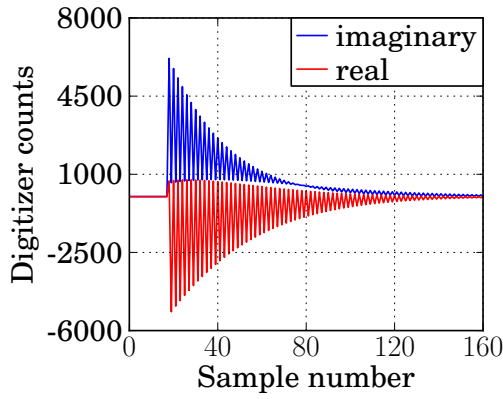
The DC offset (V_0) in the raw signal is calculated as an average of the voltage sampled before the bunch arrival time (t_b), which is subtracted from all data samples. The peak of SPD plot (Fig. 4.6(b)) tells an approximate frequency of the IF signal, which in this case is equal to 25.9 MHz. The signal is mixed with a complex oscillating signal of frequency equal to the SPD peak frequency ω_1 and unit amplitude. Neglecting the noise term and taking only the real part of Eqn. 4.5, the signal mixing process can be represented by following equation as,

$$A \cos(\omega t_s + \phi) \times e^{i(\omega_1 t_s)} = \frac{A}{2} \left[e^{i((\omega + \omega_1)t_s + \phi)} + e^{i((\omega - \omega_1)t_s + \phi)} \right], \quad (4.6)$$

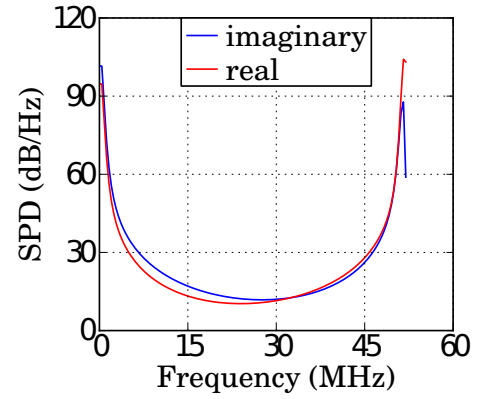
where ϕ is the phase of the IF signal with respect to the digital LO signal.

Fig. 4.7(a) shows the real and imaginary components of the mixed signal, while their SPDs are shown in Fig. 4.7(b). Each of the SPD plots shows two peaks, one near 0 and other near 52 MHz, which correspond to the two signal components with angular frequencies of $(\omega - \omega_1)$ and $(\omega + \omega_1)$ in Eqn. 4.6. The amplitude of the mixed signal is shown in Fig. 4.7(c), is the sum of the two frequency components. The signal component with frequency $(\omega + \omega_1)$ must be removed using a digital filter.

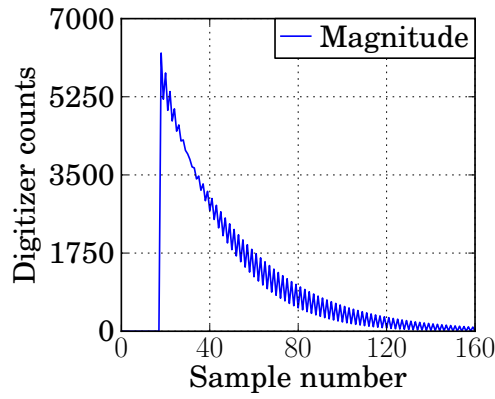
The digital filter is applied in the time domain. The output Y_j of a finite impulse response (FIR) filter at a sample j can be calculated from the input samples x_i as [50],



(a) Quadrature phase components of a mixed signal, real (in-phase) and imaginary (quadrature-phase)



(b) Power spectrum of a mixed signal, real and imaginary components



(c) Amplitude of a mixed signal with two components, one at 0 Hz and second at $2\omega_d$ angular frequency superimposed on it

Figure 4.7: Mixed signal in the time and frequency domains

$$Y_j = \frac{b_0 + \sum_{i=-\sigma}^{+\sigma} b_i x_i}{a_0} \quad (4.7)$$

where b_i are the convolution weight coefficients, a_0 and b_0 are constants, and σ defines the width of the convolution window in samples.

The convolution weight coefficients for a Gaussian filter are plotted in Fig. 4.8, which are calculated as,

$$a_0 = 3.011f_c,$$

and

$$b_i = 3.011 \left(\frac{f_c}{f_s} \right) \exp \left[-\pi \left(\frac{3.011 f_c}{f_s} f_i \right)^2 \right],$$

where f_i s traverse a range from $-\sigma$ to $+\sigma$ with $\sigma = \frac{1}{a_0 \sqrt{2\pi}}$, f_c is the cutoff frequency of the filter and f_s is the digitiser sampling frequency.

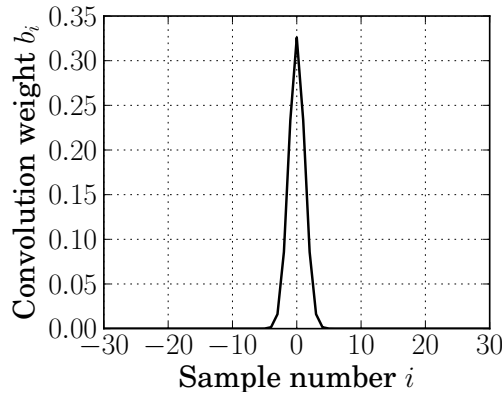


Figure 4.8: Convolution weights for a Gaussian filter with $f_c/f_s = 0.08$

Fig. 4.9(a) & 4.9(b) show the amplitude attenuation and phase delay characteristics of different digital filters; Butterworth, Chebyshev, Elliptic, and Gaussian, all with a same bandwidth of 4 MHz. The in built signal processing library in scientific python (SciPy) was used to generate the filter coefficients and their amplitude response and phase delay. As shown in Fig. 4.9(a), all filters attenuate the signal component at 2ω frequency by 160 dB. As shown in Fig. 4.9(b) the phase delay introduced by only the Gaussian filter varies linearly with the frequency. The phase delay introduced by a digital LPF does not change for a constant signal frequency, hence it does not affect the signal processing.

The amplitudes and phases of the signal processed using different digital filters are compared in Fig. 4.9(c) and 4.9(d) respectively. The Gaussian filter preserves the exponential shape of the signal and has a linear phase delay. In addition, the Gaussian filter has a finite impulse response (FIR), and the width of its convolution window can be limited explicitly. Because of these advantages, a Gaussian filter was used to process the CBPM signals.

Fig. 4.10(a) shows the in-quadrature phase components of the filtered signal, and their spectra are plotted in Fig. 4.10(b). In comparison to Fig. 4.7(b), the signal component

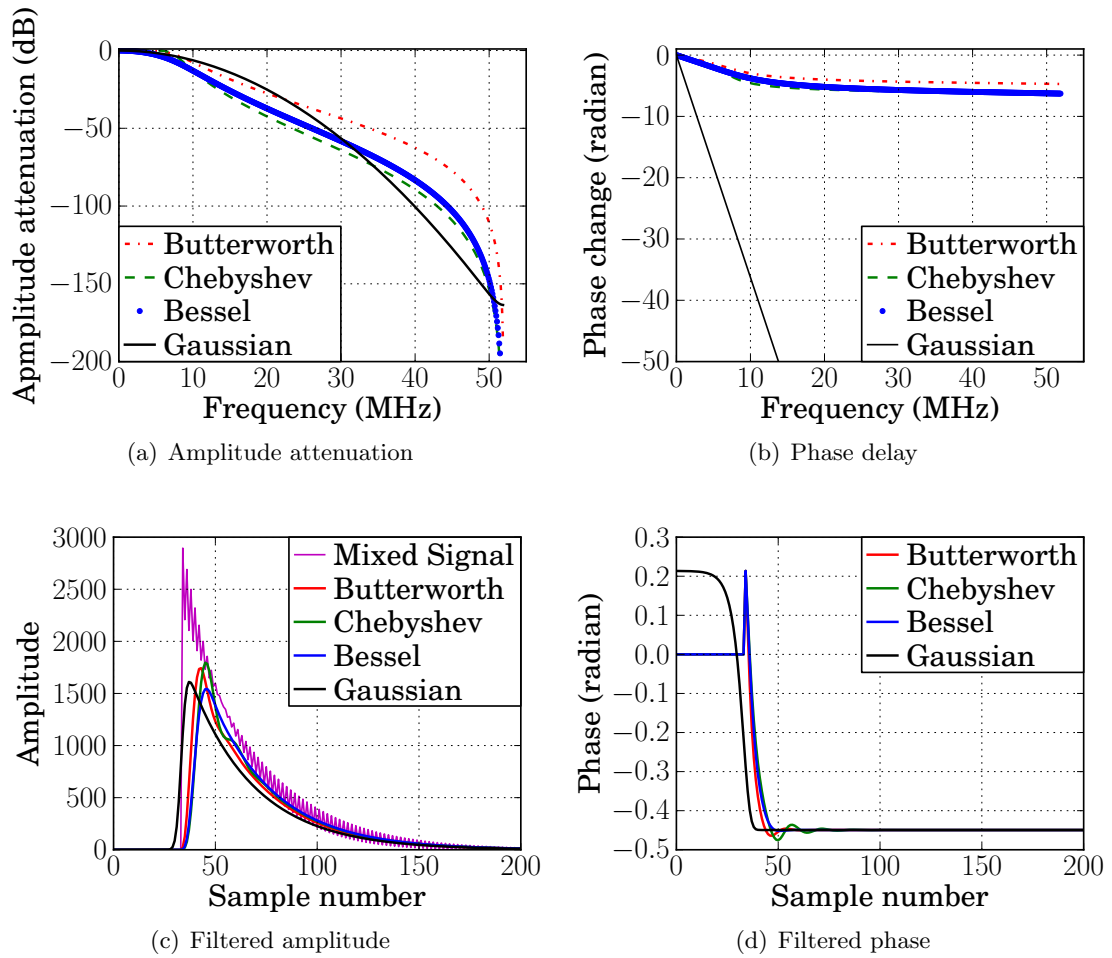
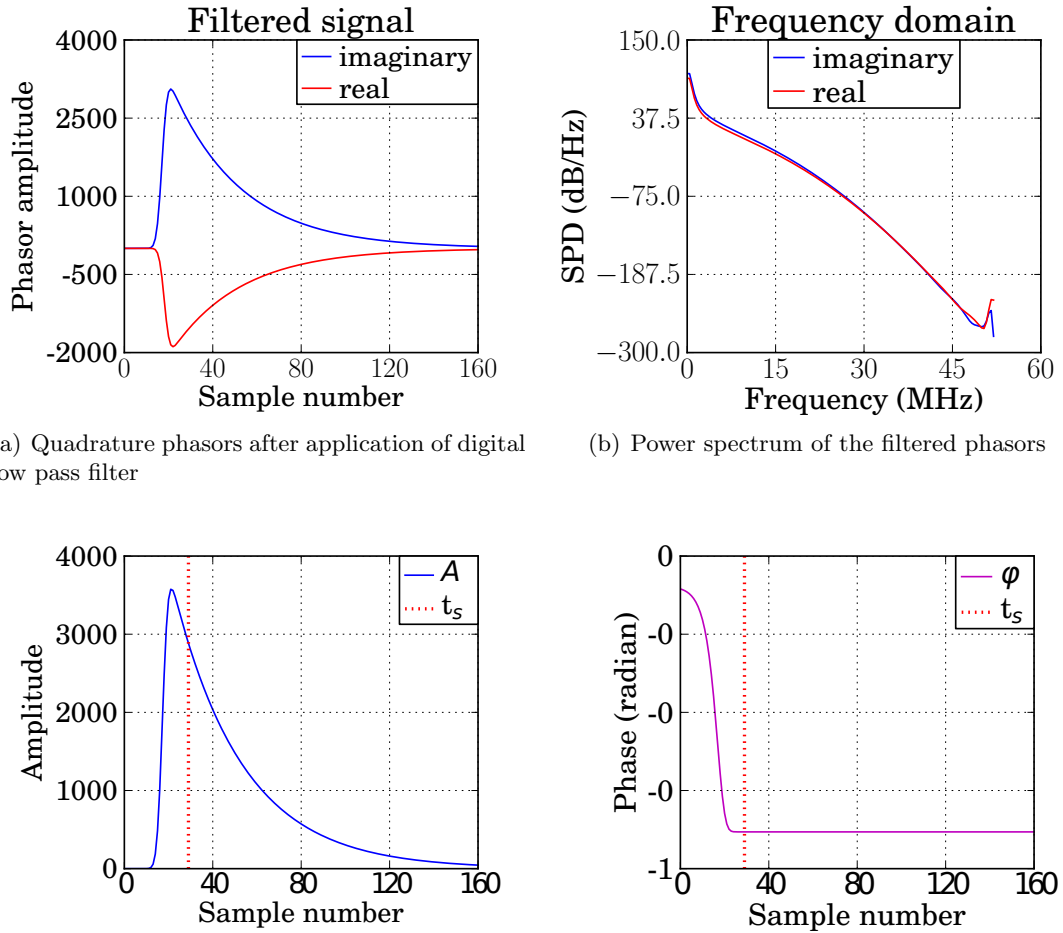


Figure 4.9: Filter characteristics comparison

with angular frequency $\omega + \omega_1$ is attenuated drastically. Accordingly, the SPD plot shows that the signal power at frequency $\omega + \omega_1$ is lower by more than 250 dB compared to the peak at frequency $\omega - \omega_1$.

Because of the limited frequency resolution of the SPD plot, the peak of the SPD is not the exact LO frequency to down-convert the IF signal to DC (0 MHz). An accurate LO frequency was determined by minimising the gradient of the phase of the down-converted signal. As shown in Fig. 4.11, if the frequency of the LO signal is not equal to the frequency of the IF signal, the phase of the filtered signal changes with time. The $\omega - \omega_1$ term in Eqn. 4.6 gives a linear change in phase $\Delta\phi$ over a change in sample



(a) Quadrature phasors after application of digital low pass filter

(b) Power spectrum of the filtered phasors

(c) Amplitude of the filtered signal, showing a sample t_s where I and Q are calculated.

(d) Phase of the filtered signal

Figure 4.10: Processed signal after application of the Gaussian digital LPF, showing a sample t_s where the I and Q phasors are calculated

time Δt_s , given by,

$$\frac{\Delta\phi}{\Delta t_s} = \omega - \omega_1 = 2\pi(f - f_{LO}). \quad (4.8)$$

This frequency difference is subtracted from the frequency of the SPD peak digital LO signal. If the digital LO frequency is equal to the IF signal frequency, then the phase remains constant (as plotted in Fig. 4.11) in time and has zero gradient. The phase gradient is calculated using only the samples with large signal amplitude. The

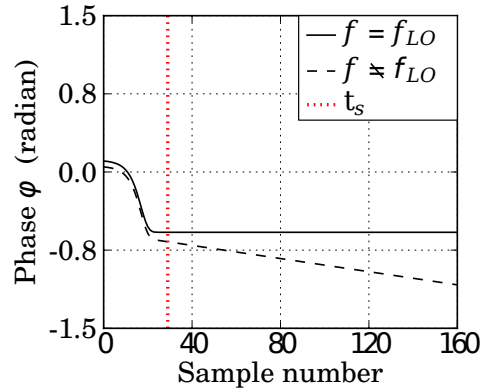


Figure 4.11: Phase of the down-converted IF signal as a function of sample number, for two different digital LO frequencies.

frequency is varied until the gradient is minimised. For $f = f_{LO}$, Eqn. 4.5 reduces to,

$$V(t_s) = A e^{\left(-\frac{t_s - t_b}{\tau}\right)} e^{i\phi}.$$

The amplitude and phase at an appropriate sampled time t_s is used to calculate the position. The time t_s is chosen such that it is delayed enough, after bunch arrival, to avoid the amplitude deformation due to the filters near the amplitude peak. This voltage can be represented in terms of the in i and quadrature q phase signals, compared to the LO signal, as,

$$\begin{aligned} i(t_s) &= A e^{\left(-\frac{t_s - t_b}{\tau}\right)} \cos(\phi) \\ q(t_s) &= A e^{\left(-\frac{t_s - t_b}{\tau}\right)} \sin(\phi). \end{aligned} \quad (4.9)$$

The same electronics system was used for the dipole and monopole signals from the position and reference cavities respectively. The digitised IF signals from both types of cavity were processed using the same digital signal processing (DSP) code to derive the amplitudes and phases. To remove the effect of the variation in the bunch charge, the processed amplitude of dipole signal A_d is normalised with the processed amplitude of the reference signal A_r . To correct the measurement for the variation in the bunch arrival time compared to the LO phase, the phase of the reference signal ϕ_r is subtracted

from the phase of the dipole signal ϕ_d . The amplitudes at any single sample (at any instance time) or a mean value of amplitudes at several consecutive samples (mean of amplitude over finite time) can be used for the calculation. From the processed amplitudes and phases, the in I and quadrature Q phasors are calculated as,

$$\begin{aligned} I(t_s) &= \frac{A_d(t_s)}{A_r(t_s)} \cos(\phi_d(t_s) - \phi_r(t_s)) \\ Q(t_s) &= \frac{A_d(t_s)}{A_r(t_s)} \sin(\phi_d(t_s) - \phi_r(t_s)). \end{aligned} \quad (4.10)$$

These I and Q phasors are used during the system calibration and position calculation.

c) Calibration

To convert the I and Q phasors into the actual beam position, it is essential to calibrate the CBPM system. During the calibration process the cavities are moved in x or y (perpendicular to beam propagation) directions using precision movers [26]. A cavity is usually moved in a range from -200 to +200 μm , with a step size of 100 μm . Scans over the range of -1000 μm to 1000 μm were also recorded several times. At each mover position, the cavity signals from several machine pulses were recorded. The signals (x or y position signals, depending on the direction of the mover scan) were processed using the electronic and digital processing methods described previously, resulting in I and Q phasors.

Fig. 4.12 shows the typical calibration plots from a single mover position scan, along the y -axis, of the CBPM labeled MQM11FF. The first row shows plots of I vs Q amplitudes, as well as of I and Q at different mover positions. Both I and Q phasors are correlated with the change in the mover position. The mean values of IQ are calculated at each mover position, which are plotted as red markers (*). The angle Θ_{IQ} is calculated by fitting a line through the mean values. The I and Q phasors are rotated by angle Θ_{IQ}

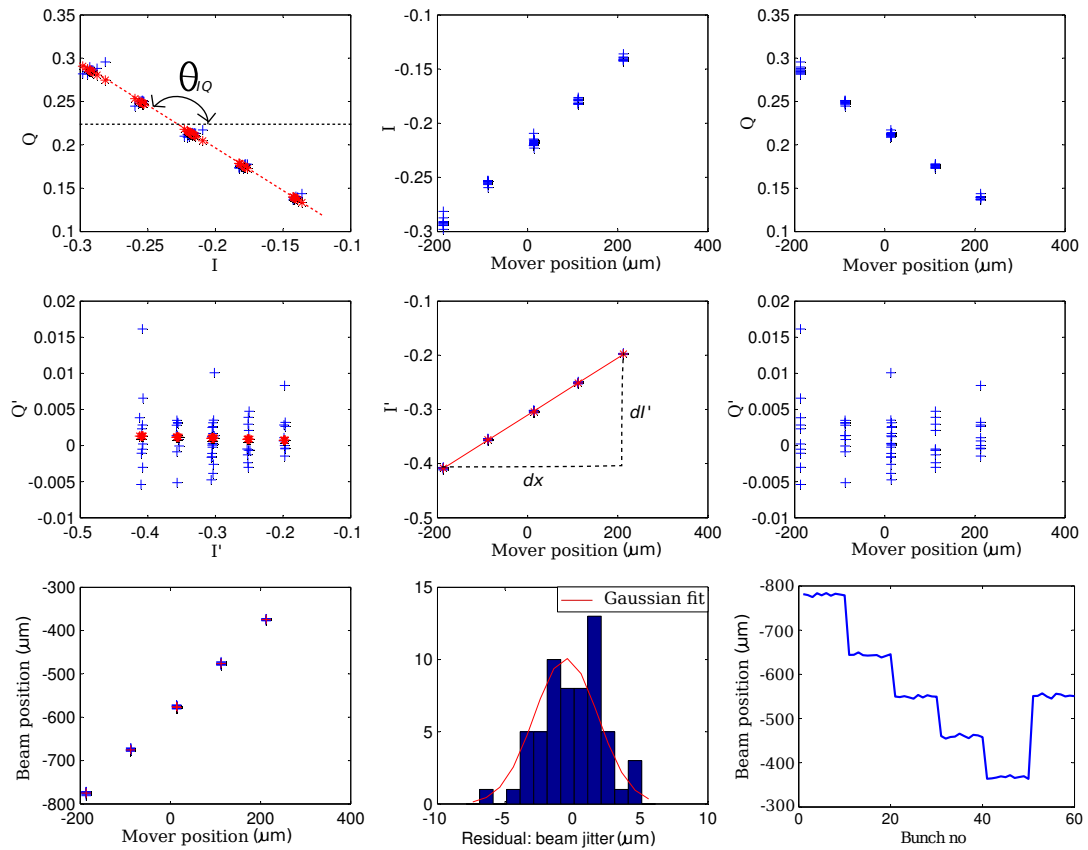


Figure 4.12: Calibration plots showing IQ diagram, phase rotation, position scale determination and residual histogram.

using a standard rotation matrix given by,

$$\begin{aligned}
 I' &= I \cos(\Theta_{IQ}) + Q \sin(\Theta_{IQ}) \\
 Q' &= -I \sin(\Theta_{IQ}) + Q \cos(\Theta_{IQ})
 \end{aligned}
 \tag{4.11}$$

The coordinates are rotated to make only I' phasors sensitive to the mover position. It is not mandatory to choose only I' signal to represent the position. The coordinate rotation process can be seen as changing the phase of the digital LO signal such that the phase of I' matches the phase of the signal induced due to a bunch position offset.

The second row (in Fig 4.12) shows the same plots for the rotated phasors I' and Q' . The first plot shows that the I' is no longer correlated to Q' . The second and third plots show that I' changes linearly with the mover position, while Q' does not depend

on the mover position. The position scale factor S is calculated from the slope of I' against mover position, so,

$$\frac{1}{S} = \frac{dI'}{dx}, \quad (4.12)$$

where x is the mover position.

The beam position is determined by multiplying the phasor I' with the scale factor S . The left plot in the third row shows the measured beam positions as a function of the mover positions. At each mover position, the position residuals are calculated, and histogram is plotted to calculate the measurement error. A Gaussian is fitted to the residuals histogram, whose width is the convolution of the error in the position measurement and beam position jitter. A position jitter of more than $2 \mu\text{m}$ is observed compared to the expected resolution of the order of 200 nm. The measurement error is mainly dominated by beam jitter. The other sources of errors are non-linearities and noise in the processing electronics, along with the digitiser clock errors. Beam jitter can be reduced by using correlation techniques such as singular value decomposition (SVD), which is discussed later in this chapter.

4.2.2 Effect of temperature change on CBPM frequency

The effects of temperature change on a CBPM were studied using surface temperature monitor probes attached to the cavities. Most of the CBPMs are fixed to the quadrupole and sextupole magnets. When the magnets are turned on during beam start up, their temperature rises until reaching equilibrium. The heat from the magnets are transferred to the attached cavities and increase their temperature.

The metal of the cavity expands with an increase in the temperature and changes the cavity geometry. With a rise in the temperature, the cavity should expand and the resonant frequency of the dipole mode should decrease. One of the S-band CBPMs, labeled MQM1FF with the dipole frequency of 2.8 GHz, was monitored for the effect of temperature change. This cavity was chosen because it was the only cavity with a sizable temperature variation. At regular time intervals the temperature and variation in the dipole frequency was monitored. The change in the dipole frequency was de-

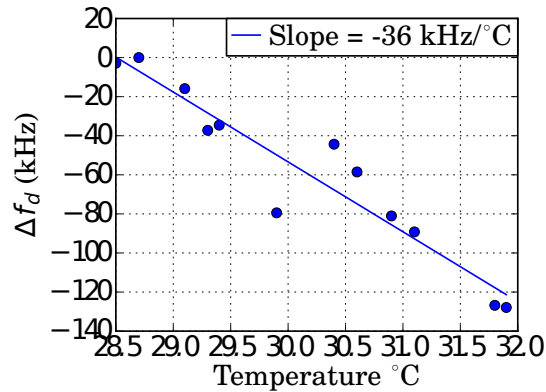


Figure 4.13: Change in the resonance frequency of a CBPM as a function of temperature.

terminated from the variation in the IF frequency, determined using the phase gradient minimisation process discussed in section 4.2.1. The change in dipole frequency Δf_d with temperature is plotted in Fig. 4.13. During the experiment, the temperature of the cavity increased from 28.5 to 32 °C and the CBPM frequency decreased by 125 kHz, giving a temperature dependence of $-36 \text{ kHz}/^\circ\text{C}$.

4.3 Signal simulation and calibration code

To understand and verify the signal processing and system calibration methods, a code was developed to simulate and process CBPM signals. Fig. 4.14 shows the block diagram of the program structure. The code was written in python [51], and it was divided into classes depending on their functions. To simulate the cavity signals, the code first loads a set of bunch train parameters and BPM parameters.

The parameters can be given as user input or through a configuration file. Depending on the user input, the program generates a bunch train and sets the signal processing parameters. To simulate the cavity signal from multiple bunches, the individual signal from each bunch is calculated and then they are added to produce the net signal. The user can generate signals with a specific amount of beam position and angle jitter. The simulated signal was added with user specified thermal noise. The signal was then

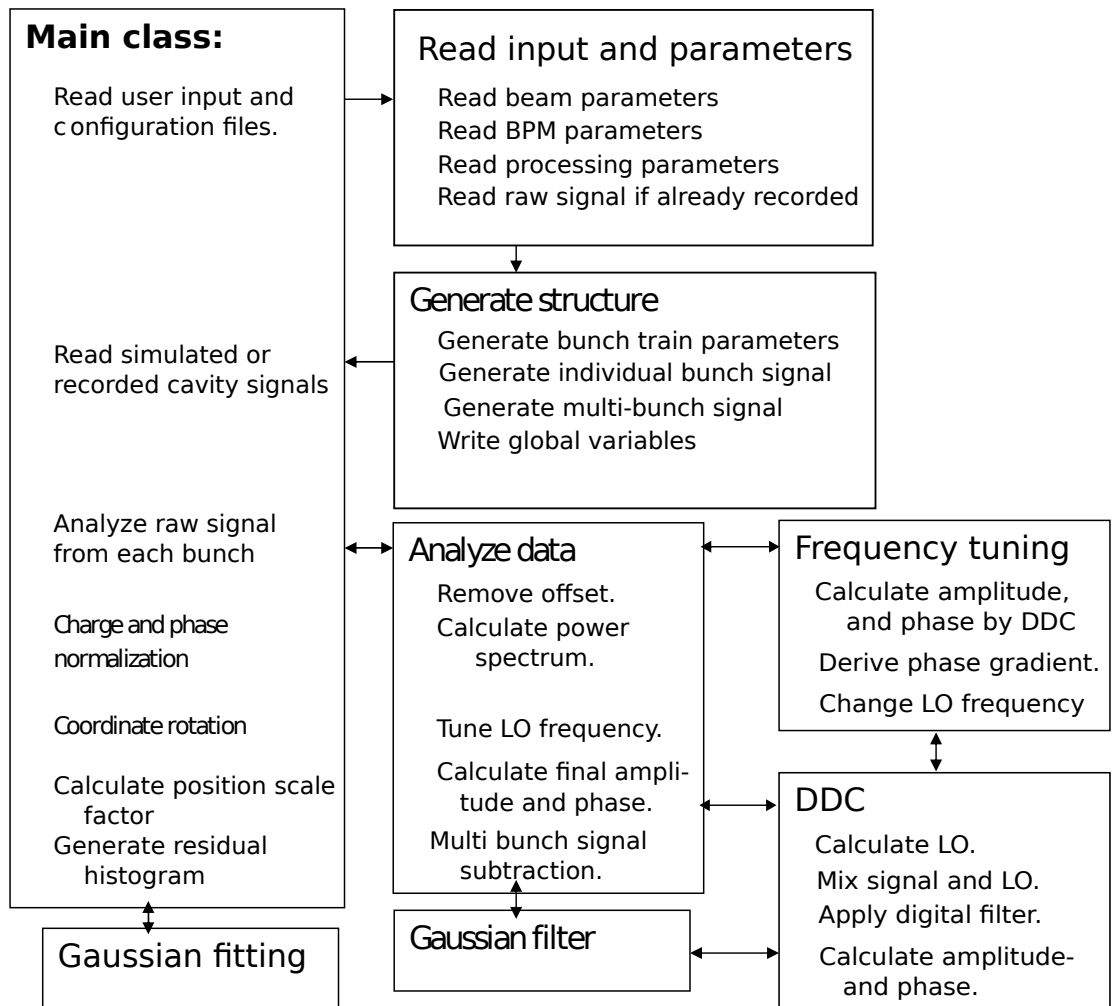


Figure 4.14: Layout of the simulation and analysis code.

passed to the class for DSP.

The simulated signals are processed using the same processing codes used to process the experimental data. As mentioned in Section 4.2.1, the amplitude and phase of the signal are calculated using digital down-conversion and filtering. After frequency tuning of the digital LO signal, the final amplitude and phases are used to calculate I and Q phasors. In the case of a signal from multiple bunches, the signal pollution from previous bunches was removed using a signal subtraction algorithm. As with

single bunch operation, the rotated I and Q phasors were used to determine the beam position. Because the input parameters, such as signal and noise amplitudes, are well controlled for simulated signals, the performance of the code can be verified against any discrepancies observed in the experimental data. Along with the experimental results, the signal processing and results obtained using the simulated data are also discussed in the following sections.

4.4 CBPM signal from multiple bunches and signal subtraction

After a bunch has passed through a cavity, the induced field continues oscillating with its amplitude decaying exponentially in time. Similar to Eqn. 4.5, the digitised IF signal for one bunch $V_1(t_s)$, now with labels on the parameters for the bunch number as,

$$\begin{aligned} V_1(t_s) &= A_{\text{peak},1} \Theta_1(t_s - t_{b,1}) e^{\left(-\frac{t_s - t_{b,1}}{\tau}\right)} e^{i(\omega t_s + \phi_1)} \\ &= A_1 e^{i(\omega t_s + \phi_1)} \end{aligned} \quad (4.13)$$

where,

$$A_1 = A_{\text{peak},1} \Theta_1(t_s - t_{b,1}) e^{\left(-\frac{t_s - t_{b,1}}{\tau}\right)}, \quad (4.14)$$

where the variables used in the above equation and following equations in this chapter are defined in Table 4.3.

For two bunches, the fields induced inside the cavity add linearly and result in an IF voltage $V_2(t_s)$ given by,

$$V_2(t_s) = A_1 e^{\left(-\frac{\Delta t_b}{\tau}\right)} e^{i(\omega t_s + \phi_1)} + A_2 e^{i(\omega t_s + \phi_1 - \omega \Delta t_b)}. \quad (4.15)$$

The individual signals simulated for each bunch are shown in Fig. 4.15(a). Upon arrival of the second bunch, the amplitude of the signal from the first bunch has decayed, but only up to 50% of its initial (peak) value. The signal from the second bunch is polluted

Table 4.3: Definitions of mathematical variables used for multi-bunch signals.

Symbol	Name	Meaning
$A_{\text{peak},j}$	Peak amplitude	Initial (peak) amplitude of the IF signal, induced by j^{th} bunch
A_j	Amplitude	Amplitude of the IF signal at time t_s , induced by only j^{th} bunch
ϕ_j	Phase	Phase of the IF signal with respect to digital LO, induced by only j^{th} bunch
$t_{b,j}$	Bunch arrival time	Arrival time of the j^{th} bunch
Δt_b	$t_{b,j} - t_{b,j-1}$	Time separation between consecutive bunches
t_s	Time sample	Sample time during a bunch, at which the position is calculated
ω	Angular frequency	Angular frequency of the IF signal from a cavity
τ	Decay constant	Decay constant of the IF signal from a cavity
B_j	Net amplitude	Net amplitude of the total IF signal at a time t_s , after j number of bunches have passed
θ_j	Net phase	Net phase of the total IF signal with respect to digital LO, induced after j number of bunches have passed through a cavity

considerably by the signal from the first bunch. The simulated net signal from the two bunches, which would be recorded by a digitiser, is shown in Fig. 4.15(b).

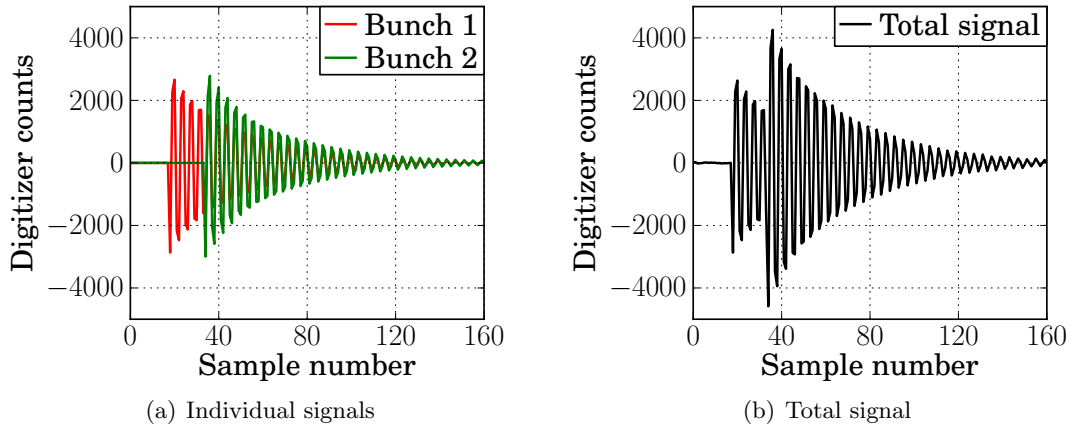


Figure 4.15: Simulated digitised IF signals from two bunches separated by 187.6 ns

In a similar way, the signal induced after the passage of n bunches can be written as,

$$\begin{aligned} V_n(t_s) &= \sum_{k=1}^n A_k e^{\left(-\frac{(n-k)\Delta t_b}{\tau}\right)} e^{i(\omega t_s + \phi_1 - (k-1)\omega\Delta t_b)} \\ &= B_n e^{i(\omega t_s + \theta_n)}, \end{aligned} \quad (4.16)$$

where,

$$A_k = A_{\text{peak},k} \Theta_1(t_s - t_{b,k}) e^{\left(-\frac{t_s - t_{b,k}}{\tau}\right)}. \quad (4.17)$$

Using above formula, the CBPM signals from a bunch train made of many bunches with different parameters can be simulated. As in the case of single bunch signal, the net amplitude B_n and net phase θ_n of the total signal from multiple bunches are also calculated by the process of digital frequency down conversion, by mixing it with a digital LO signal and filtering. Neglecting any attenuation and phase delay in the digital filter, the equation for the down converted signal for n bunches $V_{DDC,n}$ can be written from the above equation as,

$$\begin{aligned} V_{DDC,n}(t_s) &= \sum_{k=1}^n A_k e^{\left(-\frac{(n-k)\Delta t_b}{\tau}\right)} e^{i(\phi_1 - (k-1)\omega\Delta t_b)} \\ &= B_n e^{i(\theta_n)}. \end{aligned} \quad (4.18)$$

The above equation shows that the signal from the n^{th} bunch will be polluted by signals induced by the previous bunches. The method developed to remove this signal pollution uses a signal subtraction algorithm. The algorithm removes the signal pollution by subtracting the phasors sampled during the immediate preceding bunch, with appropriate amplitude decay and phase rotation applied to it. The process can be mathematically expressed by rearranging Eqn. 4.16 as,

$$\begin{aligned} V_{DDC,n}(t_s) &= A_n e^{i(\phi_1 - (n-1)\omega\Delta t_b)}, \\ &+ e^{\left(-\frac{\Delta t_b}{\tau}\right)} \sum_{k=1}^{n-1} A_k e^{\left(-\frac{(n-1-k)\Delta t_b}{\tau}\right)} e^{i(\phi_1 - (k-1)\omega\Delta t_b)} \\ &= A_n e^{i(\phi_1 - (n-1)\omega\Delta t_b)} + e^{\left(-\frac{\Delta t_b}{\tau}\right)} B_{n-1} e^{i(\theta_{n-1})}. \end{aligned} \quad (4.19)$$

By rearranging the terms in the above equation, an equation for the subtracted signal from a cavity can be written as

$$A_n e^{i(\phi_1 - (n-1)\omega\Delta t_b)} = B_n e^{i(\theta_n)} - e^{\left(-\frac{\Delta t_b}{\tau}\right)} B_{n-1} e^{i(\theta_{n-1})}. \quad (4.20)$$

The equation shows that the signal pollution from all previous bunches can be removed by subtracting the signal phasors sampled during only the immediate previous bunch, with an appropriate amplitude decay. The pollution in the dipole signals from a position cavity and monopole signal from a reference cavity is removed using the same signal subtraction algorithm.

As for single bunch signals (Eqn 4.10), the I and Q phasors can be calculated for the individual bunches using the subtracted amplitudes and phases of the dipole and reference cavities, so

$$\begin{aligned} I_n(t_s) &= \frac{A_{n,d}}{A_{n,r}} \cos[\phi_{1,d} - \phi_{1,r} - (n-1)\Delta t_b(\omega_d - \omega_r)], \\ Q_n(t_s) &= \frac{A_{n,d}}{A_{n,r}} \sin[\phi_{1,d} - \phi_{1,r} - (n-1)\Delta t_b(\omega_d - \omega_r)], \end{aligned} \quad (4.21)$$

where the symbols are described in Table 4.3, and carry an additional subscript of d for dipole and r for reference cavities.

In comparison to Eqn 4.10, the above equation has an additional phase term. It shows that if the resonant frequencies of the dipole and reference cavities are not equal, there will be a phase difference $\Delta\phi_{IQ}$ between the I and Q phasors of the consecutive bunches, which can be calculated as,

$$\Delta\Theta_{IQ} = \Delta\omega \times \Delta t_b = (\omega_d - \omega_r) \Delta t_b. \quad (4.22)$$

With these predictions, the signal subtraction algorithm was tested on the signals induced by multiple bunches in the CBPMs on the ATF2.

4.4.1 Application of the algorithm on two bunch signals

To test the performance of the signal subtraction algorithm on the CBPM signals induced by multiple bunches, signals were recorded from the CBPMs installed on ATF2, while the ATF2 was operated in a multi-train mode (Section 4.1.1). Most of the data was recorded parasitically during machine operations for the study of Feedback on Nano-second Timescales (FONT) system. Also during a dedicated time slot of few hours in the period between November - December, 2011. Several cavities were calibrated using precision movers, with a focus on a triplet of cavities labeled MQM13FF, MQM12FF and MQM11FF, located in the low dispersion region. The monopole cavity labeled as REFC1 was used as a reference cavity. The frequencies and decay times of these cavities are listed in Table 4.4.

Table 4.4: Frequency and decay time of the cavity triplet used for the studies of the CBPM signals from multiple bunches.

CBPM	Resonance frequency $\omega/2\pi$ (GHz)	Decay constant τ_d (ns)
MQM13FF	6425.8	316
MQM12FF	6426.2	285
MQM11FF	6426.0	305
REFC1	6424.6	292

The same electronics and digitiser systems, which were used to process the single bunch signals, were also used to process the signals from multiple bunches. The GHz frequency cavity signals were down converted to a MHz frequency IF signals, which were then digitised. By digitally processing the digitised signal in a similar way to the single bunch signals, the amplitude and phase (B_n and θ_n in Eqn. 4.18) were calculated for the dipole and reference signals. The amplitude and phase from a y -position signal induced in MQM13FF by a machine pulse of two bunches, are plotted in Fig. 4.16. Each bunch carried 1.6 nC charge, and were separated by 186.7 ns.

During the process of DDC, a digital Gaussian low pass filter was used to remove the high frequency components. As described in Section 4.2.1*b*), the DDC requires a Gaussian low pass filter to remove the 2ω components. The width of the convolution window increases with reduction in the cutoff frequency. The maximum width of the

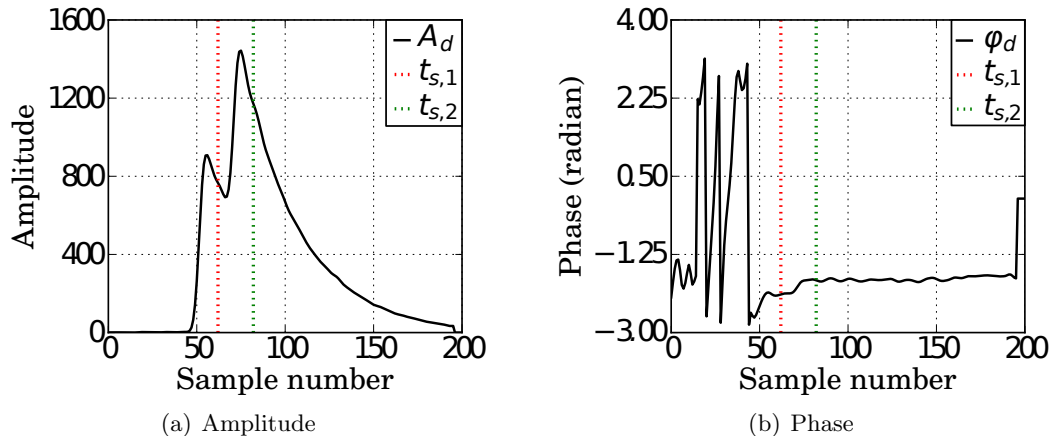


Figure 4.16: Processed amplitude and phase, with sample location for position determination for each bunch.

window is limited by the number of sample points available between consecutive bunch arrivals. A 14 sample wide Gaussian filter of cutoff frequency of 14.6 MHz was used in the DDC filter. The processed amplitude and phase were sampled during each bunch, at the time samples $t_{s,1}$ and $t_{s,2}$. The sample point was chosen between two bunch arrivals, as seen in Fig. 4.16.

To calculate the position scale factor (S) and rotation angle (Θ_{IQ}), the CBPM MQM13FF was calibrated in a similar way to the single bunch calibration. The mover position was scanned along the y -axis from -200 to 200 μm in steps of 100 μm . The CBPM signals from around 20 machine pulses were recorded at each mover position.

From the downconverted amplitude and phase at the specific samples during each bunch, the I and Q phasors were calculated. The I and Q phasors calculated without applying the signal subtraction algorithm, using the net amplitudes B_n (in Eqn. 4.18) and phases θ_n , are plotted in Fig. 4.17(a). In all following plots in this chapter, the color coding of red for Bunch-1, green for Bunch-2 and blue for Bunch-3 is used to plot the data from different bunches, unless specified.

The first bunch is unpolluted by previous bunches so the same algorithm of θ_{IQ} and S determination was used as in single bunch operation, described in Section 4.2.1c). The IQ phasors varied along a line at a specific angle Θ_{IQ} with the I -axis. The angle Θ_{IQ} is the IQ rotation angle required to calculate the bunch position. To compare the

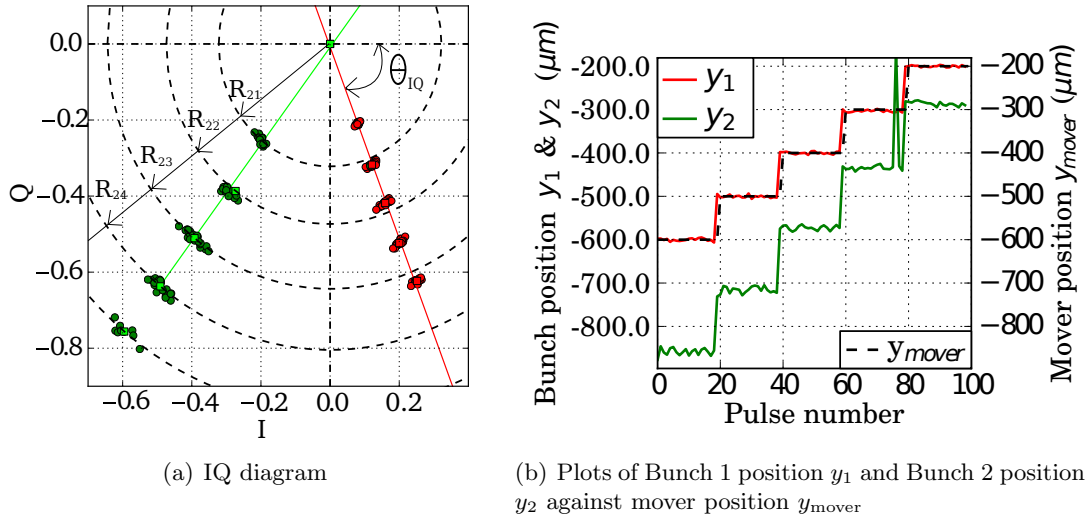


Figure 4.17: Calibration of MQM13FF in a multi-train mode without signal subtraction.

IQ plots from the first and second bunches, concentric circles are plotted with their centers at the origin and radii R_{jk} (for bunch j mover position k) equal to the mean magnitudes of the phasors at each mover position. The change in the radius R_{jk} of the circle with the change in the mover position gives the position scale factor (S).

As seen from Fig. 4.17(a), the amplitudes of the IQ vectors from the second bunch are approximately 43% higher than the amplitudes from the first bunch. For a given change in the mover position, the change in the signal amplitude for the second bunch is not equal to the change for the first bunch. As both of the bunches are extracted during a single extraction pulse, the second bunch is expected to arrive at the same position of the first bunch. Even if the second bunch arrives at a different position offset, the change in the phasor amplitudes from the two bunches for a mover position change should always be equal because of its linear dependence on the position offset. Clearly without subtraction, each bunch would require separate scale factors. It would require a calibration for each bunch and it also depends on the signals from previous bunches. The difference in rotation angle Θ_{IQ} for the two bunches can be because of the difference in the resonant frequencies of the dipole and reference cavities.

The phasors were rotated by the respective angle Θ_{IQ} for each bunch using Eqn. 4.11. The position was calculated by multiplying the rotated phasors I' (in Eqn. 4.12) with

the scale factor S for the first bunch. The measured positions of both bunches as a function of mover position are plotted in Fig. 4.17(b). The bunch positions y_1 and y_2 of the first and second bunches follow the change in the mover position y_{mover} , but the absolute values and amount of change in the position of the second bunch were higher than those of the first bunch. The position of the second bunch was overestimated by more than 43%, which was a large systematic offset.

To remove the signal pollution from the previous bunches, the signal subtraction algorithm was applied on the CBPM signals. The subtracted amplitude A_2 and phase ϕ_2 for the second bunch were calculated using Eqn. 4.20. The subtracted phasors from the reference cavity were also calculated using the same algorithm. The I and Q values were calculated from the subtracted amplitudes and phases using Eqn. 4.10, and are plotted in Fig. 4.18(a).

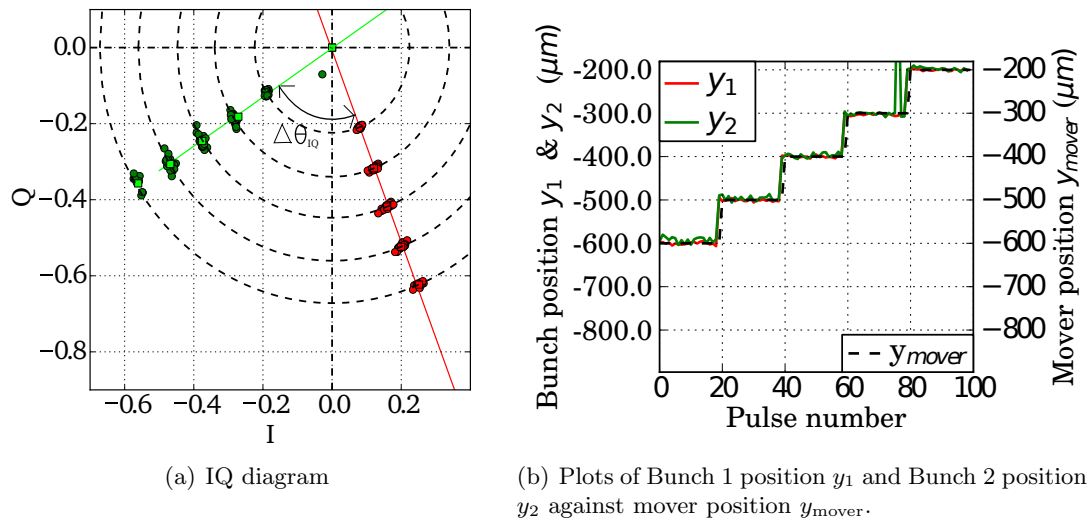


Figure 4.18: CBPM system calibration in a multi-train mode with signal subtraction.

As expected, the magnitude of the phasors of the first and second bunches were now similar and fall on same concentric circles. The change in the magnitude for both bunches, for a cavity position change, are now equal. To calculate the bunch position, the phasors were rotated by their respective angles Θ_{IQ} using Eqn. 4.11. The positions calculated, by multiplying the rotated phasors with the scale factor S from the first bunch, are plotted in Fig. 4.18(b). The average beam positions of both bunches calculated at different mover positions, are listed in Table 4.5.

The scale factor calculated from the first bunch was used to calculate the positions of both bunches. When calculated without signal subtraction, the position offset of the second bunches at each mover position were larger than that of the first bunches. At larger offset of 600 μm , the error in second bunch position increased to 260 μm . This systematic error, of 43%, in the second bunch position was due to the signal pollution from the first bunch. After application of the signal subtraction algorithm, the difference in position reduced to less than 2%. The results prove that the signal subtraction algorithm removes the signal pollution effectively and the method works.

Table 4.5: Systematic error in bunch position measurement due to signal pollution, and removal of signal pollution using signal subtraction algorithm

Mover Position y_{mover} (μm)	Bunch 1	Bunch 2			
	Average position y_1 (μm)	Without signal subtraction		After signal subtraction	
		position y_2 (μm)	$ y_2 - y_1 $ (μm)	position y_2 (μm)	$ y_2 - y_1 $ (μm)
-200	-200.1	-286.1	86.0	-197.4	2.7
-300	-303.1	-434.4	131.3	-301.0	2.1
-400	-399.8	-572.7	172.9	-397.7	2.1
-500	-500.5	-716.3	215.8	-496.9	3.6
-600	-600.0	-858.5	258.5	-591.9	8.1

a) Dependence of IQ rotation angle on dipole and reference frequencies

As explained in Section 4.2.1, before multiplying with the position factor, the I and Q phasors are rotated by the angle Θ_{IQ} using Eqn. 4.11. As shown in Fig. 4.18 the rotation angle for the second bunch is different from that for the first bunch. The scale factors S for the first and second bunches become equal after signal subtraction. Because Θ_{IQ} for the two bunches are different, the calibration constants determined from the single bunch calibration can not be used to calculate the position of the second bunch. If the phase jump can be estimated, then it can be removed. The phase of a signal with angular frequency ω would advance by $\Delta\phi$ over a time span of Δt_b as,

$$\Delta\phi = \omega \times \Delta t_b. \quad (4.23)$$

The processed phases of the signals with different frequencies, from a dipole (MQM13FF) and reference (REFC1) cavities, are shown in Fig. 4.19. As shown in Eqn. 4.22, if the frequencies of the dipole and reference cavities are different, then there will be a phase difference $\Delta\Theta_{IQ}$ between the IQ rotation angles Θ_{IQ} for consecutive bunches.

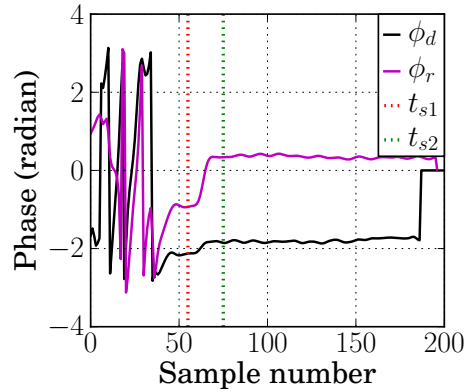


Figure 4.19: Processed phases of the IF signals from cavities MQM13FF and REFC1, induced by two bunches.

To confirm the hypothesis, bunch separation Δt_b was changed and the MQM13FF was calibrated to calculate the phase difference $\Delta\Theta_{IQ}$ for the two bunch separations. The dipole (MQM13FF) and reference (REFC1) cavities have their frequencies separated by 1.1764 MHz. The IQ plots from the signal subtracted phasors for the two bunch separations are shown in Fig. 4.20. It is clear from the plots that $\Delta\Theta_{IQ}$ changes with the bunch separation.

The measured phase difference for the different bunch separations are compared to their predicted values in Table 4.6. The phase difference agreed well with the predicted values, which proves that it is due to the difference in resonant frequencies of the dipole and reference cavities.

Table 4.6: IQ rotation angle difference $\Delta\Theta_{IQ}$ between the first and second bunch phasors, for different bunch separations Δt_b .

Bunch Separation Δt_b (ns)	Phase difference $\Delta\Theta_{IQ}$ (radian)	
	Theoretical	Experimental
186.7	1.38	1.36
285.6	2.05	2.09

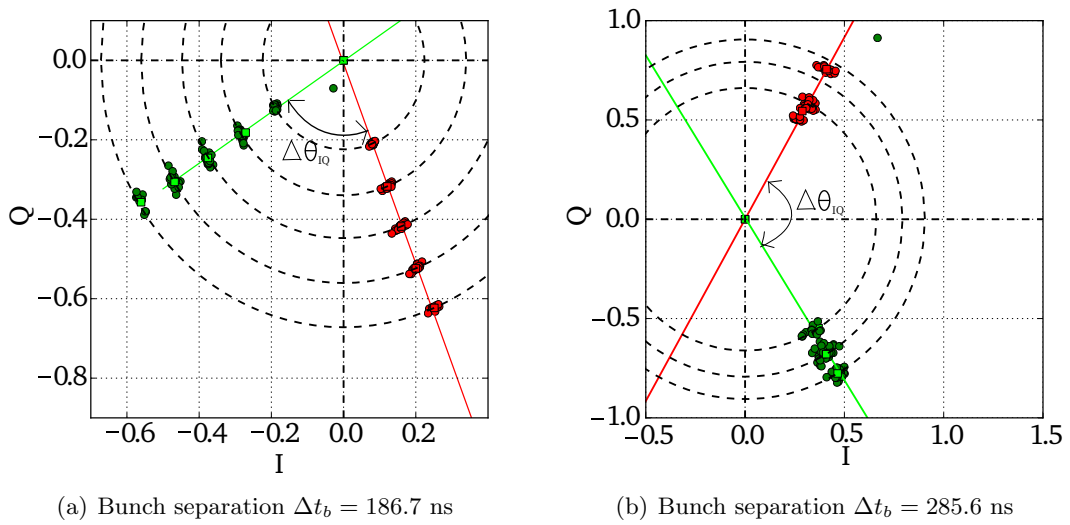


Figure 4.20: IQ plots of subtracted phasors from calibrations of MQM13FF along the y -axis, for two different bunch separations Δt_b .

The frequency difference can be measured by RF testing of the cavities and also from the digitised IF signals. For a known frequency difference and bunch separation, the expected phase jump can be predicted and removed during the calculation of I and Q phasors as shown in Eqn 4.21. Now as the reason for the phase difference is established and the position scales for both of bunches are equal, the calibration coefficients determined from a single bunch calibration can be used to derive the positions of any bunch with a known bunch separation.

b) Second bunch with different position offset

It was convenient to interpret the two bunch calibration data with the second bunch arriving at the same position offsets as the first bunch. If the second bunch is kicked by a different amount by the extraction kicker, which is possible when it falls near the edge of the kicker pulse, it may arrive at the CBPM at a different horizontal position offset. The IQ diagram for a calibration of MQM11FF in the x -axis is shown in the Fig. 4.22. The cavity was moved over a range of -200 to 200 μm around its nominal position, with a step size of 100 μm .

As shown in Fig. 4.21, the amplitude of the IQ phasors, calculated without signal

subtraction, from the second bunch do not agree with that of the first bunch. The difference in phasor magnitudes for consecutive mover positions are compared in Table 4.7. When the signal subtraction was not applied to the second bunch phasors, the position scale factor for the first bunch was approximately 50 % higher than that for the second bunch.

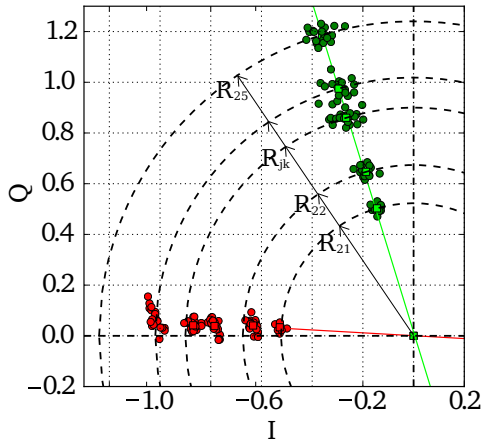


Figure 4.21: IQ diagram from a calibration run of MQM11FF, without signal subtraction.

The IQ diagrams after signal subtraction are shown in Fig. 4.22(a) & Fig. 4.22(b). Even after the signal subtraction is applied, the second bunch has different position offsets compared to the first bunch. Even if the second bunch has different horizontal position offset, for a change in the mover position, the change in the amplitude of the IQ phasors for the first and second bunches should be equal.

Table 4.7: Comparison of the change in the amplitude of position signal for second bunch, with and without signal subtraction

ΔR_{jk}	Bunch-1 ($j = 1$)	Bunch-2 ($j = 2$)	
		Without subtraction	With subtraction
$R_{j2} - R_{j1}$	0.1053	0.1506	0.1050
$R_{j3} - R_{j2}$	0.1519	0.2265	0.1541
$R_{j4} - R_{j3}$	0.0842	0.1185	0.0834
$R_{j5} - R_{j4}$	0.1509	0.2217	0.1566

After signal subtraction, for each mover position change, the change in the amplitudes of the IQ phasors for the second bunch agreed well with that for the first bunch, even though their absolute values were different. The difference of more than 50 % in

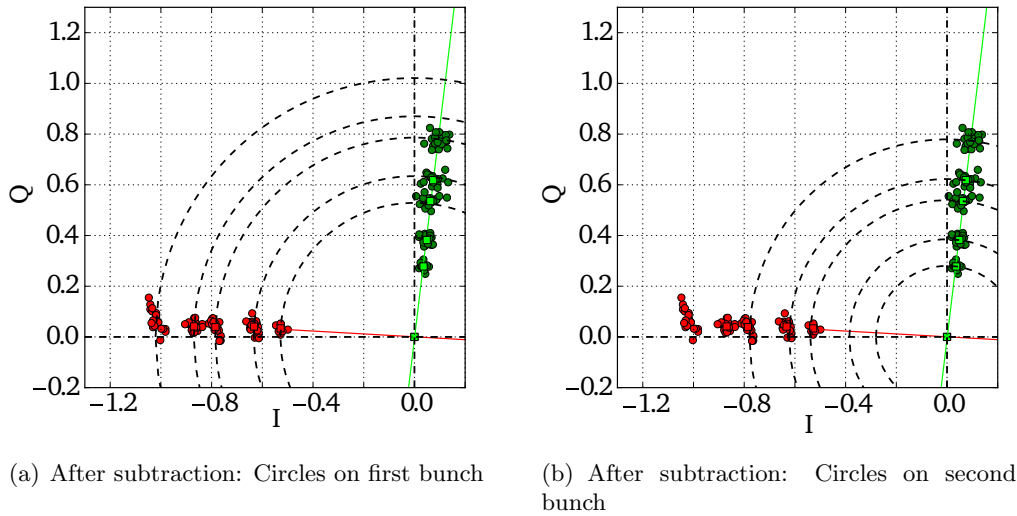


Figure 4.22: IQ diagrams from a calibration run of CBPM MQM11FF, with signal subtraction, showing second bunches arriving at different position to the first bunch

the position scale reduced to less than 3.5 % after signal subtraction. Comparison of position scale shows the effectiveness of the signal subtraction method irrespective of the absolute bunch position values.

c) Beam jitter and SVD based jitter subtraction

To derive the resolution of CBPM MQM12FF in multi-bunch mode, sets of CBPM signals from 100 machine pulses were recorded from the triplet of CBPMs. Bunch positions were calculated using the signal subtraction, IQ rotation and position scale factor S . The position measurement variation is normally dominated by the actual variation in the beam position, which is typically two to three orders larger than the system single bunch resolution. Once the beam position jitter is removed, the resolution should be limited by the variation in the system gain, amplitude noise and phase noises in the system.

For a fixed beam-line-optics, the positions recorded by different CBPMs at different locations along the beam line should be correlated to a certain degree. Using correlation techniques, beam position at the location of the cavity under test can be predicted using other BPMs, which can be used to remove the beam position jitter. The beam position

was predicted using a model independent analysis (MIA) technique [52]. A set of coefficients c_j can be determined, which linearly relate the position r_{ki} of an i^{th} bunch recorded by the k^{th} CBPM to the positions r_{ji} of the same bunch recorded by other CBPMs, given by,

$$r_{ki} = \sum_{j=1, j \neq k}^M r_{ji} \cdot c_j, \quad (4.24)$$

where M is the total number spectator cavities. Alternatively I' or I and Q could be used instead of positions.

To find the coefficients, a matrix is formed from the positions recorded from N machine pulse given by,

$$\begin{pmatrix} r_{k1} \\ r_{k2} \\ \vdots \\ r_{kN} \end{pmatrix} = \begin{pmatrix} r_{11} & r_{21} & \cdots & r_{j \neq k 1} & \cdots & r_{M1} \\ r_{12} & r_{22} & \cdots & r_{j \neq k 2} & \cdots & r_{M2} \\ \vdots & \vdots & \ddots & \vdots & \ddots & \vdots \\ r_{1N} & r_{2N} & \cdots & r_{j \neq k N} & \cdots & r_{MN} \end{pmatrix} \cdot \begin{pmatrix} c_1 \\ c_2 \\ \vdots \\ c_M \end{pmatrix}. \quad (4.25)$$

The equation can be written in matrix notation as

$$\mathbf{R}_k = \mathbf{R} \cdot \mathbf{C}, \quad (4.26)$$

from which the coefficient vector \mathbf{C} can be determined as,

$$\mathbf{R}^{-1} \cdot \mathbf{R}_k = \mathbf{C}. \quad (4.27)$$

The matrix \mathbf{R} can be inverted using singular value decomposition (SVD) technique as follows [53]. Any non-singular $N \times M$ matrix \mathbf{R} (with $N \geq M$) can be decomposed into three matrices as

$$SVD(\mathbf{R}) = \mathbf{U} \mathbf{S} \mathbf{V}^T, \quad (4.28)$$

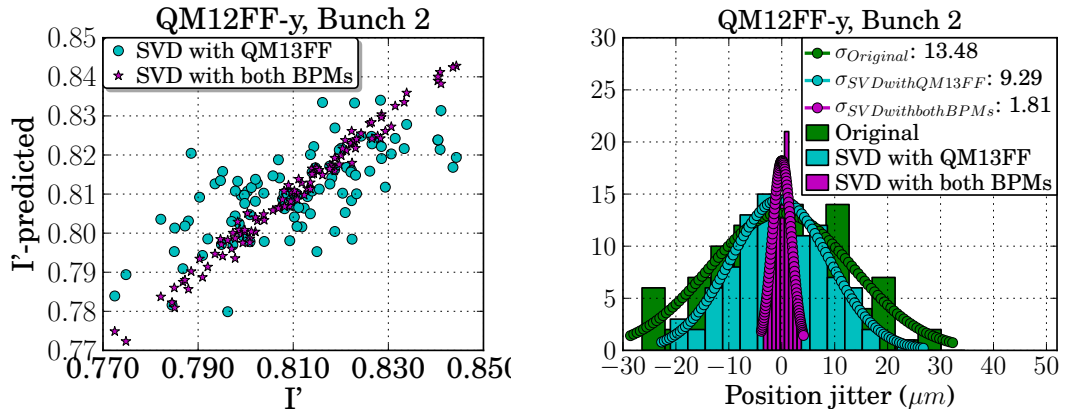
where \mathbf{U} is $N \times M$ column orthogonal matrix, \mathbf{V}^T is a transpose of an $N \times N$ orthogonal matrix and \mathbf{S} is a diagonal matrix of singular values. The position matrix \mathbf{R} can be

inverted as,

$$\mathbf{R}^{-1} = \mathbf{V} \mathbf{S}^{-1} \mathbf{U}^T. \quad (4.29)$$

Using the inverted matrix \mathbf{R}^{-1} in the Eqn. 4.27, the coefficients \mathbf{C} can be calculated and used to predict the bunch position at the CBPM under test. The predicted positions can be considered as the variation in the beam position, and can be subtracted from the measurement to find the system resolution. The built-in SVD function in a module of SciPy was used to correlate the phasors.

To determine the position resolution for the second bunch after application of the signal subtraction algorithm, CBPM signals from 100 machine pulses were recorded and bunch positions were calculated. Fig. 4.23(b) shows the histograms of the position errors calculated for the y positions of the second bunch measured by the MQM12FF. Gaussian curves are fitted to the peaks of the histograms using a least square minimisation technique. The width of the Gaussian fit gives the error in the measurement. To remove the error in position measurement due to actual beam position jitter, SVD based jitter subtraction was applied using correlation with the x and y positions measured by MQM11FF and MQM13FF.



(a) A plot showing the degree of correlation between the measured I' , and I' predicted using the SVD based correlation with one and both CBPMs.

(b) Error in position measurements, before and after SVD based jitter subtraction with one and both CBPMs.

Figure 4.23: Plots showing correlation with SVD based prediction, and reduction in position residual after SVD based jitter subtraction.

Between -1 as inverse-correlation to, 0 as no correlation and 1 as the complete cor-

relation; the measured I' from MQM12FF were correlated to the measured I' from MQM11FF and MQM13FF by 0.97 and 0.68 respectively. The same can be observed in Fig. 4.23(a), where the I' measured with MQM12FF are weakly correlated to the I' predicted by SVD with MQM13FF alone, than the I' predicted using SVD with MQM11FF and MQM13FF both.

In addition to the original position error (without any jitter subtraction), Fig. 4.23(b) also shows the histograms for the remaining position error after SVD based jitter subtraction. Because MQM12FF is weakly correlated to MQM13FF, the jitter subtraction using only MQM13FF was less effective than using both of the CBPMs. The original position jitter of $13.48 \mu\text{m}$ reduced to $1.81 \mu\text{m}$ after jitter subtraction using both of the CBPMs. The error remaining, after position jitter subtraction, in the position measurements for both bunches with the three CBPMs under test are listed in Table 4.8.

Table 4.8: Error in position measurement after SVD based beam position jitter subtraction.

CBPMs	Error in position measurement (μm)			
	x position		y position	
	Bunch 1	Bunch 2	Bunch 1	Bunch 2
MQM11FF	2.18 ± 0.62	2.15 ± 0.74	1.97 ± 0.47	3.01 ± 0.87
MQM12FF	1.53 ± 0.27	2.37 ± 0.68	1.03 ± 0.20	1.81 ± 0.46
MQM13FF	4.08 ± 1.13	7.29 ± 2.90	1.24 ± 0.34	1.74 ± 0.49

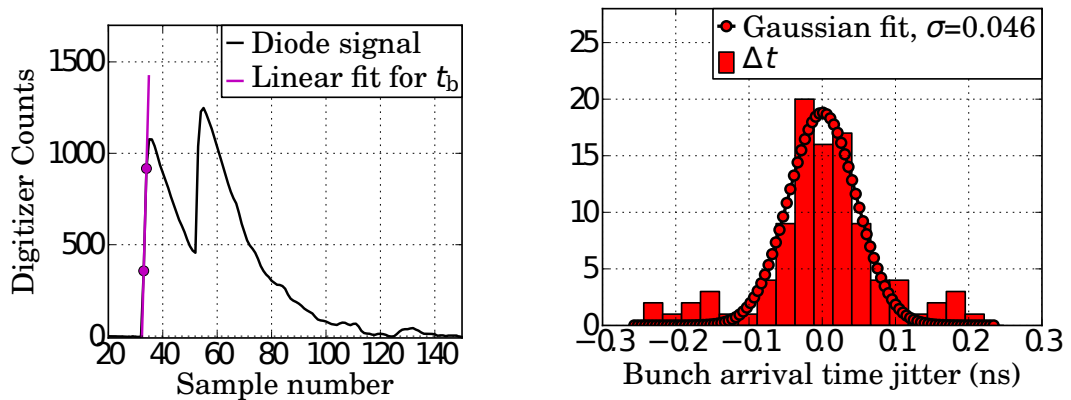
d) Effect of bunch arrival time error and filter limitations

In addition to the beam position jitter, the measured position error includes errors because of the bunch arrival timing. In the signal subtraction algorithm it is assumed that the bunch separation (Δt_b) is constant, and the amplitude from the previous bunch has decayed accordingly. If the bunch arrival and digitisation time changes by Δt , it adds an error in the position $\Delta y_{t,n}$ of,

$$\Delta y_{t,n}(\Delta t) = B_{n-1} e^{-\frac{\Delta t_b}{\tau}} \left(1 - e^{-\frac{\Delta t}{\tau}} \right) \times S, \quad (4.30)$$

where B_n is the net amplitude sampled during the previous bunch, S is the position scale factor and τ is the time decay constant of the signal. All equations for error calculation mentioned in this section can be used for a dipole as well as reference signals.

The bunch arrival time jitter is determined from the rising edge of the reference signal detected using a diode, as shown in Fig. 4.24(a). The variation in the bunch arrival time during a calibration run is shown in Fig. 4.24(b), with a fitted Gaussian distribution. The Δt distribution has width of 50 ps, which includes the digitiser clock jitter, and hence is the maximum possible variation.



(a) Determination of bunch arrival time t_b from a reference cavity signal detected using a diode. (b) Variation in the bunch arrival time. (Δt)

Figure 4.24: Determination of the bunch arrival time t_b and its variation.

In the case of a longer bunch train, the signal amplitude B_n increases with the number of bunches n . From Eqn. 4.30, the error in the position due to arrival time jitter should increase for the bunches towards the end of the bunch train. The signal from CBPM MQM13FF has an amplitude decay time constant τ of 316 ns. For two bunches at a position offset of 400 μm and arrival time jitter of 50 ps, the error in the second bunch position, calculated using Eqn. 4.30, should be of the order of 35 nm.

Other than the amplitude subtraction, the error in the timing will also add error to the phase of a CBPM signal phase, given by,

$$\Delta\phi_t = \Delta t \times \omega, \quad (4.31)$$

where $\Delta\phi_t$ is the phase change due to the change in the bunch arrival time, and ω is the angular frequency of the digitised IF signal. From the jitter in the measured phase (ϕ or θ), the timing error Δt can be verified using Eqn. 4.31. For an IF signal frequency of 26 MHz, the 50 ps error in t_b should vary the phase by 0.008 radian. On the other hand, the observed error in the DDC phase (ϕ_1) for the first bunch, as shown in Fig. 4.25, was of the order of 0.07 radian. The observed phase error is an order of magnitude larger than that which could be induced by bunch arrival time variation, the position error calculated using Eqn. 4.30 increases to $0.5 \mu\text{m}$.

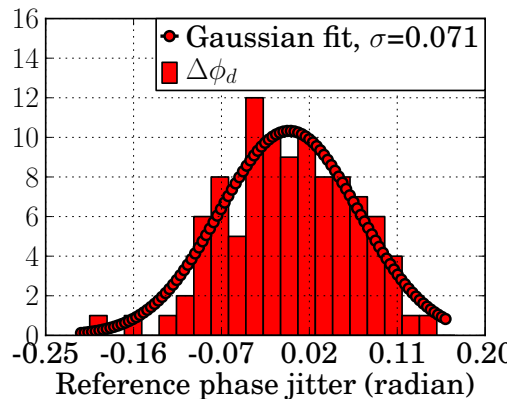
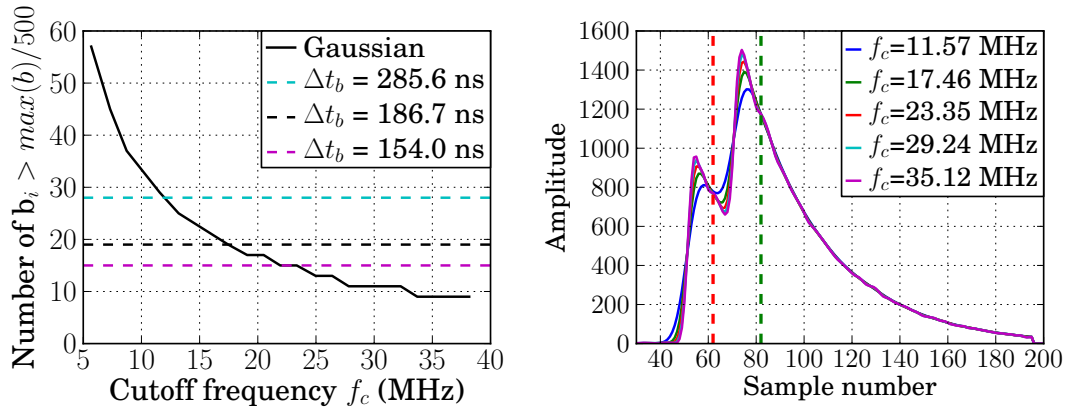


Figure 4.25: Variation in DDC phase.

Another source of amplitude error is the filtering of the higher harmonic signal components (with 2ω frequency) generated during the process of frequency down conversion, which are removed using a low pass filter. The bandwidth of the LPF is limited by the bunch separation. Depending on the digitisation rate, the digital filters suffer from the limited number of samples available for filtering. To measure the position of an individual bunch, only the sample points between consecutive bunch arrivals should be used. This limitation on the window width limits the minimum cutoff frequency of the digital LPF.

Fig. 4.26(a) shows the window width of the Gaussian LPF with different cutoff frequencies. An ideal Gaussian filter of any bandwidth has an infinite width in time. The effective temporal width of the filters was calculated by determining the sample number i at which the filter coefficient b_i is reduced to $1/500$ th of the maximum value b_0 . In between bunches separated by 154, 186.7 and 285.6 ns, the signal digitised at 103.95 Msamples/sec will have 16, 19 and 28 samples respectively. The corresponding

LPF bandwidth lower limits are 25, 19 and 13.2 MHz. The DDC amplitudes calculated using Gaussian LPFs of different bandwidths are shown in Fig. 4.26(b). Because the two bunches were separated by 186.7 ns the filters needed to have larger bandwidth than 19 MHz, otherwise the filter would extend into regions of signal from the neighbouring bunches.



(a) Width of the convolution window of a Gaussian LPF

(b) DDC amplitude from a CBPM signal calculated using Gaussian LPFs of different bandwidths

Figure 4.26: Effects of the digital LPF of different cutoff frequencies on the convolution window and signal amplitude.

For an IF signal with frequency f_{IF} of 26.3 MHz, the 2ω component has frequency of 52.6 MHz, which is above the digitiser Nyquist frequency of 51.96 MHz. The attenuation α_{LPF} of the 2ω component calculated from the frequency responses of the Gaussian LPFs with different bandwidths are plotted in Fig. 4.27(a). A filter with cutoff frequency of 19 MHz should attenuate the amplitude of the 2ω component $A_{2\omega}$ by 250 dB. After mixing, the amplitude of the 2ω component will be the same as the DC component A . After application of a LPF, the attenuated amplitude $A_{DDC,2\omega}$ is,

$$A_{DDC,2\omega} = \alpha_{LPF} \times A. \quad (4.32)$$

The error in the bunch position, because of the 2ω term, can be estimated as α_{LPF} times the measured position offset. For a position offset of 1 mm the error should be of the order of 0.28 fm. Fig. 4.27(b) shows the error in the position measured with MQM13FF along x and y -axis, when the signals were processed using LPFs of different

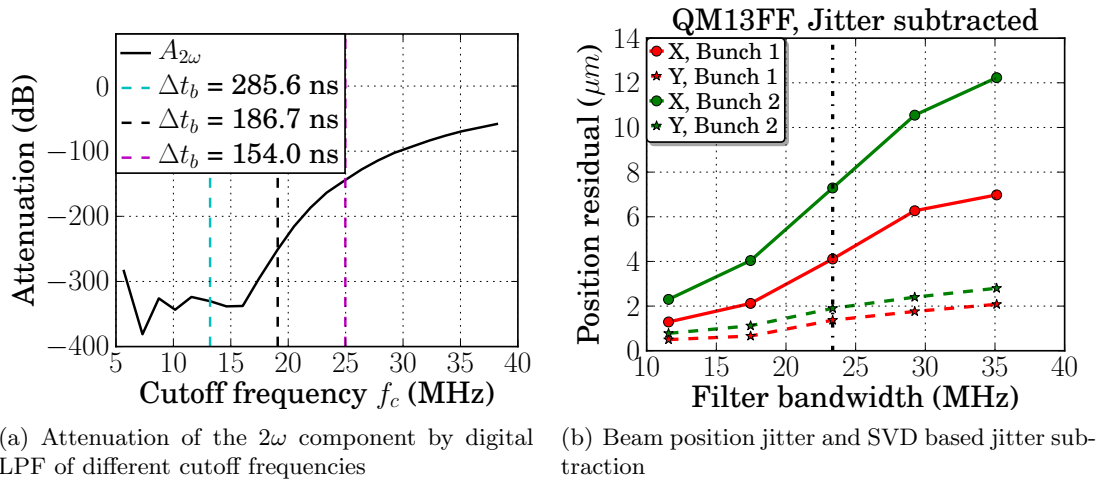


Figure 4.27: Effects of digital LPF with different cutoff frequencies on signal processing and resolution.

bandwidths. The position errors are after SVD based jitter subtraction with rest of the two CBPMs. The jitter decreases with the decrease in the LPF cutoff frequency. With LPF of bandwidth 17 MHz and below, the error in the y -position reduced to smaller than $1.0 \mu\text{m}$, which is considerably more than expected error of 476 nm .

Along with DDC amplitude, the 2ω term will also generate an error in the signal phase $\Delta\phi_{2\omega}$ given by,

$$\Delta\phi_{2\omega} = \tan^{-1} \left(\frac{A \sin(\Delta\phi) + A_{2\omega} \sin(2\omega\Delta t + \phi_{2\omega})}{A \cos(\Delta\phi) + A_{2\omega} \cos(2\omega\Delta t + \phi_{2\omega})} \right), \quad (4.33)$$

where ϕ is the phase of the cavity signal and $\phi_{2\omega}$ is the phase delay due to digital LPF at $2f_{\text{IF}}$. For such a small expected value of $A_{\text{DDC},2\omega}$ and Δt the error in phase due to 2ω component can be neglected.

4.4.2 Signal subtraction for three bunches

To test the signal subtraction method on three bunches, a cavity was calibrated during a FONT shift, when the ATF was operated with three bunches separated by 154 ns . The cavity MQM13FF was moved along the y -axis in three steps of $100 \mu\text{m}$. At the first two steps, signals from 50 pulses were recorded, while 500 pulses were recorded at the third

step to calculate the position error. To verify the performance of the signal subtraction algorithm with three bunches, cavity signals were simulated using the signal simulation code discussed earlier in this chapter. Experimental and simulated digitised signals, induced from a machine pulse of three bunches, are shown in Fig. 4.28. Signals were processed in a similar way as for two bunches, using the DDC process and a Gaussian digital LPF of 25 MHz, to calculate the amplitude, shown in Fig. 4.28, and phase.

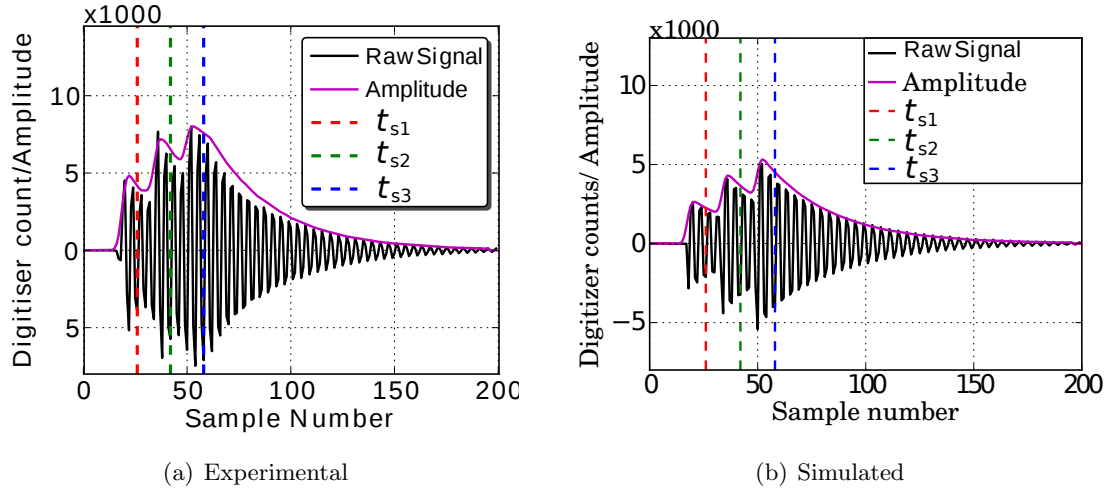


Figure 4.28: Digitised raw signal and processed amplitude induced by three bunches.

I and Q phasors were calculated at sample time t_s during the signals excited by each of the three bunches, which are plotted in Fig. 4.29. The first column in Fig. 4.29 shows the IQ diagrams from experimental signals, without and with signal subtraction. For a time decay constant of 303 ns, the amplitude of the signal induced by a bunch had decayed to only 60% when the next bunch arrived. Similar to the phasors from two bunch data, the amplitudes of the phasors from the second and third bunches were significantly overestimated.

An other point to notice is that the phase difference between the phasors from the consecutive bunches $\Delta\Theta_{IQ}$ are not even. For a frequency difference of 1.1764 MHz between the dipole and reference cavities, the phase difference after 154 ns should be 1.13 radian. The observed phase difference between the first and second bunch phasors was 0.76, while it was 0.87 radian between the second and third bunch. The positions of the second and third bunches calculated from these phasors, without signal subtraction, were overestimated by 25% and 67% respectively. Similar to the experimental signals,

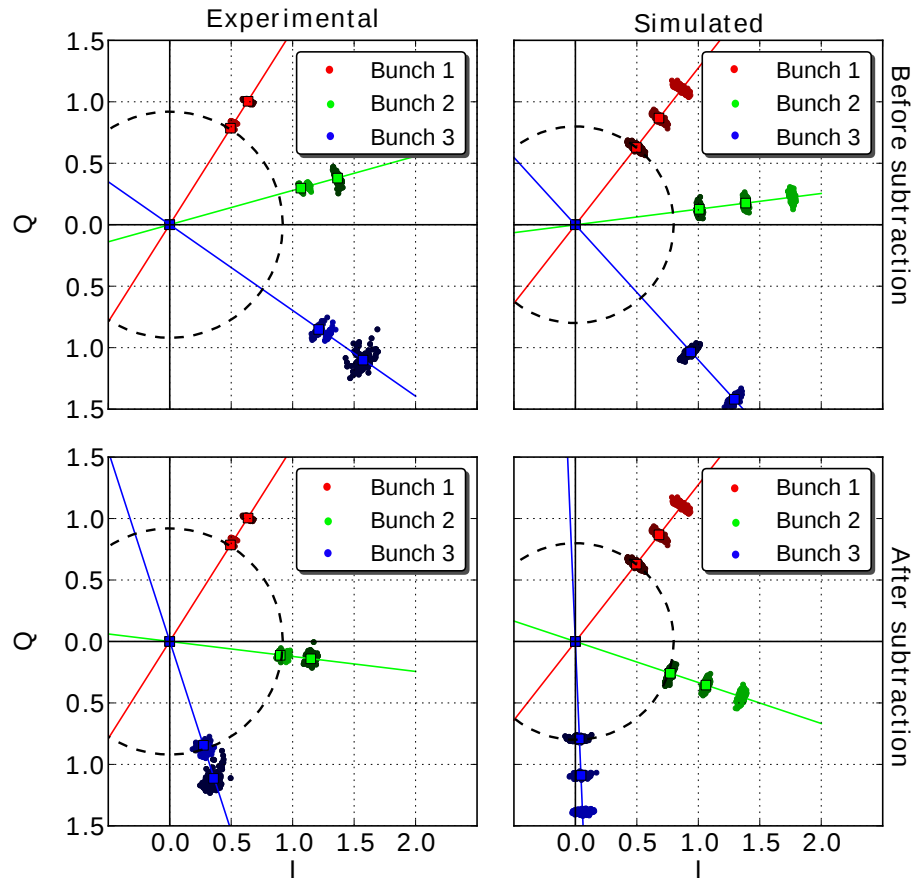


Figure 4.29: IQ plots from experimental and simulated signals induced by three bunches.

the phasors from the simulated signals also result in an over estimated position.

To remove the error, the signal subtraction algorithm was applied to the phasors. As mentioned earlier, the decayed phasors measured during the second bunch were subtracted from that of the third, and of the first from the second. The IQ phasors after signal subtraction are plotted in the bottom left of Fig. 4.29. As the signal pollution is removed, the error in position of second and third bunch reduced to 2%, from 25% and 67% respectively. The phase difference between the consecutive bunches are 1.16 and 1.14 radian, which agree well with the prediction of 1.13 radian. Similar to the experimental data, after subtraction, the simulated phasors have same amplitude and even phase difference between bunches.

The subtracted IQ phasors were rotated by rotation angle Θ_{IQ} , and position of the

bunches were calculated using position scale factor S . A histogram of the position residuals from the experimental and simulated data are plotted in Fig. 4.30. The trace label B1-S26 means for the first bunch sampled at the 26th digitiser sample. The jitter in experimental data grows with the bunch number, while simulated data shows no increase. This can also be seen in the IQ diagrams of Fig. 4.29. As the simulation did not include any non-linear effect in the processing electronics, it was suspected that saturation occurs when the amplitude grows due to the addition of the signals.

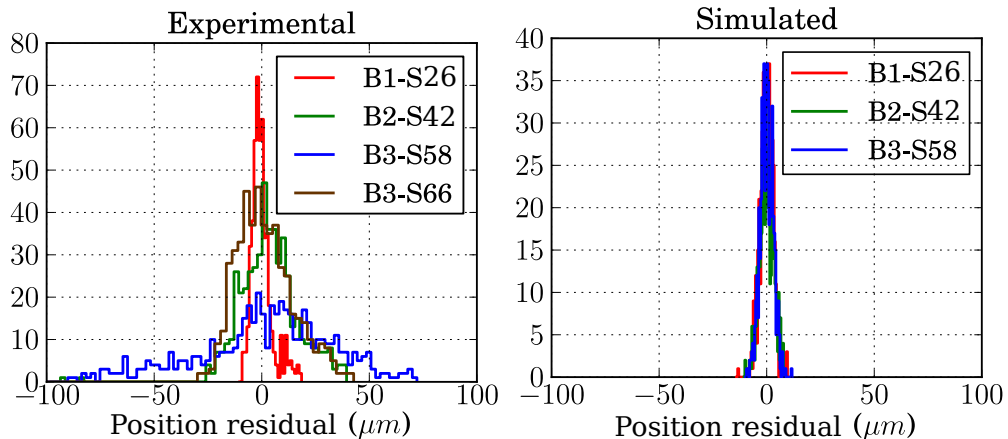


Figure 4.30: Histogram of jitter from experimental and simulated signals induced by three bunches.

If the linearity in the electronics and digital processing of the CBPM signal is maintained, the DDC amplitude should retain its exponential decay. The amplitudes of the CBPM signals recorded from 500 machine pulses, at the third mover position step during the calibration were used to verify the exponential decay. Fig. 4.31 shows the ratio of the DDC amplitude at a sample to the amplitude after 16 digitiser samples (e.g. amplitude at sample 58 divided by amplitude at sample 74). For a dipole cavity with decay time constant τ_d of 303 ns, the amplitude ratio should be 1.66. The sample numbers from 58 to 66, after arrival of the third bunch, were used for the study.

When sampled at 58, the amplitude ratio had strong dependence on the amplitude, for amplitude values higher than 5900 digitiser counts. The ratio decreases down to 1.5, and the exponential relation was no longer valid. The most probable reason for this nonlinear behaviour at higher amplitude can be some non-linearities in the electronics. Sampling at a later time allowed to avoid this problem, either partially (sample number

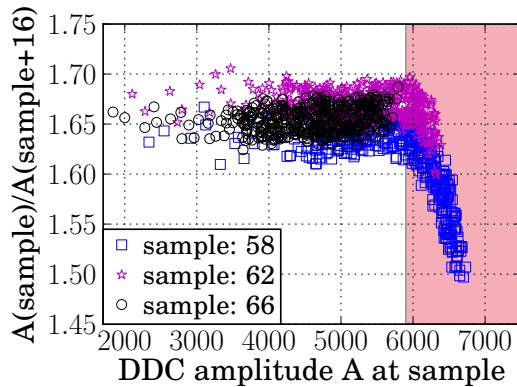


Figure 4.31: Plot of signal amplitude ratio, separated by 16 samples, as function of amplitude at the first point.

62) or completely (sample number 66).

As shown during the linearity measurements in Fig. 4.5(a), the response of the RF electronics card was linear over an input power range of more than 70 dB. The same can be seen in Fig. 4.32, where the gain is plotted for different digitised output voltage. The gain is almost constant for digitised amplitudes higher than 5900. To resemble the decrease in the amplitude ratio of 9.6% (from 1.66 to 1.5), the gain should also be compressed by corresponding amount, which was not observed.

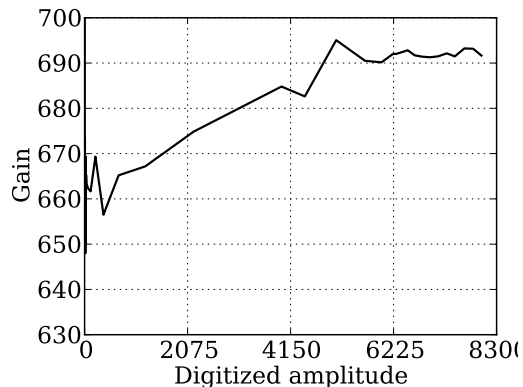


Figure 4.32: Gain at different digitised output signal amplitudes

The same subtraction algorithm was applied with the third bunch sampled at a sample number of 66. The position scale factor was increased accordingly, assuming an exponential decay. As shown in Fig. 4.30, the residual for the third bunch decreases to the same level as the second bunch. Table 4.9 summarises the RMS values of the measured

position. Although avoiding the nonlinear region reduces the RMS position for bunch 3, the variation in position of bunches 2 and 3 were almost four times larger than that for the bunch 1.

Table 4.9: RMS position jitter measured for three bunches

Bunch No	RMS position residual (μm)	
	3 rd Bunch Sample no	
	58	66
1	3.51	3.51
2	13.06	13.06
3	40.98	12.99

As nonlinearity in electronics is ruled out, another possible reason for the large position jitter for bunch 2 and 3 could have been the effect of the FONT system. As the cavity pulses were not recorded in synchronization with the FONT measurements, it is not possible to verify if the FONT was kicking the third bunch and by what amount.

4.5 Summary

The processing of the CBPM signals induced by multiple bunches were studied at ATF2, while the ATF was operated in two or three bunch modes. A signal induced by a bunch was polluted by the signals induced from previous bunches, which overestimated the bunch position by 67%. A signal processing method has been developed which removes the signal pollution using a signal subtraction algorithm. The signal subtraction algorithm was applied to the CBPM signals induced by two and three bunches in the CBPMs at ATF2. The algorithm removed the signal pollution which reduced the measurement error to less than 2%. The phase jump between the consecutive bunches was studied and it was due to the frequency difference between the dipole and reference cavities. With this study, it is possible to apply the calibration constants derived from the single bunch calibration to calculate the bunch position of any bunch with a known bunch separation. The application of signal subtraction algorithm extended the use of the existing CBPM system, with relatively high Q cavities, to the next generation accelerators using a beam with a shorter bunch separation.

Chapter 5

Cavity BPM with pre-aligned and separated dipole modes

Cavity design features, such as deliberate pre-orientation of the dipole modes by introducing a resonant frequency split between x and y position signals to improve the isolation, and extraction of beam position without any mechanical tuning of the cavity, were studied through a collaborative project with Diamond Light Source. The project was to design a prototype cavity BPM system for the proposed Next Light Source (NLS). Because the NLS project has been postponed, it was decided to use the same design for the Diamond Light Source. This chapter includes explanation of the design and simulation of the CBPM, which is followed by the laboratory RF testing, and finally some initial results from the beam testing are discussed. All design and simulation work discussed in this chapter was carried out in collaboration with the Diamond Light Source. The RF parameters of one of the fabricated cavities were tested at Royal Holloway University of London (RHUL). The beam tests on the cavity were carried out at the Accelerator Test Facility (ATF) at KEK in Japan.

5.1 Next Light Source

NLS is a proposed free electron laser (FEL) facility by the Science and Technology Facility Council (STFC) of UK. Its conceptual design report was prepared and the potential applications have been thought through. NLS will use FEL radiation from an electron bunch to produce an ultra-intense and ultra-short laser pulses in the wavelength range from THz to soft X-ray [54]. This synchrotron radiation will be used as a fast and intense radiation source for various optical analysis experiments, based on the diffraction and spectroscopic measurements. With its ultra-short laser pulses, NLS should be able to provide the following scientific benefits [54],

- Nanometer scale imaging of arbitrary objects in their native state: Capturing a living cell at nanometer resolution,
- Measure the mechanisms of physical and chemical processes at an atomic scale: Making molecular movie,
- Control electronic processes in matter: Directing attosecond dynamics.

To perform above scientific studies, the NLS is proposed to generate laser pulses as short as 20 fs pulse length, and in energy range from infrared (IR) to 5 keV soft X-ray. The choice of the beam energy for NLS FEL is mostly limited by the tuning range and polarisation of the radiator undulator [54]. To produce such a short high energy laser pulses, 32 ps long bunches of 10^{10} electrons per bunch will be accelerated up to 2.25 GeV energy in NLS. The BPM project began as a project to design a cavity BPM system for the NLS accelerator, which was then redirected to the Diamond Light Source on postponement of NLS.

5.2 Diamond Light Source

Diamond Light Source is a third generation national synchrotron facility of United Kingdom, opened in 2007 at Rutherford Appleton Laboratory (RAL) campus in Ox-

fordshire. It is a user facility which provides a high intensity synchrotron radiation beam over a wave length range from infrared to X-rays [55].

The intense X-ray pulses generated at Diamond are used for various studies over many scientific disciplines, such as Chemistry, Environmental study, Life science, Earth science and Engineering. For example, pharmaceutical companies can study structural information of the samples, using molecular crystallography with extreme time and spacial resolution, to improve the performance of the drug [56]. Biological processes such as protein denaturation, phase separation, binding and unbinding, are studied using the non-crystalline diffraction techniques using X-rays. In material science, the structure and morphology of a thin film object, such as a high temperature superconducting film, are studied using diffraction of the high intensity X-rays.

5.2.1 Machine information

A schematic layout of the facility is shown in Fig. 5.1 [57]. Diamond Light Source can be classified into three main sections, linac, booster ring and main storage ring. The pre-injector linac provides a primary input beam to the booster ring. It can be operated in a short or long pulse mode, with pulse duration of 1 ns or 300 - 1000 ns respectively [58]. Pulses of 50 pC to 3 nC can be generated with pulse repetition rate from single shot to 5 Hz. The electron gun consists of a thermionic dispenser cathode, which is operated at -90 kV potential difference to the earth. The long pulse generated by the gun is then bunched in a buncher system, which consists of the standing and traveling wave structures at 500 MHz and 3 GHz respectively. The bunched beam is accelerated using two accelerating structures, which have 156 cells and operates in $2\pi/3$ mode at 3 GHz.

The accelerated pulses are inserted into a booster ring for further acceleration and conditioning. The booster is formed of a normal focusing defocusing (FODO) lattice. In the booster, an input beam of 100 MeV is accelerated up to 3 GeV [59]. The input beam is accelerated using RF cavities, providing an accelerating voltage of 1.1 MV at 500 MHz. It is designed for 3 mA beam current and can be operated in a single long

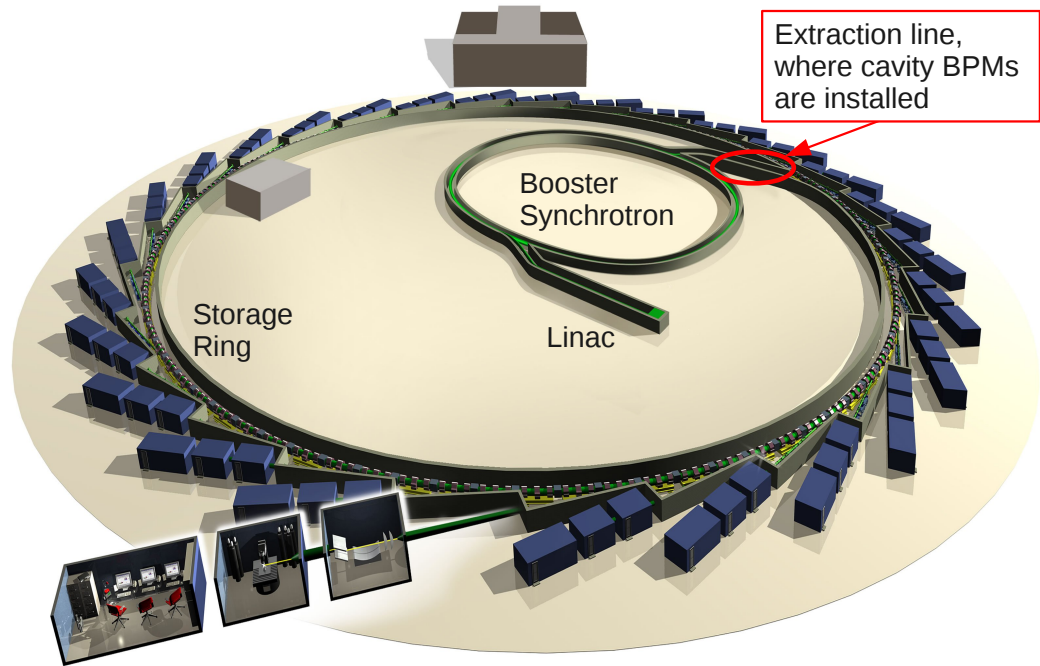


Figure 5.1: Model schematic layout of the Diamond Light Source.

bunch mode or a multi-bunch train mode.

The 3 GeV main storage ring is made of 24 straight cells and has circumference of 561 m [55]. As a third generation light source, it uses the advanced magnet concepts such as superconducting and normal-conducting wigglers to produce the magnetic fields up to 3.5 and 2.0 T [60] respectively. The energy lost through synchrotron radiation of the stored beam current of 300 mA, is compensated by an accelerating structure operating at 500 MHz. The design goal is to store a beam with 300 mA for 100 hours. A beam of 100 mA has been successfully stored for 100 hours during the commissioning of the storage ring [61]. The main parameters of the Diamond Light Source machine are listed in Table 5.1.

The majority of the BPM system installed at Diamond are from LabCA [61, 62]. The beam in the booster synchrotron and storage ring are monitored by 22 and 168 four button BPMs respectively. The BPM signals are acquired and processed using a EPICS and MATLAB based processing system, and results are used to correct the beam using the fast and slow feedback systems. Using the feed back system, the beam size could

Table 5.1: Major parameters of the Diamond Light Source storage ring.

Parameter	Value
Electron beam energy (GeV)	3
Number of cells	24
Circumference (m)	561.5
Beam current (mA)	300
Beam emittance (nm-radian)	2.74 (horizontal) and 0.0274 (Vertical)

be reduced to the nominal emittances of 2.7 and 0.03 nm rad in the horizontal and vertical directions respectively [61].

Well controlled injection into the storage ring provides a better starting conditions and improves the performance of the storage ring. The new CBPMs were planned to be installed in the extraction line, from the booster ring to the storage ring, to provide better measurement of beam position. If installed in either of the rings, the system will get saturated from the revolving high current beam. In addition, the required space was available in the extraction line with minimum changes required.

5.3 Cavity BPM design and EM simulations

While designing a CBPM, each dimension can be chosen to improve the system resolution and to provide efficient post processing. With an increase in the resonant frequency of a cavity, the size of entire CBPM structure decreases. A CBPM structure designed in the C-band frequency range will be compact, while large enough to be machined with sufficient accuracy. In addition, high quality components for the processing electronics are available at cheaper price because of the advances in the radio communication field in this frequency range. With all above factors, it was decided to design the CBPM in the C-Band frequency range.

During the design process, after deciding the geometry shape and approximate values of all dimensions, the CBPM structure is simulated using various electromagnetic codes to predict its performance and to optimise the dimensions. The simulation process flow and different simulation packages used for this study are explained subsequently.

5.3.1 Software packages for EM simulations and post-processing

The workflow of simulations through the softwares installed at different locations are shown in Fig. 5.2. The 3-dimensional (3D) geometries of the CBPM structures were first created in Cubit [63]. Cubit is a software toolkit, which is developed, distributed and supported by Sandia and its sister laboratories in USA. The complex geometries can be built using the standard 3D volumes, or from scratch using the geometry components such as points, curves and surfaces. New geometries can be created by boolean operations such as addition, subtraction or intersection of the existing geometry components. The geometries can be divided by symmetry planes, and different boundary conditions can be assigned. Individual volumes can be grouped together in a block to assign them same properties, such as the volume material type. Cubit installed on a stand alone desktop was capable to create the CBPM geometries for this study.

The actual EM simulations are performed using two software packages, GdfidL [64] and ACE3P [65]. For GdfidL, a geometry created in Cubit was exported in the Standard Tessellation Language (STL) file format. ACE3P codes accept a tetrahedral mesh in the NetCDF format. The geometry was meshed in cubit using first or second order tetrahedral elements, which was then exported as a Genesis file. The Genesis file was converted into the NetCDF format using ACDDTool [66].

GdfidL is a 3D EM simulation software, which can be operated on serial or parallel computers [64]. GdfidL has a built-in module for geometry creation through a command script, but Cubit was preferred because of its graphical interface and flexibility to modify individual volumes. GdfidL can compute the EM fields in a lossless or lossy structure. It has an internal mesh generator to produce cuboidal mesh with linear mesh elements. GdfidL uses an Eigenmode solver to identify the resonant modes and time domain solver to compute the EM fields in a geometry. From the computed EM fields, the post-processors can compute various parameters such as, Q values, shunt impedance, S-parameters and wakefields. At Royal Holloway, GdfidL runs on a Beowulf cluster with 54 nodes.

Advanced Computational Electromagnetic 3D Parallel (ACE3P) is a finite element (FE)

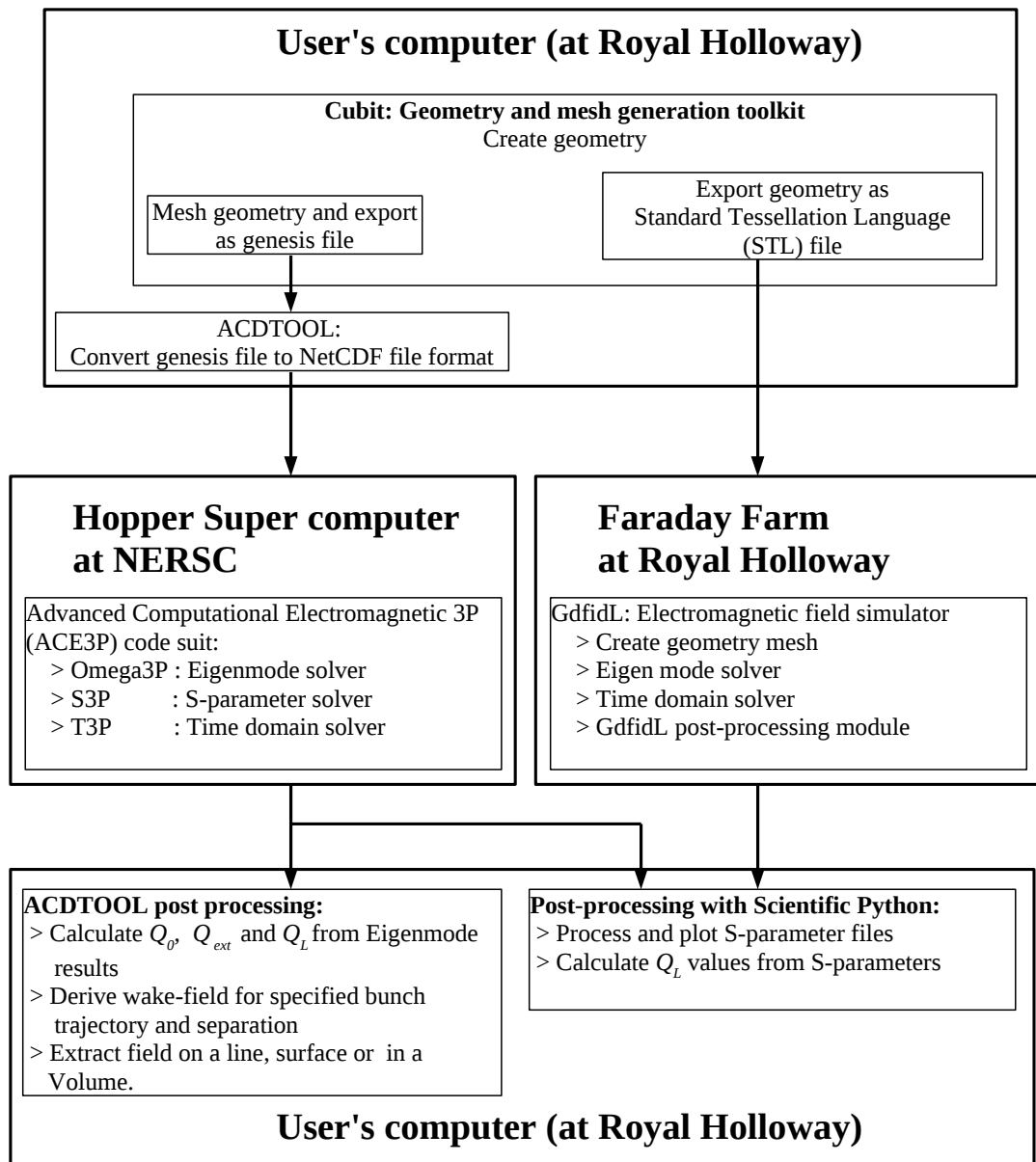


Figure 5.2: Simulation workflow and distribution of software on various computer systems.

based code suit which includes solvers for electromagnetic, particle tracking and thermal simulations [65]. They can solve field problems for lossy and lossless materials. Within the ACE3P suite, Omega3P is an Eigenmode solver used to simulate the resonant modes of a structure [67]. It calculates electric and magnetic field patterns for each mode along with surface current density. Omega3P also calculates the internal quality factor (Q_0), and external quality factor (Q_{ext}) if ports are defined. From the EM fields calculated

by Omega3P, the normalised shunt impedance (R/Q) of an individual resonant mode, experienced by a bunch traversing along a linear trajectory, can be calculated using ACDDTool.

The impedance matching between different parts of a CBPM can be simulated using an S-parameter solver S3P. The S-parameters are derived as a ratio of the received and transmitted voltages at ports, normalised to the line impedance [19]. S3P calculates complex S-parameter values at specified frequencies, and writes them in a file in a standard array format.

The beam coupling efficiency of a CBPM was studied, by simulating a charge particle bunch passing through it, using a time domain solver T3P. User can specify the bunch charge distribution, bunch length, speed and its linear trajectory of propagation. The charge in a bunch is distributed only along its length (along the direction of propagation), while the bunch resembles only a point on the transverse plane. It calculates the EM field induced by the moving bunch, from which its propagation or build up with time can be studied. The wake potential that would be experienced by a following bunch with different bunch separation can be calculated using T3P.

ACE3P codes were used on the supercomputers at National Energy Research Scientific Computing (NERSC) facility, located in Berkeley California. The NetCDF geometry mesh file and other simulation setup files were copied to NERSC, where they were solved in parallel mode. The simulation results were copied back to user's computer for post-processing and visualisation. The simulated EM fields were visualised using ParaView. The results from S-parameter simulations were processed using SciPy.

ParaView is an open source visualisation software which can work on multiple platforms [68]. The electromagnetic fields simulated using Omega3P and T3P were viewed and analyzed in ParaView. The fields can also be plotted on any cross-section plane. The values of the electric and magnetic field components on a point, curve, surface and inside a volume can be extracted for processing. The propagation or build up of the fields inside any structure can also be visualised as moving time frames for better understanding.

ACE3P codes benefit from the tetrahedral mesh with curved elements and spacial discretisation. On other hand with GdfidL, user has more explicit control on the mesh generation. Use of ACE3P codes had advantages from efficient parallel processing and execution on vast computational resources, but required many different softwares during a simulation cycle and data transfer. Using GdfidL had the benefits of integrated software modules and local data availability, but it was limited by the resources available at Royal Holloway. It was preferred to use ACE3P over GdfidL, but GdfidL was used when it was difficult to mesh any complex geometry using Cubit. Most of the electromagnetic simulations during the project were cross compared by three different packages, CST, GdfidL, and ACE3P. The GdfidL and ACE3P codes were used to simulate various models at Royal Holloway, while the same geometries were simulated using CST at the Diamond Light Source [69].

5.3.2 Resonant cavity

The Diamond RF system runs at 499.654 MHz. It is foreseen to use a higher order harmonic of the RF system frequency to provide local oscillator (LO) signal for the electronics of the CBPM system. Even when an external LO source is used, the frequency of the LO should be kept at an integer multiple of the RF system frequency to phase lock the LO to use the CBPMs for position feed-back and correction.

a) Cavity Radius

The thirteenth harmonic of the machine RF system frequency falls at 6495 MHz, which will be used as an LO frequency (f_{LO}). An electronic frequency down conversion and signal processing scheme, similar to the one discussed in Section 4.2 for the CBPMs at ATF2 beam line, will be implemented for the CBPM system at Diamond as well. From the Nyquist theorem, a digitiser with digitisation rate of 250 Mega-samples per second limits the processing bandwidth to 125 MHz. For accurate frequency and phase determination of the digitised signal, at least 5 sample points per signal cycle are required. The IF signal with frequency ($f_{IF} = f_{RF} - f_{LO}$) of less than 50 MHz will

have enough oscillation cycles between the consecutive bunches, and it satisfies the digitisation requirements. The choice of 20 MHz as the IF frequency sets target for the BPM signal frequency to be at 6475 MHz, with lower limit at 6445 MHz.

To benefit from the previous design experience and for the ease of manufacturing, a cylindrical cavity was chosen as the resonant structure. From Eqn. 2.4, the radius b of a vacuum filled cylindrical cavity, corresponding to the dipole frequency of 6475 MHz is calculated,

$$b = \frac{1}{2\pi} \frac{1}{\sqrt{\mu_0\epsilon_0}} \left(\frac{j_{11}}{f_{110}} \right) = 28.23 \text{ mm}, \quad (5.1)$$

where f_{110} is the resonant frequency of the dipole mode, j_{11} is the first zero of the Bessel function (J_1) which describes the electric field distribution of the dipole mode, ϵ_0 and μ_0 are the permittivity and permeability of vacuum respectively.

The resonant frequencies of the monopole, second monopole and quadrupole modes of a pillbox cavity with a radius of 28.33 mm, calculated using Eqn. 2.4, will be 4.0, 8.7 and 9.3 GHz respectively.

b) Cavity height

The amplitude of EM fields induced by a bunch in the cavity increases linearly with the cavity length (Section 2.2.1). This linear increase is attenuated by the transit time factor (α_{TT} in Eqn. 2.10) because of the oscillating nature of the RF voltage. Fig. 5.3 shows the transit time factor for the monopole and dipole modes of a CBPM with different cavity length l , and a constant radius of 28.33 mm.

From Fig. 5.3 increasing the cavity length reduces the excited monopole and dipole mode, because of the transit time effect, although the dipole mode decreases faster. The relative increase in the monopole mode compared with the dipole mode reduces the system resolution due to the increased pollution of the high frequency tail of the monopole mode at the dipole mode frequency. Also, as can be seen from Eqn. 2.21 and 2.22 the amplitudes of the signals dues to the bunch trajectory and tilts also increase with the cavity length. Considering all these factors an inital value of 8 mm was used

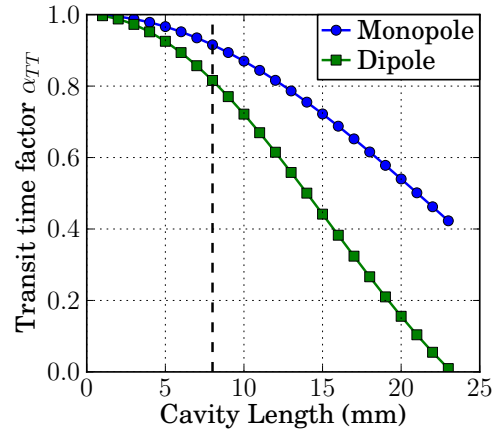


Figure 5.3: Transit time factor α_{TT} for the monopole and dipole modes of a pillbox cavity with different lengths.

for the simulation model.

It is known from previous design experiences that adding a beam pipe and coupling structures to an ideal pillbox cavity reduces its resonant frequencies. Taking this into account, a cavity model with slightly smaller radius was used to simulate the pillbox cavity.

Fig. 5.4(b) shows a simulation model of pillbox cavity for Omega3P, and an axial electric field component for dipole mode. Only half of the pillbox cavity was solved with

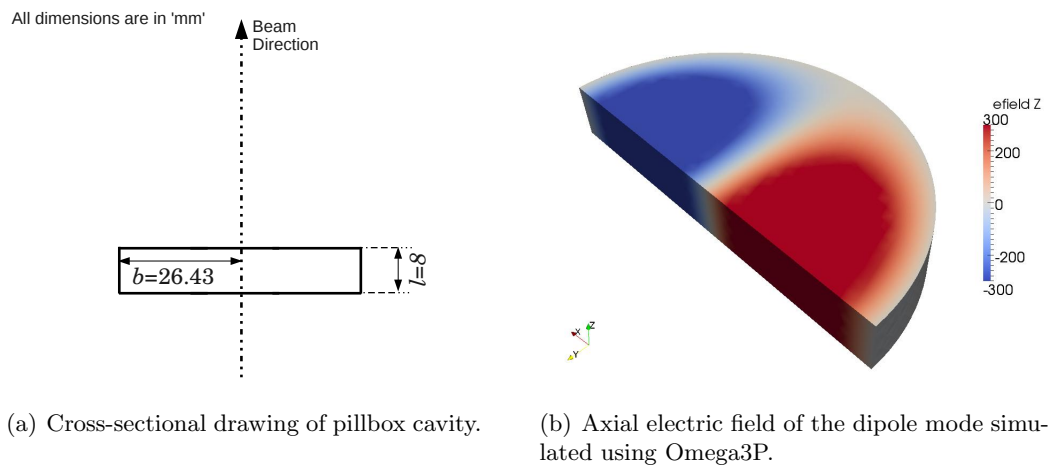


Figure 5.4: Simulation model of pillbox cavity.

magnetic symmetry boundary condition on the x -plane. Imposing a symmetry boundary condition restricts the modes which can be excited in the structure, but can save considerable simulation time while solving larger models. The resonant frequencies of major modes derived using Eigenmode solvers in the three different codes are compared in Table 5.2. The simulated values were in good agreement with the theoretical and the difference among the codes were less than 0.05 %.

Table 5.2: Resonant frequency of a pillbox cavity calculated using different Eigenmode solver packages.

Mode	Resonant frequency $f_{r,\text{pillbox}}$				
	Theory (MHz)	Variation from theory (MHz)			
		CST	GdfidL	Omega 3P	Spread
Monopole	4341.4	-0.2	0.0	1.0	1.2
Dipole	6917.3	-0.5	0.0	1.6	2.1
Quadrupole	9271.2	-1.2	1.1	2.3	3.5

The internal quality factor Q_0 of a pillbox cavity can be calculated as [69],

$$Q_0 = \frac{1}{\delta} \frac{l}{1 + \frac{l}{b}}, \quad (5.2)$$

where the skin depth δ of the material is calculated as,

$$\delta = \frac{2}{\sqrt{\mu \omega \sigma}}, \quad (5.3)$$

where σ is the electrical conductivity of the cavity material, ω is the angular resonant frequency of the mode and μ is the permeability of the material.

Table 5.3: Internal quality factor Q_0 of a pillbox cavity derived using different Eigenmode solver packages.

Mode	Internal quality factor $Q_{0,\text{pillbox}}$				
	Theory	Variation from theory			
		CST	GdfidL	Omega 3P	Spread
Monopole	6132	0	55	-7	62
Dipole	7729	2	75	-15	90
Quadrupole	8948	2	55	-24	79

To design CBPM with relatively high quality factor, copper is the suitable material because of its higher electric conductivity of 5.8×10^7 S/m. The quality factors for the three lowest order modes simulated using Eigenmode solver of three different codes, are compared with their theoretical values in Table 5.3. The values are in good agreement with the theoretical prediction, with spread of 1.5%.

c) Cavity with beam pipe

As shown in Fig. 5.5(a), the cylindrical beam pipes with radius a of 10 mm were added at the both ends of the pillbox cavity to see the effect. Fig. 5.5(b) shows the simulation model and axial electric field component of the dipole mode determined using Omega3P. Simulation results for the primary resonant modes of the structure are tabulated in Table 5.4. The resonant frequency of dipole and quadrupole dropped by the addition of the beam pipe, while the frequency of monopole increased. The quality factor Q_0 did not change much by addition of the beam pipes.

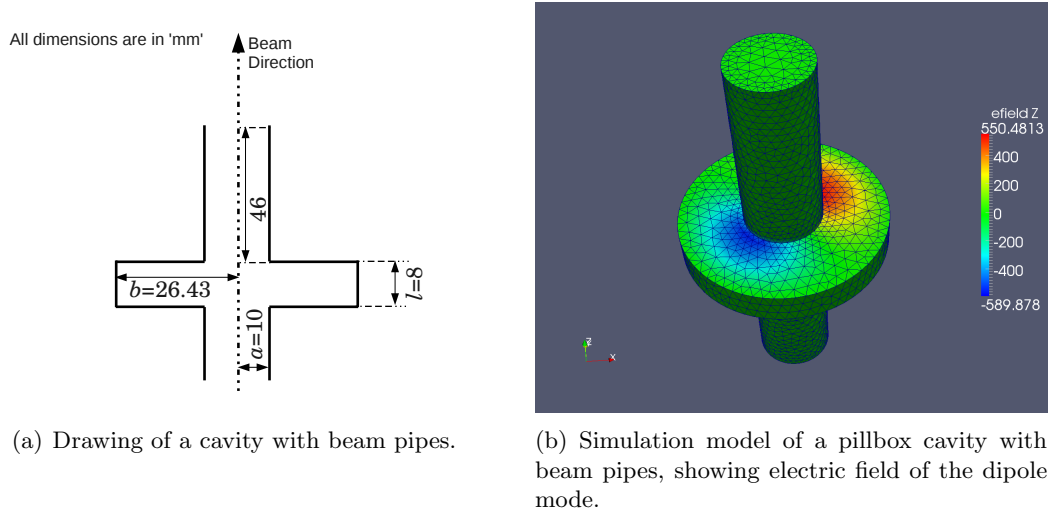


Figure 5.5: Geometry model of a pillbox cavity with beam pipes, solved using Omega3P.

The normalised shunt impedance (R/Q_0) for various modes were calculated using ACD-Tool as a post process on the Eigenmode simulation results. The R/Q_0 for bunch offset of 1 mm showed that the monopole mode is 88 times strongly coupled than the dipole mode, while the quadrupole is 270 times weakly coupled than the dipole mode. As the geometry is symmetric in transverse plane, the orientation of the modes were fixed by

even a small asymmetry in the mesh.

Table 5.4: Eigenmode simulation results of a model with cavity and beam pipes.

Mode	Resonant frequency f_r (MHz)		Quality factor Q_0		$\left(\frac{R}{Q_0}\right)_{1\text{mm}}$ (Ω Cavity)
	f_r	$f_r - f_{r,\text{pillbox}}$	Q_0	$Q_0 - Q_{0,\text{pillbox}}$	
Monopole	4703.0	361.6	6266	+134	71.63
Dipole	6473.4	-443.9	7687	-42	0.81
Quadrupole	9004.5	-265.7	9077	+129	0.0031

The cutoff frequency of the lowest transmission mode TE_{11} for the cylindrical beam pipe can be calculated using Eqn. 2.5, and it is 8.78 GHz. The two highly coupled primary resonant modes, the monopole and dipole, are well below the cutoff frequency of the beam pipe. The power coupled in these modes will not propagate through the beam pipes, and will decay exponentially with length in the pipe.

5.3.3 Waveguide adapter with coaxial coupler

To couple the electromagnetic fields out of the resonant cavity, a slot coupled waveguide was used because of its inherent characteristics as a high pass filter and the restrictions it applies on the orientation of the coupled field. A rectangular waveguide structure is chosen, over a cylindrical, for the following reasons:

- The magnetic field of the cavity dipole mode is aligned with the magnetic field of TE_{10} mode of the rectangular waveguides, which improves the isolation between x and y position measurements.
- The coaxial coupler is more effective with rectangular waveguide compared to cylindrical.
- Because of manufacturing ease, as the coaxial coupler can be mounted more accurately on a plane surface of a rectangular waveguide than on a cylindrical surface.

The dimensions of the waveguide can be chosen such that it restricts the monopole from coupling into the waveguide (as explained in the Section 2.2.1). Fig. 5.6 shows the simulation model of a waveguide adapter with coaxial coupler, along with the dimensions and ports. From Eqn. 2.11, the width A of a rectangular waveguide, given the cutoff frequency $f_{c,10}$ of TE_{10} is,

$$A = \frac{c}{2} \left(\frac{1}{f_{c,10}} \right), \quad (5.4)$$

where c is the speed of light.

As mentioned in Table 5.4, the monopole and dipole frequencies of the cavity-beam pipe structure are 4.7 and 6.47 GHz respectively. The cutoff frequency of the waveguide should be between these two values. A waveguide with 28 mm width (A) will have cutoff at 5.35 GHz, hence it will couple the dipole field while efficiently rejecting monopole.

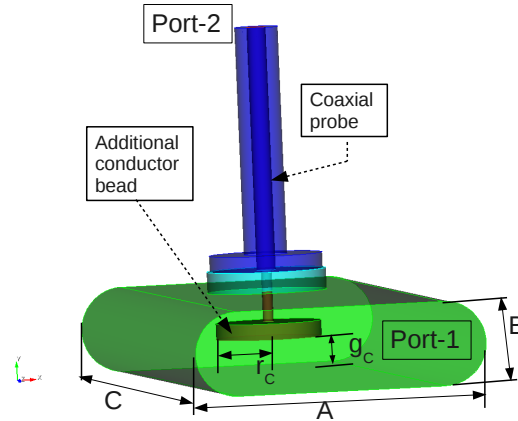


Figure 5.6: Simulation model of a waveguide adapter with coaxial coupler, showing dimensions and ports.

Typically the height (B) of the waveguide is kept around half of its width. Reducing the height increases the capacitance and hence improves the power coupling through capacitive coaxial probe. The lower limit on height is imposed by the space required for coupling probe structure, and possible tolerances.

The guide-wavelength, inside the waveguide, corresponding to the cavity dipole mode frequency can be calculated as [19],

$$\lambda_{g,110} = \frac{\lambda_{110}}{\sqrt{1 - \left(\frac{\lambda_{110}}{\lambda_c}\right)^2}}, \quad (5.5)$$

where λ_{110} is the free space wavelength for the dipole frequency and λ_c is the cutoff wavelength of the waveguide mode, which is twice of the waveguide width ($2A$) for the TE_{10} mode of a rectangular waveguide. The interpretation of position signal becomes complicated if the waveguide also resonates at the dipole frequency of the cavity. To avoid resonance in the waveguide, the length (C) of the waveguide should not be an integer multiple of the half guide wavelength ($\lambda_{g,110}/2$).

The field coupled into the waveguide from the monopole mode will propagate as an evanescent mode, with power decaying along waveguide length by factor $\alpha_{\text{evanescent}}$ given by,

$$\alpha_{\text{evanescent}} = e^{-\frac{4\pi}{c}\sqrt{f_c^2 - f_{r,010}^2}} = -4.64 \text{ dB/cm}, \quad (5.6)$$

where $\alpha_{\text{evanescent}}$ is the amplitude decay factor of the evanescent mode, f_c is the cutoff frequency of the waveguide and $f_{r,010}$ is the resonant frequency of the monopole. To limit the structure length, the waveguide length was chosen to be 60 mm, for which any power coupled from the cavity monopole mode will be decayed by -16 dB at the position of the coaxial probe.

Power coupled into the waveguide is extracted out using capacitive coaxial probe (Fig. 5.6). For maximum coupling of the field at certain frequency, the distance between the probe and the waveguide end wall (the surface opposite to Port-1) should be a quarter of its guide wavelength ($\lambda_g/4$).

The conventional capacitive coaxial couplers use a thin cylindrical central conductor, without the additional conductor bead (shown in Fig. 5.6). In absence of the bead, the gap g_c has to be very small (of the order of 100 μm), and hence it is very sensitive to fabrication errors. An adapter with a thin probe will have narrower bandwidth (BW), and its transmission coefficients will vary within the dipole BW. To couple all power

induced over the BW of the dipole modes, the BW of the waveguide adapter should be wider than the BW of the cavity dipole modes. The transmission coefficient of the coupler should be constant over the BW of the dipole modes. In addition, the BW of the waveguide coupler is kept considerably wider than the cavity bandwidth to accommodate the intentional frequency separation between x and y position signals, and any frequency variation due to fabrication errors.

To overcome the limitations of the conventional adapter, an additional conductor bead was added at the end of the coaxial probe as shown in Fig. 5.6. The capacitive bead provides an additional capacitance, which makes it possible to increase the gap g_c between the probe and opposite waveguide wall. To study the transmission and reflection characteristics of the waveguide adapter, the S-parameters of the simulation model shown in Fig. 5.6 were solved using S3P. The major simulation parameters are listed in Table 5.5.

Table 5.5: Simulation parameters used for study of waveguide adapter

Parameter	Value	Unit
Solver package	S3P	
Average/Minimum mesh element length	2 / 0.2	mm
Mesh type	Tetrahedral with curved elements	
Frequency step size	50	MHz

The simulated transmission and reflection responses of the waveguide adapters with conductor beads of different radius's r_c are shown in Fig. 5.7(a) and 5.7(b). The gap g_c was kept constant at 3.6 mm. The geometry was solved using the S-parameter solver S3P. The code does not produce meaningful results below the waveguide cutoff frequency, and should be excluded from the analysis. Port-1 at the waveguide end was used as an input port. The simulation showed that the adapter bandwidth increases and its response becomes flatter with an increase in the bead radius. The bead of radius 5 mm is used in the final design. For the bead with 5 mm radius, the reflection at 6450 MHz (near dipole mode frequency) was -11.4 dB. The Minimum reflection of -17.8 dB occurred at 7150 MHz. The maximum radius of the bead was limited by its access into the waveguide, hence the bead with 6 mm radius could not be used even though it provided lower reflection at the dipole frequency. Though the bead radius

was limited to 5 mm, the coupler could be further optimised by changing the gap g_c .

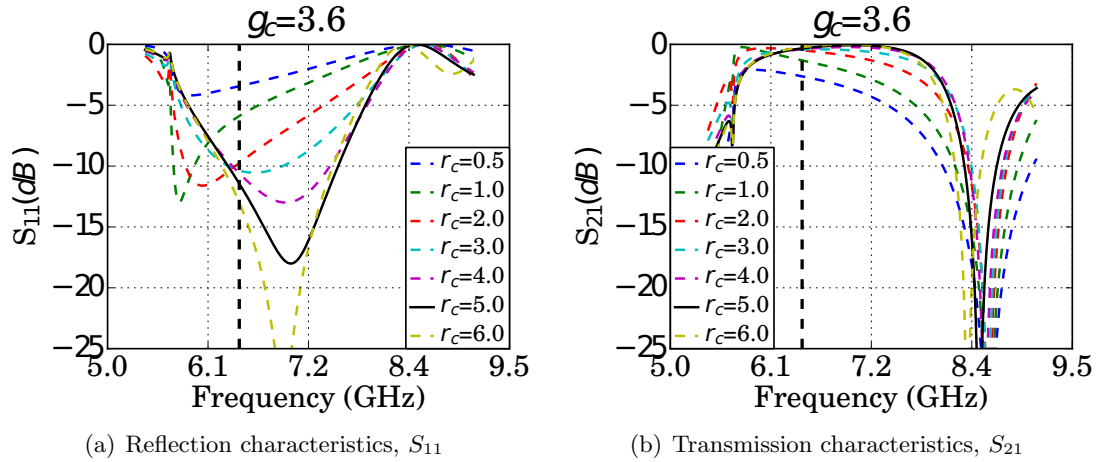


Figure 5.7: Simulated S-parameter responses of the waveguide adapters with coaxial beads of different radius r_c , at constant gap g_c

The simulated S-parameter responses of the adapter with different gap g_c are shown in Fig. 5.8(a) and 5.8(b). The adapter bandwidth increased with increase in g_c , while the transmission attenuation at dipole frequency reduced. The minimum reflection occurred for the gap of 4.6 mm. The simulation showed that, because of the additional conductor bead, it was possible to increase the gap and still achieve a wide bandwidth.

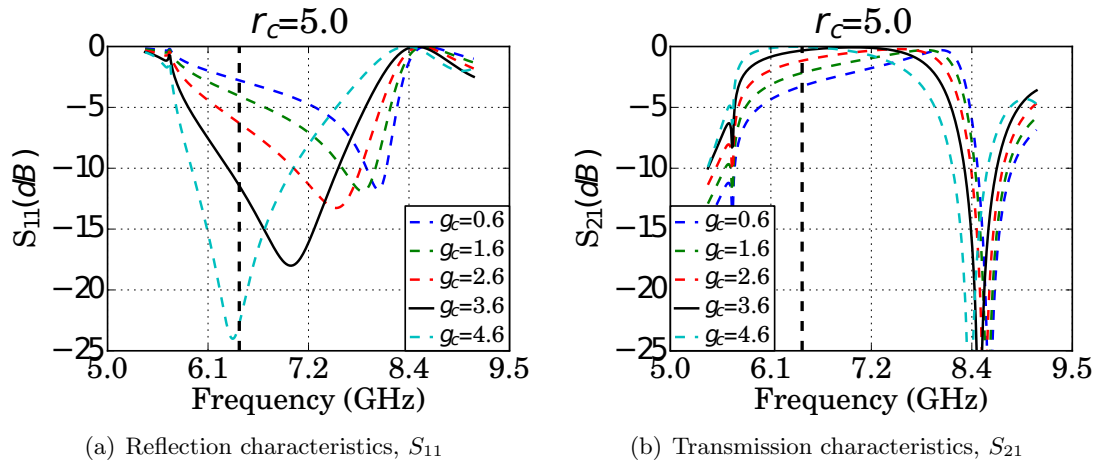


Figure 5.8: Simulated S-parameter responses of the waveguide adapters with different gap (g_c), for constant bead radius (r_c)

The waveguide adapter will be coupled to the cavity through a coupling slots at the waveguide surface assigned as a Port-1 in Fig 5.6. The surface will be enclosed and

will have a smaller opening in the form of a coupling slot. This modification changes the transmission and reflection characteristics. The final tuning of the gap (g_c) should be carried out while simulating the complete CBPM geometry. In the final design, a conductor bead of radius r_c of 5 μm was kept at gap g_c of 3.6 μm to reduce the effect of the fabrication errors and to minimise the rotation of the fields inside the cavity.

5.3.4 Deliberate orientation of dipole modes using asymmetric slots

The EM field induced in the dipole mode of the cavity is coupled to the waveguides through coupling slots (as shown in Fig. 5.9(a)). The slots are used because they provide better isolation between the x and y position measurement. The slots also provide better monopole rejection. The $x - y$ isolation increases with the ratio of the slot length to its width. The length of a slot is limited to the difference of the radius of the cavity and beam pipe, and it is kept at the maximum possible value. The minimum thickness of the slot is limited by the mechanical strength of the cavity material. In the final design the slots were designed to be 1.5 mm thick and 13 mm long.

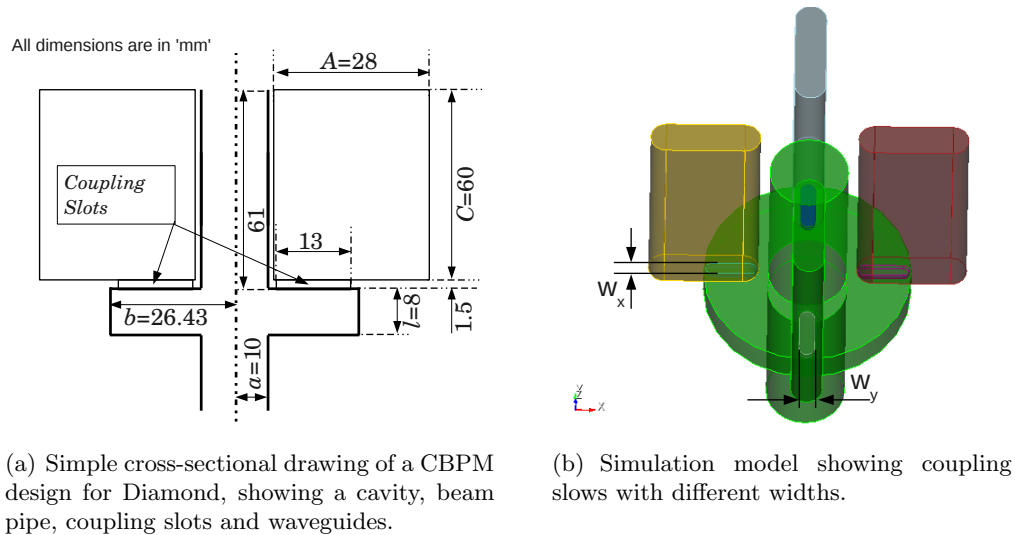


Figure 5.9: Simulation model to study effects of asymmetric coupling slots along x and y axes.

Because an ideal cylindrical cavity is a symmetric structure, the orientation of the induced dipole field is determined by the direction of the beam position offset. Even

a small error in fabrication of CBPM breaks the symmetry and it can disorient the modes which will no longer be aligned to the coupling slots or direction of the beam offset. The disoriented modes degrades the $x - y$ isolation and hence the measurement accuracy. As the cavity is planed to be built without any mechanical tuning system, it will not be possible to improve the isolation once it is fabricated. The isolation can be improved by deliberate orientation of the dipole modes to the coupling slots along x and y axes.

The orientation of the modes were fixed by breaking the symmetry of cylindrical cavity using slots of different widths W_x and W_y along x and y axes respectively. Using slots with different widths separates the dipole modes coupled to them and fixes their orientation parallel to the slots axes. The two dipole modes will resonate at different frequencies. As the modes are separated in frequency, the isolation can be further improved by attenuating the other dipole mode signal using filters of bandwidth lower than 5 MHz, in digital signal processing.

The minimum possible slot width is limited by the cavity material and output signal strength, as the power coupled into the waveguide decreases with a decrease in the slot width. The coupled power increases with the coupling slot width, but the $x - y$ isolation decreases, and the power coupled from the high frequency tail of the monopole increases.

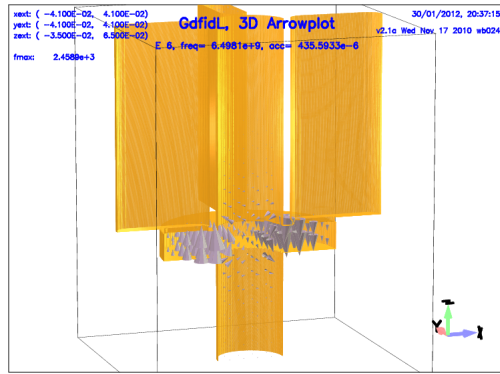
Fig. 5.9(b) shows a simulation model of the cavity and waveguides coupled to it through the slots. To examine the effects of asymmetric slots, the width W_y was changed while keeping the width W_x constant. The models were solved using Eigenmode solver of GdfidL to find their principle resonance modes. The important parameters of simulation

Table 5.6: Parameters of the simulation model to study mode separation

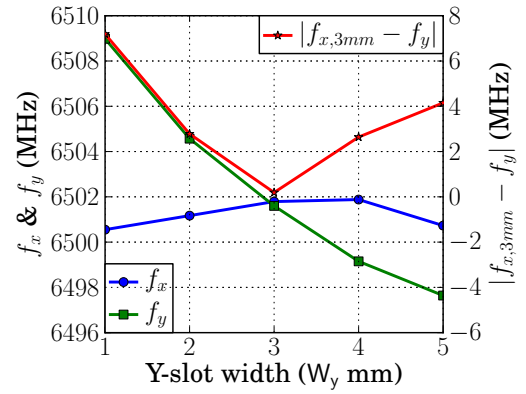
Parameter	Value	Unit
Solver package	GdfidL Eigenmode solver	
Average/Minimum mesh element length	0.2 / 0.02	mm
computation system	one quad-core node on cluster	
Simulation time	8.0	hours/ solution

models are listed in Table 5.6. GdfidL was used to compare the simulation results with the results presented in section 5.6.3.

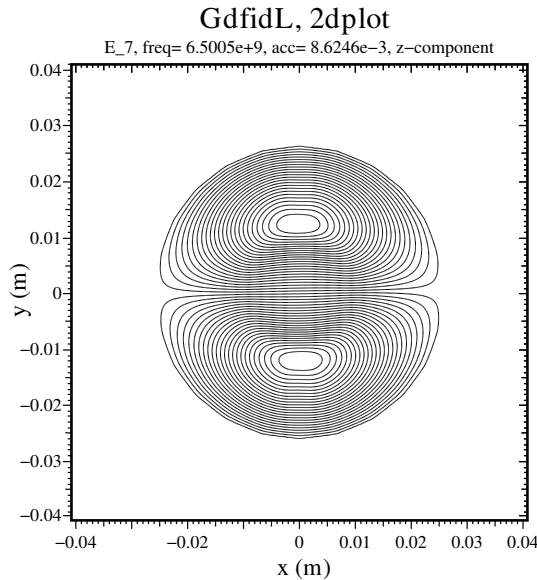
Fig. 5.10(a) shows the simulation model in GdfidL post processing software, and the electric field of the mode coupled through the slots along y -axis. The frequency separation between the two modes, introduced by different slot widths, are plotted in the



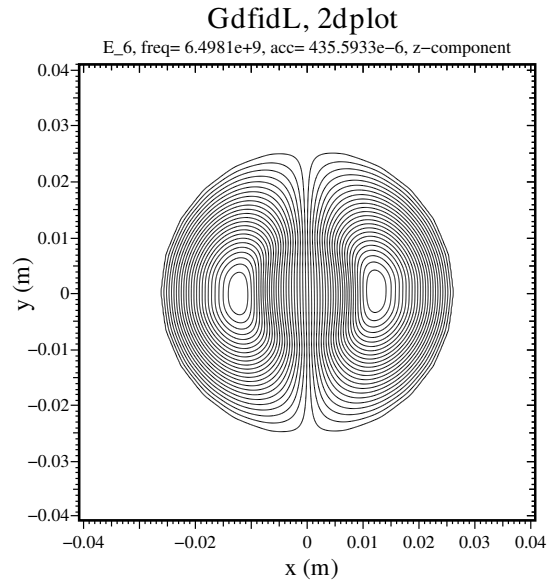
(a) Cavity model in GdfidL showing the electric field of the mode coupled to the slots along the y -axis.



(b) Frequency separation between two dipole modes for different slot widths W_y



(c) Equi-amplitude contours on the cavity central plane for the y -dipole mode coupled to the slots along x -axis



(d) Equi-amplitude contours on the cavity central plane for the x -dipole mode coupled to the slots along y -axis

Figure 5.10: Simulation results from the study of the separation of the dipole modes using asymmetric coupling slots along the x and y axes

Fig. 5.10(b). Simulations showed that with a change in width W_y , the resonant frequency f_y of the dipole mode coupled to the slots along the y -axis decreased, and vice versa. Along with f_y , the resonant frequency f_x of the dipole mode coupled to the slots along x -axis also changed with change in W_y . The change in f_x was smaller compared to the change in f_y .

Simulations showed that the modes were separated by 5 MHz by changing the slot width by 2 mm. The frequency change was not linear in W_y . For a lower slot width, the frequencies changed most, the slots would be more sensitive to fabrication errors and less power would be coupled to the waveguide.

The equi-amplitude contours for the axial component of the electric field \vec{E}_z of the two dipole modes, for a model with slot widths W_x and W_y of 3 and 4 mm, are plotted in Fig. 5.10(c) and 5.10(d) respectively. The two dipole modes were separated from each other in frequency and were aligned to the slots. All plots in Fig. 5.10 confirm the hypothesis that the dipole modes are deliberately pre-oriented to the slots and separated in frequency. As the frequency separation will be affected by the addition of the coaxial couplers, and the boundary conditions used at the waveguide ends, the final design parameter optimisation should be done on the complete geometry model.

5.3.5 Simulation of complete cavity BPM geometry

After the above detailed studies, a complete geometry model of the CBPM was created for final EM simulations. Fig. 5.11 shows the simulation model geometry created using Cubit. Based on the study of mode separation, the waveguides along the x and y axes were coupled to the cavity through 4 and 3 mm wide slots respectively. As shown in Fig. 5.11(b), the port numbers are assigned in a counter clock wise direction, starting with Port-1 assigned to the waveguide adapter coupled through the narrower slot along the y -axis.

To find the optimum mesh setting, the geometry was meshed using Cubit with different mesh densities, and was solved using Omega3P. Fig. 5.12 shows the resonant frequency and Q_0 of a dipole mode for solution with different mesh densities. For all mesh densities

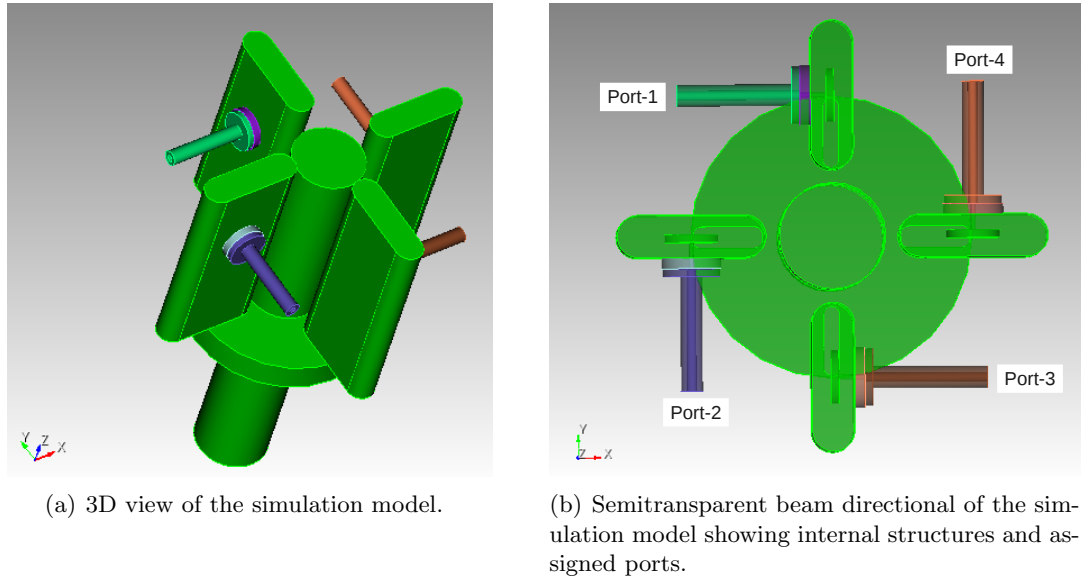
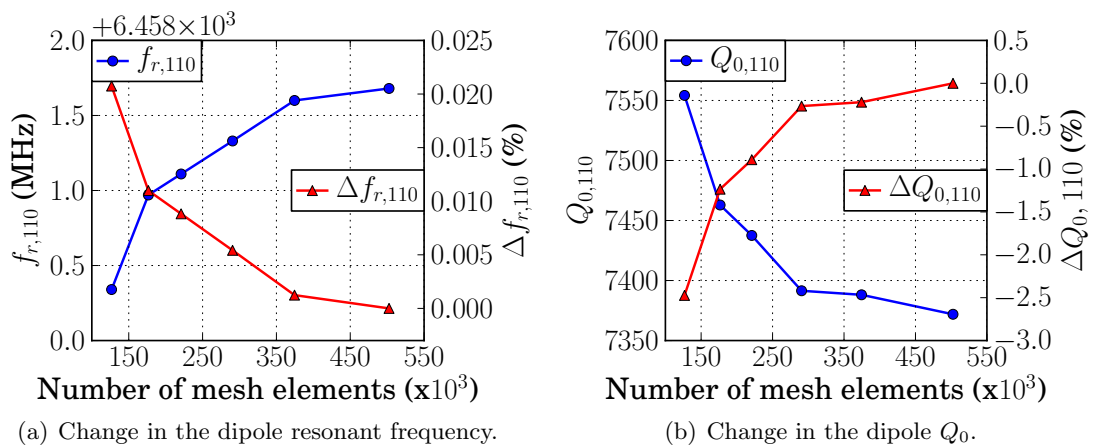


Figure 5.11: Simulation model of complete CBPM geometry.

tested, the simulation results were stable. Because curved mesh elements were used, the geometry was defined accurately even with a coarse mesh. The variation in the dipole frequency and Q_0 were less than 1.6 MHz and 200 respectively, which are 0.025% and 2.5% of their values calculated at the highest mesh density. The variation in simulation results were negligible above 450000 mesh elements. The same mesh has been used for Eigenmode, S-parameter and time domain solutions.

Figure 5.12: Cavity dipole frequency and Q_0 as function of number of mesh elements.

Electric fields of the four lowest frequency resonant modes, derived from the Eigenmode simulation using Omega3P are plotted in Fig. 5.13. The dipole mode, which is coupled out through the waveguides along the x -axis, measures the beam position offset along the y -axis, and while the dipole mode coupled out through the waveguides along the y -axis measures the position along x -axis.

Table 5.7 lists the results from the Eigenmode simulations. The resonant frequencies of the lowest frequency resonant modes were reduced by the addition of the waveguide adapters. As expected, the R/Q_0 of the monopole and dipole did not change considerably by insertion of the slots and waveguide coupler. The R/Q_0 values were calculated

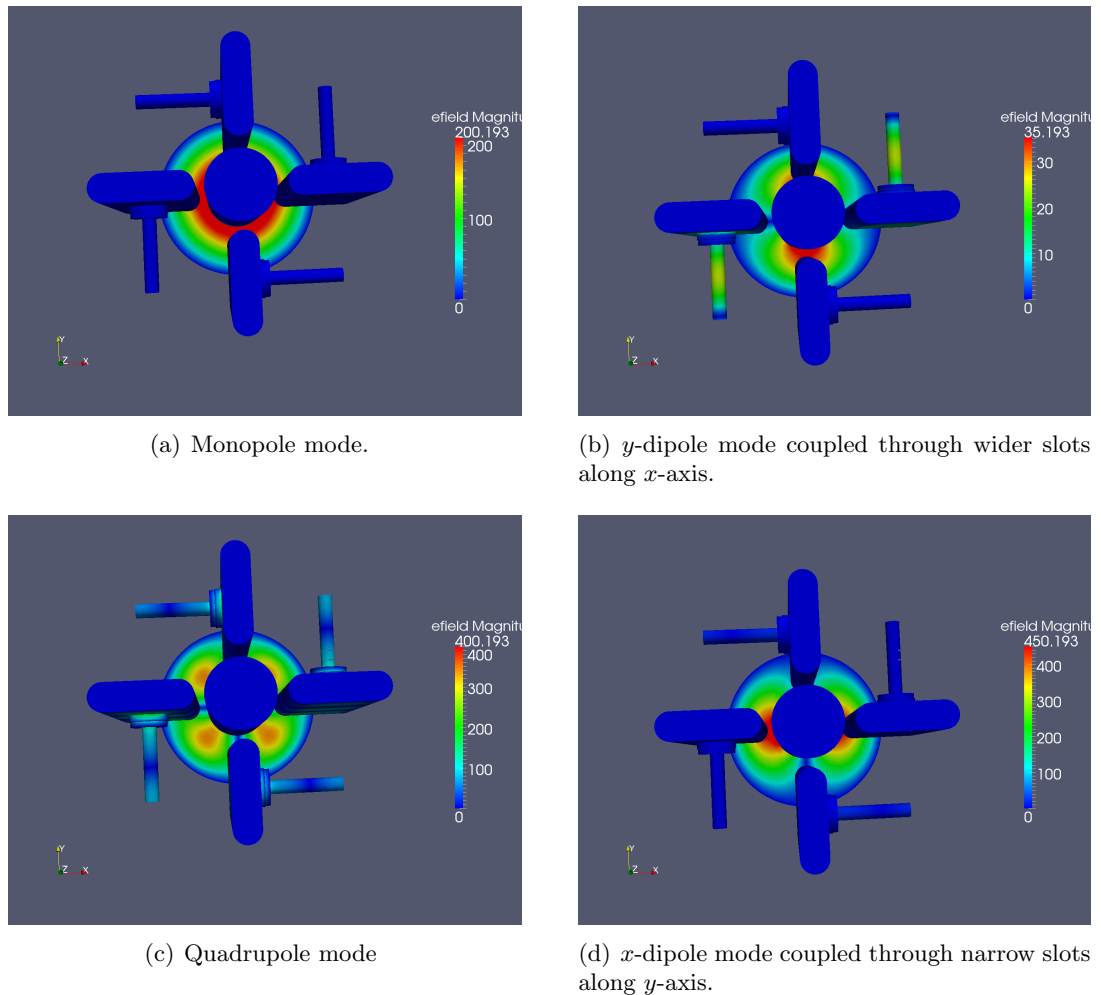


Figure 5.13: Field orientation of the lowest four frequency resonant modes derived from the Eigenmode simulations of complete CBPM model.

using ACDTool for bunch position offsets of 1 mm in x and y axes.

Table 5.7: Results of the Eigenmode simulations of the complete CBPM model, using Omega3P.

Mode (Bunch position offset for R/Q_0)	Simulation output				Calculated from simulation		
	f_r (GHz)	Q_0	Q_{ext}	$\left(\frac{R}{Q_0}\right)$ (Ω)	Q_L	τ_d (ns)	Voltage attenuation after $2\mu s$
Monopole	4.6985	6323	6.83×10^{12}	71.98	6322	428.2	9.37×10^{-3}
y -dipole (1 mm along y -axis)	6.4552	7487	5117	0.818	3039	149.8	1.59×10^{-6}
x -dipole (1 mm along x -axis)	6.4596	7535	7388	0.825	3730	183.8	1.88×10^{-5}
Quadrupole (1 mm at 45° to x -axis)	8.7615	10148	1.27×10^6	0.0017	10067	365.7	4.21×10^{-1}

The Q_0 of the modes were in agreement with the theory and previous simulation results of Table 5.4. The higher value of the external quality factor Q_{ext} for the monopole mode verified that it did not couple into the waveguides, but it decayed through resistive heating in the cavity walls. Lower value of Q_{ext} for the y -dipole mode than x -dipole mode verified that more power was coupled through the wider slot along the x -axis than the narrow slots along the y -axis. With higher Q_{ext} , the quadrupole was weakly coupled out through the waveguide compared to the dipole modes.

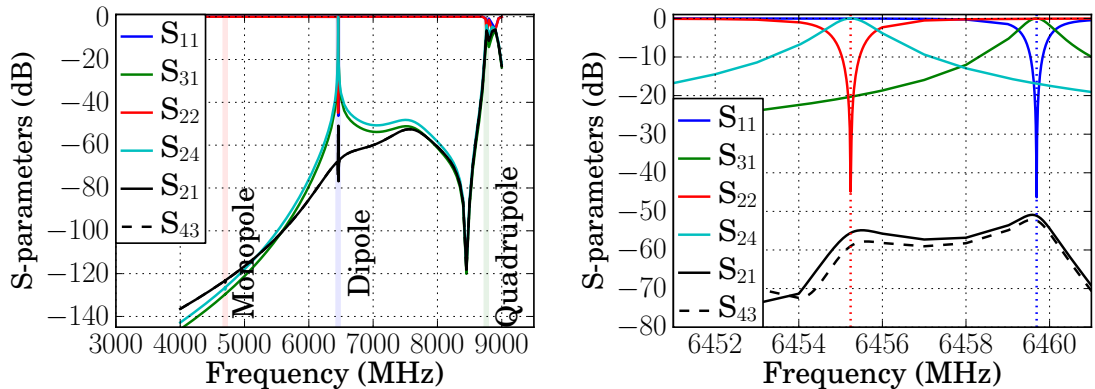
From the simulated Q_0 and Q_{ext} , the loaded quality factors Q_L and field amplitude decay constants τ were calculated using equations 2.8 and 2.6. For a bunch separation of $2 \mu s$, the field amplitudes of the two dipole voltages will have decayed by -115 and -94 dB by the time the next bunch arrives.

The S-parameters of the complete BPM model were simulated using S3P. Fig. 5.14(a) shows the S-parameter simulation results over a frequency range covering monopole to

quadrupole modes. S-parameters were first simulated with a coarser frequency resolution of 100-MHz. The frequency regions of the individual modes were simulated with a finer frequency resolution of 10 kHz. A typical total simulation time to solve 100 frequency steps using 120 CPUs on the Hopper super computer was 1 hour (120 CPU hours). Because it is easier to interpret, the S-parameter are plotted in the decibel magnitude format, which can be calculated as,

$$S(dB) = 20 \times \log_{10} (|S_{\text{complex}}|), \quad (5.7)$$

where S_{complex} is the S-parameter value received from the simulation in a form of a complex vector. As expected, the monopole was attenuated by more than -120 dB at 4698 MHz. The quadrupole was coupled better than -3 dB at 8762 MHz. Compared to the dipole mode, the quadrupole mode is poorly coupled to the beam, and it will be attenuated by the RF and digital filters.



(a) S-parameters in frequency range from the monopole to quadrupole modes.

(b) Zoomed to the frequency region of the dipole modes.

Figure 5.14: Results of S-parameter simulations of a complete CBPM geometry using S3P.

The S-parameters within a frequency range of the dipole modes are shown in Fig. 5.14(b). As listed in Table 5.8, the peaks of the reflection and transmission characteristics for the two dipole modes were at 6455.2 and 6459.6 MHz, which agreed with the values from the Eigenmode simulations. As shown by the traces of S_{11} and S_{22} , the reflection for the both dipole modes were less than -45 dB. From the S_{31} and S_{42} traces, the transmission loss between the coupled ports was less than -0.0002 dB. From the

transmission traces, the bandwidth of the modes were calculated as the difference of the frequencies on both sides of the peaks at which the S-parameter magnitude is half of the peak magnitude (3 dB point). The 3 dB bandwidth Δf_{3dB} , derived from the S_{31} and S_{24} , were 0.86 and 1.2 MHz respectively. Using the peak frequencies f_r and BWs from the S-parameter curves, the loaded quality factors for the modes were calculated using the following equation [19],

$$Q_L = \frac{f_r}{\Delta f_{3dB}}. \quad (5.8)$$

Table 5.8: Results of S-parameter simulations of the complete CBPM model.

Parameters	Dipole Region				
	Peak frequency f_r (MHz)	Peak magnitude (dB)	Bandwidth Δf_{3dB} (MHz)	Q_L	τ_{volt} (ns)
Reflection					
S_{11}	6459.6	-46.3	–	–	–
S_{22}	6455.2	-44.8	–	–	–
Transmission					
S_{31}	6459.6	-0.00015	0.86	7511	370
S_{42}	6455.2	-0.00015	1.26	5123	253
Cross coupling					
S_{21}	6455.2 & 6459.6	-55.6 & -51.1	–	–	–
S_{43}	6455.2 & 6459.6	-59.0 & -52.4	–	–	–

As tabulated, the loaded quality factor Q_L for the dipole modes were 7511 and 5123. The Q_L derived from the S-parameter simulations were larger than the same derived from the Eigenmode simulations, and hence should be verified using time domain simulation. As the same geometry mesh file, material properties, boundary conditions and ports were used in the both (the Eigenmode and S-parameter) simulations, the reason for the difference in the Q_L values was not clear. The $x - y$ isolation was derived as a difference between a transmission and cross coupling traces. The $x - y$ isolation was better than -50 dB at the frequencies of both dipole modes.

As the resonant frequencies are verified from two different solvers, the major parameter remaining to check is the beam coupling. To verify it, propagation of a bunch through the CBPM model was simulated using T3P. The major parameters used in the simulation are listed in Table 5.9. As the prototype cavity was planned to be tested at the ATF2, the typical bunch parameters for the ATF were used in the simulation. To simulate the passage of an 8 mm long bunch, the mesh element along the bunch trajectory should be shorter than 2 mm. A total bunch length of $4\sigma_b$ was used to avoid any spurious excitation of high frequency modes due to sharp bunch edges. To reduce the simulation time, the model was simulated using a first order mesh setting.

Table 5.9: Parameters used for the time domain simulation of the complete CBPM geometry.

Bunch Parameters		Other parameters	
Parameters	Values	Parameters	Values
Bunch length σ_b	8 mm	Maximum element along bunch trajectory	1 mm
Total number of σ_b	4	Time step length	6 ps
Bunch charge	1.6 nC	Number of CPUs used	120
Bunch offset	1 mm in y	Total CPU time	6 ($\times 120$) hours

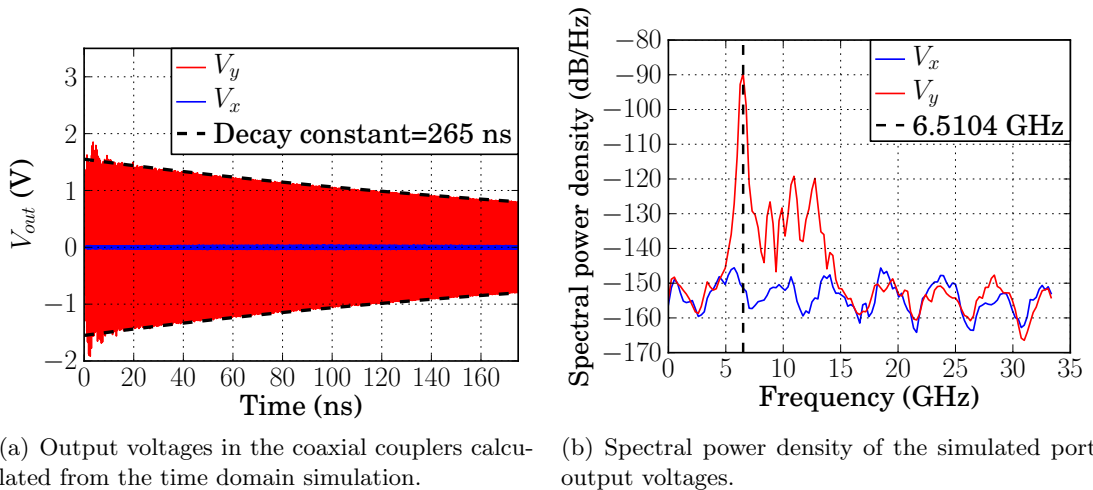
A single bunch was passed through the cavity along a linear trajectory parallel to the cavity (z) axis, at 1 mm offset in the y -axis. To derive the coupled voltages at the ports, the electric and magnetic field components were monitored at specific points near ports inside the coaxial couplers. The positions of the point monitors were chosen such that the coaxial radius vectors passing through them were parallel to the x or y -axis. At these locations, only one axial component of the electric field, \vec{E}_x or \vec{E}_y , would be dominant, which simplified their interpretation. The corresponding coaxial output voltage V_{coax} across a matched load resistance can be calculated from the monitored electric field using [19],

$$V_{\text{coax}} = |\vec{E}_\rho| \rho \ln \left(\frac{r_{\text{shield}}}{r_{\text{probe}}} \right), \quad (5.9)$$

where ρ is the radial distance of the point monitor in the coaxial coupler, $|\vec{E}_\rho|$ is the electric field magnitude at the monitor position, r_{shield} and r_{probe} are the radius of the

outer and inner conductors of the coaxial coupler respectively.

Fig. 5.15 shows the voltages V_y and V_x , calculated using the above equation, coupled into the coaxial couplers along the x and y axes respectively. As the bunch position was offset in the y -axis, the bunch energy should couple to the y -dipole mode (Fig. 5.13(b)), which is coupled out through the waveguides along the x -axis into Port-2 and Port-4. The amplitude of the output voltage V_y at the beginning of the signal in Port-2 was 1.5 V. An exponential decay function was fitted to the amplitude of the port voltage. The voltage amplitude decayed to 0.367 times its initial maximum value after 265 ns, which agreed well with the decay time (τ_{volt} in Table 5.8) calculated from the S-parameter simulation.



(a) Output voltages in the coaxial couplers calculated from the time domain simulation.

(b) Spectral power density of the simulated port output voltages.

Figure 5.15: Results from time domain simulation of a complete CBPM geometry using T3P.

The cavity output voltage can be analytically predicted using Eqn. 2.18, where the Q_{ext} values mentioned in the Table 5.7 can be used. A single bunch of 8 mm length and 1.6 nC charge, when passed at 1 mm position offset, should induce y -position peak signal amplitude (V_y) of 1.3 V. The prediction using Q_{ext} agreed well to the port voltage calculated from the time domain simulation.

The value of Q_L calculated from the Eigenmode simulation is lower compared to the same from the S-parameter simulation. As the time domain simulation agreed with the S-parameter simulation, the amplitude of the extracted voltage should be lower than

the one calculated using the Q_{ext} from the Eigenmode simulation.

The peak amplitude voltage V_x of the signal coupled into Port-1 was 0.04 V. The spectral power density (SPD) of x and y signals are shown in Fig. 5.15(b). The frequency resolution of the SPD plot was 0.2 GHz, which was limited by the total number of simulation time samples. The power coupled into Port-2 was approximately 60 dB higher than the power coupled into Port-1. The isolation from the time domain simulation agreed well with the 55 dB isolation calculated from the S-parameter simulation.

5.4 Fabrication

The fabrication process was monitored by our collaborators at the Diamond Light Source. Each cavity BPM was fabricated in four major sections, which were then brought together. All the cavities were fabricated by FMB (Feinwerk- und Meßtechnik), Berlin, Germany. One of the four fabricated cavities is shown in the Fig. 5.16. To minimise the fabrication errors due to brazing, the cavity, waveguides and coupling slots were machined as a single section. The open ends of the cavity and waveguide

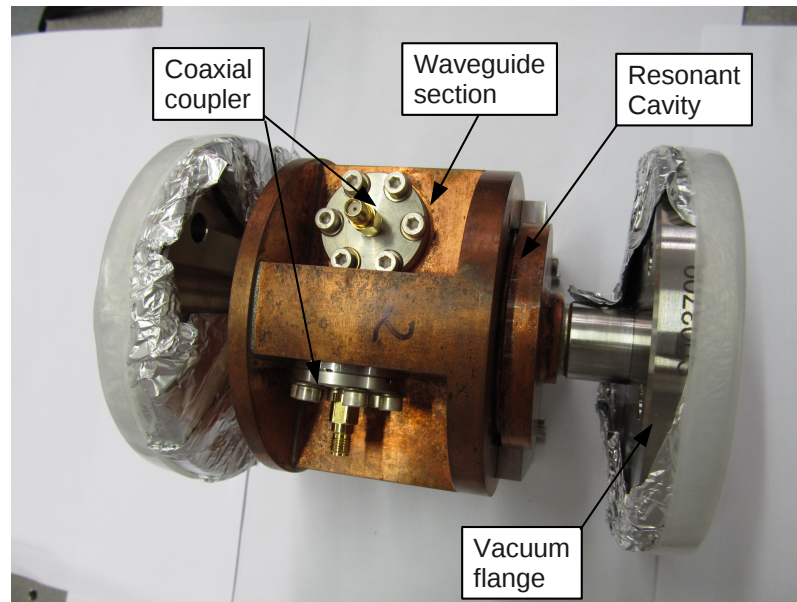


Figure 5.16: One of the four fabricated cavity BPMs for the Diamond Light Source.

were enclosed by brazing metal caps to them. Both ends of the beam pipe were then brazed to standard DN63-CF vacuum flanges. The coaxial couplers were fitted after brazing all of the sections.

The cavity will be attached to the other accelerator components through vacuum flanges. For accurate orientation of the cavity with support structure, reference holes were drilled on cavity structure where the support can be fixed.

5.5 Benchtop RF measurements

After fabrication, the RF characteristics of all cavities were measured at the Diamond Light Source. One of the four cavities was further studied in details through RF measurements at Royal Holloway. Presented in this section are the various measurements performed to determine the reflection and transmission characteristics, Q values, and orientation of the modes.

5.5.1 Test instruments

A vector network analyzer (VNA) from Rohde & Schwarz, model number RS-ZVB20 [70], has four ports for simultaneous measurement of the S-parameters. The measurements can be performed from 10 MHz to 20 GHz, with frequency resolution of 1 Hz. The typical dynamic range is 110 dB in the frequency region of interest. The typical amplitude and phase accuracy is better than 1 dB and 6° respectively. An automatic calibration kit based on the short and open technique was available for the model. It can be operated manually, or remotely through GPIB or LAN.

A precision mover system from Thorlabs was used to scan the position of a dielectric bead, during mode orientation measurements. It can move in two axes in range of 10 cm, with position accuracy of $1.6\ \mu\text{m}$. It has load capacity of 12 kg and can be moved with maximum speed of 3 mm/s, to which it can accelerate at maximum rate of $4.5\ \text{mm/s}^2$.

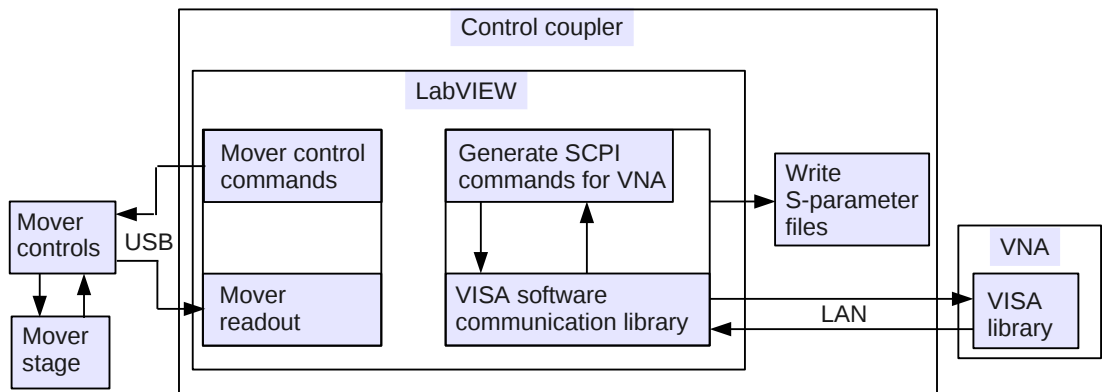


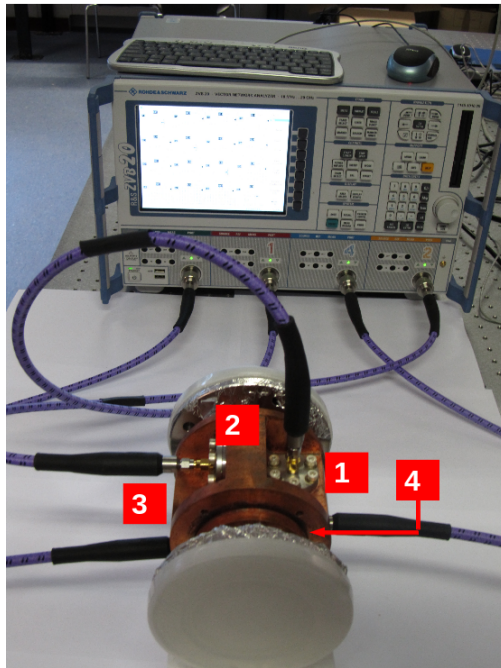
Figure 5.17: Block diagram of remote hardware control scheme for RF measurements.

Fig. 5.17 shows a block diagram explaining the scheme for the communication, control and synchronisation between various test instruments. LabVIEW was used to synchronise and sequence individual processes [71]. The VNA was controlled using SCPI commands, issued through VISA communication library over LAN. The mover control commands and readouts were executed through USB.

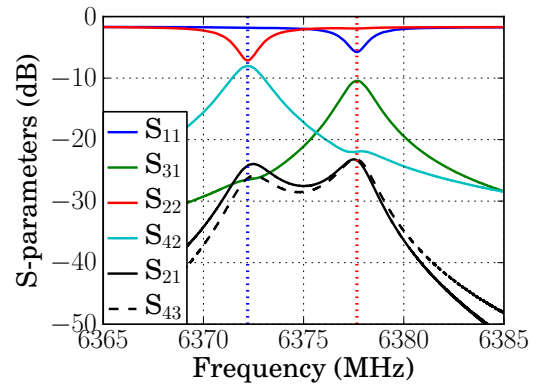
5.5.2 S-parameter measurements

Before starting the RF measurements for the CBPM, the VNA was first calibrated using the calibration kit, to measure the intrinsic losses of the instrument and connections. The calibration kit was then replaced with the device under test (DUT), which is a cavity BPM in this case.

The experimental setup to measure the transmission and reflection characteristics of the CBPM is shown in Fig. 5.18. All four ports of the BPM were connected to the individual ports of VNA as noted in the Fig. 5.18(a). All of the 16 complex S-parameters were recorded during a single frequency sweep. At first, the S-parameters were measured over a wide frequency bandwidth, spanning from the monopole frequency to quadrupole frequency. All 16 traces were exported to an ASCII data file. The exported data was processed and plotted using SciPy.



(a) Experimental setup.



(b) Measured S-parameters of the cavity under test.

Figure 5.18: Experimental setup to measure the S-parameters of a CBPM, and measurement results.

The S-parameter magnitudes derived within the dipole frequency region are plotted in Fig. 5.18(b). The frequency span of 20 MHz was traced with frequency resolution of 2 kHz for accurate post processing. The peak frequencies $f_{p,exp}$ and magnitudes $S_{p,exp}$ of the S-parameter traces calculated from the experimental measurements are tabulated in Table 5.10, along with their difference from the values, $f_{p,simu}$ and $S_{p,simu}$, calculated from the S-parameter simulation results, listed in Table 5.8. Two dipole modes had the resonant frequencies of 6372.2 and 6377.7 MHz, which are lower by more than 81 MHz from the simulation results. The dipoles were separated by 5.5 MHz, which is a wider separation than what was predicted by simulations. The peaks of the reflection curves had magnitude between -5.5 to -8.5 dB, which are at least 36 dB higher than the simulated results. The higher reflection values means that the dipole frequency signals transmitted from the ports, towards the cavity, were reflected 4000 times more than that found in the simulations, and the coupling was weaker than the predicted value.

From the transmission traces S_{31} and S_{42} , the signals received at the coupled port were

attenuated by 10.3 and 8.0 dB respectively. The transmission losses were much higher than those expected from the S-parameter simulations, which means that the fields induced in the cavity by a bunch will be attenuated more when extracted out into the coaxial lines. The $x - y$ isolation, calculated as the difference between the magnitudes of S_{31} and S_{21} traces at the peak frequency of S_{31} trace, was equal to -13 dB. The isolation was poorer compared to the simulated isolation of -55 dB.

As the monopole frequency was below the cutoff frequency of the waveguide, the monopole was not visible and it was below the noise level, with amplitude attenuation higher than -150 dB. No apparent peak could be identified in the expected monopole frequency region. The quadrupole was coupled with transmission loss less than -4 dB.

One of the possible reasons for the poor transmission and isolation values for dipole

Table 5.10: Results of S-parameter measurements.

Param- eters	Measured		Simulated - Measured	
	Peak frequency $f_{p,exp}$ (MHz)	Peak magnitude $S_{p,exp}$ (dB)	Peak frequency $f_{p,simu} - f_{p,exp}$ (MHz)	Peak magnitude $S_{p,simu} - S_{p,exp}$ (dB)
Reflection				
S_{11}	6377.6	-5.8	82.0	-40.5
S_{33}	6377.7	-6.5	81.9	-39.8
S_{22}	6372.2	-7.1	83.0	-37.6
S_{44}	6372.2	-8.3	83.0	-36.5
Transmission				
S_{31}	6377.7	-10.3	81.9	+10.3
S_{42}	6372.2	-8.0	83.0	+ 8.0
Cross coupling (at peak frequencies of S_{31} and S_{42} traces)				
S_{21}	6377.7 & 6372.2	-23.4 & -24.2	81.9 & 83.0	-32.2 & -26.9
S_{43}	6377.7 & 6372.2	-23.2 & -26.2	81.9 & 83.0	-35.8 & -26.2

modes could be the disorientation of the modes due to fabrication errors. For better understanding of cavity performance, the orientation of the modes were studied.

5.5.3 Calculation of Q-values using impedance method

The Q -values of a cavity can be calculated using different methods [19, 72]. The loaded quality factor Q_L can be calculated from a transmission curve using Eqn. 5.8. The Q_0 and Q_{ext} can be determined using an impedance method explained by Ginzton [72]. To apply this method the impedance of the waveguide coupler should be relatively constant within the bandwidth of the mode. The impedance method can be explained using a cavity equivalent circuit. Fig. 5.19 shows a cavity equivalent circuit reduced to a single port connection. The source inside the VNA connected to a port of the cavity can be represented by the source V_s on the circuit. The internal impedance of source and VNA port together is represented by Z_0 . The coupling between the waveguide and coaxial coupler is represented by an equivalent complex mutual coupling coefficient M between the inductor of the cavity L and waveguide coupler L_1 . The resonant cavity is represented by the LCR circuit, where the L , R and C are the equivalent inductance, resistance and capacitance respectively. The loading effects from the remaining ports are also accounted in the values of L , R and C for the cavity.

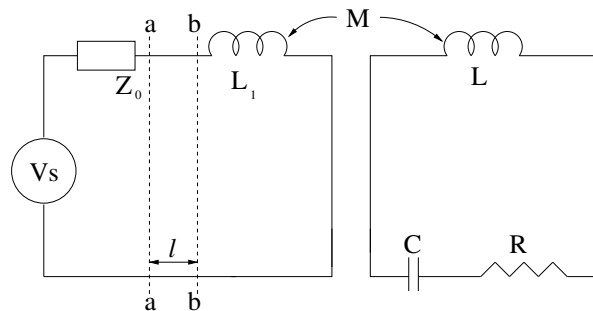


Figure 5.19: Cavity equivalent circuit reduced to a single port connection.

The effective impedance at the VNA output (line aa) can be reduced to the form written as [72],

$$\frac{Z_{aa}}{Z_0} = j \frac{X_1}{Z_0} + \frac{(\omega M)^2}{R + j(\omega L + 1/\omega C)}, \quad (5.10)$$

where $X_1 = \omega L_1$ is the series reactance of the coupler. The equivalent complex reflection

coefficient is calculated as,

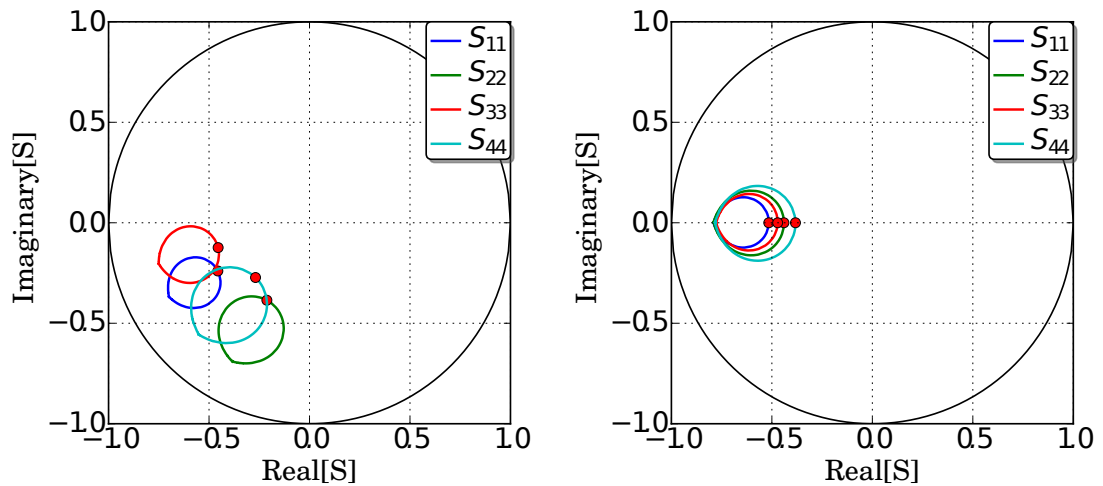
$$\Gamma_{aa} = \frac{Z_{aa}/Z_0 - 1}{Z_{aa}/Z_0 + 1}. \quad (5.11)$$

The complex reflection traces from the S-parameter measurements are plotted in Fig. 5.20(a).

The points corresponding to the resonant frequency peaks are highlighted as red circles.

The Q values can be determined from these plots after two processing steps:

1. Rotation of the curves to put the resonance peak points on the real S axis;
2. Shifting of the curves along the real S axis such that the Q_L calculated from the impedance method matches the Q_L determined from the transmission curves.



(a) Reflection S-parameter traces measured at four ports.

(b) Traces rotated around the origin.

Figure 5.20: Rotation of the S-parameter traces during calculation of Q values using impedance method. Red circles represent the peak (resonant frequency) points on the S-parameter traces. The black circle represents $R=0$ circle.

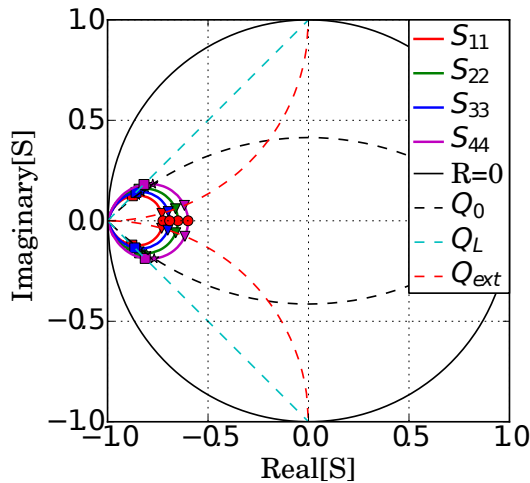
At the resonant frequency, the cavity equivalent impedance has a real value and the peak point should lie on the real S axis of the vector S-parameter chart. The plots are rotated due to the additional phase introduced within the couplers and transmission lines. To compensate the phase difference, the traces are rotated around the center such that the peak points fall on the real S axis of the plot. It is equivalent to inserting

or removing a lossless transmission line, which will change only the phase of the signal. The rotated smith charts are plotted in the Fig. 5.20(b).

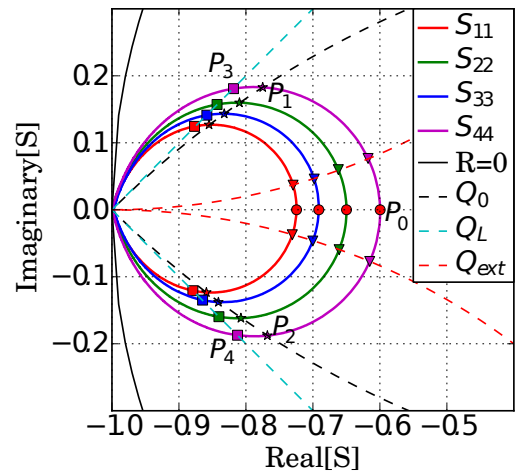
If there are no losses within the waveguide coupler, the point diametrically opposite the peak frequency should lie on the $R = 0$ circle. The waveguide couplers have inherent losses which should be taken into account when shifting the traces. The losses in the waveguides are already considered when calculating Q_L from the transmission traces. Fig. 5.21(a) and 5.21(b) shows the rotated reflection traces shifted along the real S axes. The quality factors Q_0 , Q_L and Q_{ext} can be calculated using the intersections points between the S-parameter traces and the curves labelled as Q_0 , Q_L and Q_{ext} respectively [72]. For example, the Q_L from S_{44} trace can be calculated using [72],

$$Q_L = \frac{f(P_0)}{|f(P_4) - f(P_3)|}, \quad (5.12)$$

where $f(P_0)$ is the resonant peak frequency, $f(P_4)$ and $f(P_3)$ are the frequencies for points at the intersection between the S_{44} trace and Q_L lines. The traces are shifted along the real S axes such that the Q_L calculated using the above equation matches the Q_L calculated from the transmission traces. Determination of Q_L is an iterative



(a) Traces shifted along real S axes



(b) Enlarged plot, showing intersection points used to calculate the Q values

Figure 5.21: Traces shifted to match calculated Q_L values to those from the transmission curves

process. Each locus is moved individually. Moving the locus outward, towards $R = 0$ circle, increases the Q_L and vice versa. Similar to the Q_L , the values of Q_0 and Q_{ext} are calculated from the frequencies of the intersection points with the traces labeled as Q_0 and Q_{ext} . The curves Q_0 are circles with radius $\sqrt{2}$ and centers at points (0,-1) and (0,1). The curves Q_{ext} are circles with radius 1 and their centers at (-1,-1) and (-1,1).

The Q values calculated using impedance method, for all four reflection ports are listed in Table. 5.11. As expected the Q_{ext} for the S_{22} and S_{44} are lower than those for S_{11} and S_{33} , because more power is coupled through the wider slots. The derived Q_0 value for a port (for example for Port-1 from S_{11}) include the loading effect from the other coupled port (Port-3 from S_{33}). The actual internal quality factor ($Q_{0,absolute}$) can be derived by removing the contribution from the coupled port as,

$$Q_{0,absolute} = \frac{Q_0 Q_{ext,coupled}}{Q_{ext,coupled} - Q_0}, \quad (5.13)$$

where $Q_{ext,coupled}$ is the Q_{ext} value derived for the coupled port.

Table 5.11: Q values calculated using impedance method.

Trace	Peak frequency (MHz)	Transmission method $Q_{L,31}$ & $Q_{L,42}$	Impedance method			
			Q_L	Q_0	Q_{ext}	$Q_{0,absolute}$
S_{11}	6377.6	$Q_{L,31} = 3727$	3729	4274	26794	5193
S_{33}	6377.7		3729	4355	24155	5201
S_{22}	6372.2	$Q_{L,42} = 3096$	3096	3704	17408	4901
S_{44}	6372.2		3096	3729	15170	4849

These Q values can be used to predict the cavity output signal for the given bunch parameters, using Eqn. 2.18. The Q_L values will be verified from the decay time of the cavity signal during beam testing. The Q_{ext} can be verified during beam testing, if the bunch charge and length are known from other diagnostics; and if the position offset at the location of the CBPM can be predicted using correlation or beam optics relation with the positions measured by other CBPMs.

5.5.4 Field orientation measurements.

If the dipole fields are disoriented from the slots, a bunch with position offset along x -axis will induce voltage into the dipole mode corresponding to y position signal, which reduces the $x - y$ isolation. With proper field orientation measurements, the comparison between the S-parameters, field orientation and beam measurement should give a clearer picture of the relation between cavity parameters and its performance as a BPM.

The field orientations of the dipole and quadrupole modes are measured using bead-pull perturbation technique [19, 72]. The EM field of a resonant cavity is perturbed by inserting a small low loss dielectric bead inside the cavity. The perturbation will change the resonant frequency, amplitude and phase of the field. The amount of change in the field parameters are proportional to the volume and dielectric properties of the bead material, as well as the strength of the EM field at the position of the bead. For a same bead at different positions, the amount of perturbation is only dependent on the field strength at the bead position. From one or more characteristics of the measured S-parameters, it is possible to determine the relative or absolute amplitude of the EM field component at the bead position. The relative change in the resonant frequency of a mode due to the bead $\frac{\Delta f}{f}$ can be calculated as [19],

$$\frac{\Delta f}{f} = -\frac{\int_{\Delta V} (\mu_r \mu_0 H^2 - \epsilon_r \epsilon_0 E^2) dV}{\int_V (\mu_0 H^2 - \epsilon_0 E^2) dV}, \quad (5.14)$$

where f is the resonant frequency of the mode, μ_r and ϵ_r are the relative permeability and permittivity of the bead material, μ_0 and ϵ_0 are the permeability and permittivity of free space, E and H are the electric and magnetic field strength at the bead position, ΔV and V are the volumes of the bead and cavity respectively. For a cavity with high Q , the change in the phase $\Delta\phi$ is related to the change in the resonant frequency by,

$$\Delta\phi = \tan^{-1} \left(2Q \frac{\Delta f}{f} \right) \approx 2Q \frac{\Delta f}{f}. \quad (5.15)$$

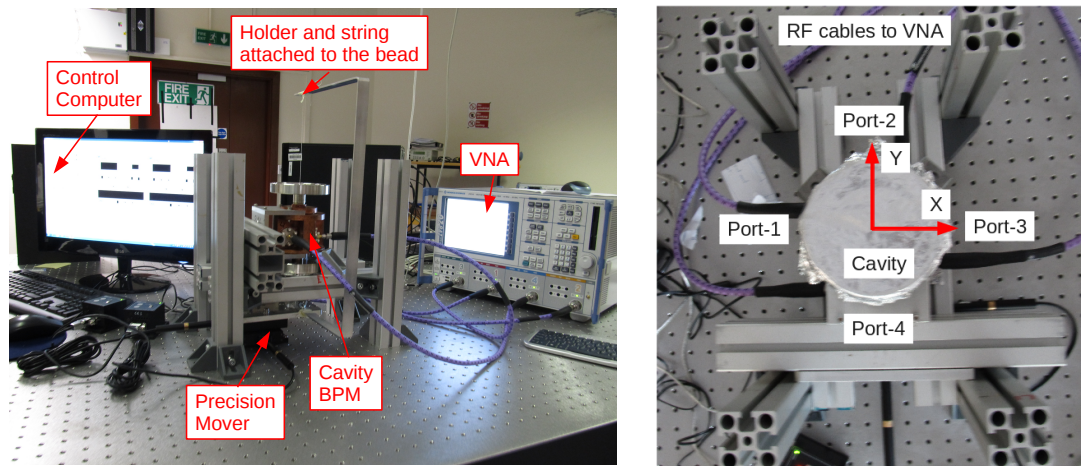
Considering that the change in the electric field within the bead cross-section is very small, the electric field strength at the bead position E_{\perp} be related to the measured

phase change by,

$$\frac{E_{\perp}}{U} \simeq \frac{\Delta\phi}{2Q} \frac{1}{\pi r^2 h}, \quad (5.16)$$

where U is the energy stored inside the cavity, r and h are the radius and height of the cylindrical bead respectively. For a cavity with relatively higher Q value, the change in the phase is $2Q$ times higher than the change in the resonant frequency. The change in the peak frequency and amplitude from a small plastic bead is difficult to detect compared to the phase change. The use of the phase is limited to the measurements with a small bead of low dielectric constant, due to the phase wrapping.

The experimental setup for bead-pull measurement is shown in Fig. 5.22. A cylindrical bead of plastic was attached to a thin string. The cylindrical bead was used to maximise the perturbation due to the axial dipole electric field. Plastic was used as a bead material to minimise any explicit interaction with the magnetic field. Both ends of the string were attached to a rigid holder, which was placed on the precision mover stage. The cavity was kept vertically static, while the holder and bead position was scanned in the xy -plane. The bead was installed in the vertical direction to reduce the position error due to the gravitational pull and vibrations. All four ports of the cavity were connected to the VNA. The port connections in reference to the mover axis are shown



(a) Experimental setup showing a control computer, bead installation, precision mover and VNA.

(b) Top view of cavity installation showing orientation of the ports with reference to the precision mover axis.

Figure 5.22: Experimental setup for field orientation measurements.

in the Fig. 5.22(b).

As discussed in Section 5.5.1, the mover stage and VNA were controlled remotely by a control computer. A control sequence was written in LabVIEW to scan the mover position, while recording all S-parameters. The front panel of the LabVIEW graphical user interface (GUI) is shown in the Fig. 5.23. A user can change the position scan range and the step size of the moves. The program also has options to change the VNA measurement settings. The frequency range of the measurement can be changed along with the number of frequency steps. User can change the format of the measurement, such as 'Smith-chart' or 'dB magnitude'. The VNA source power can be increased if the transmission lines have higher losses.

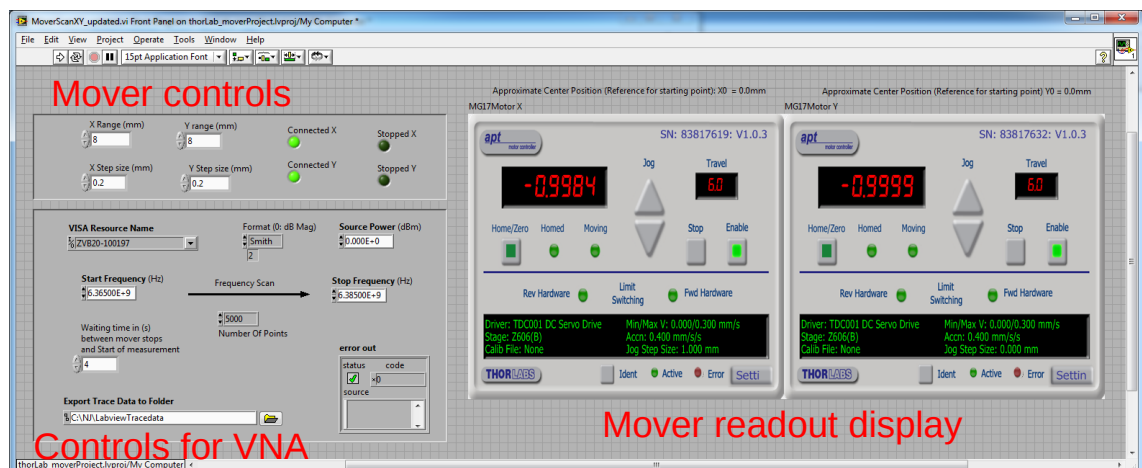


Figure 5.23: GUI interface screen of the LabVIEW program for field orientation measurement scan.

To record a scan, the bead was first moved to the center of the cavity. This was performed by manual observation. After applying appropriate settings for the mover and VNA, the LabVIEW code was executed. The processes flow of the LabVIEW program is shown in Fig. 5.24. The mover was first moved to the starting corner, depending on the specified ranges along x and y axes. To avoid effect of vibration of the bead, a time delay was used between the arrival of the mover at a position and the beginning of S-parameter measurement. No apparent vibration was observed as the mover was moved with low acceleration and the string was stretched appropriately. All sixteen S-parameters were recorded at that position, which are exported as a data file, which also contained the x and y positions of the mover.

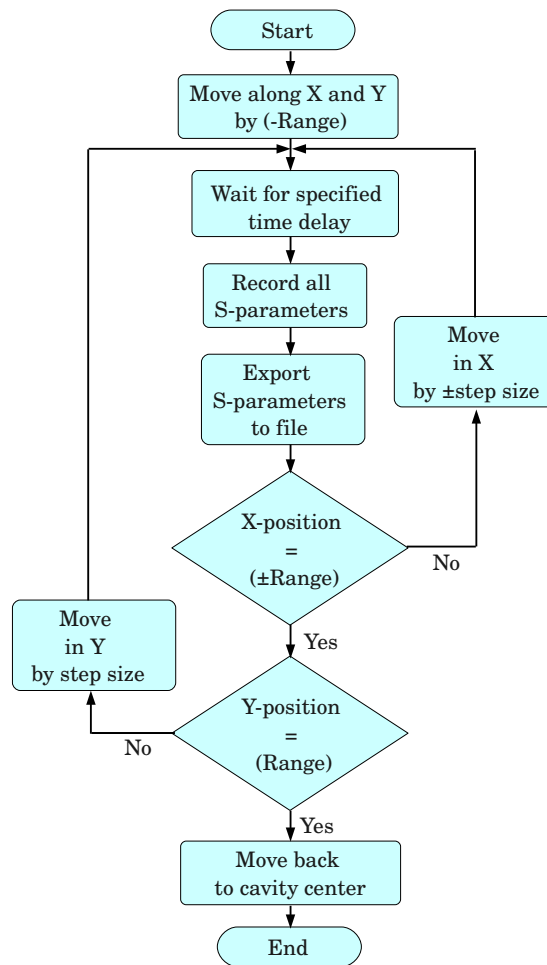


Figure 5.24: Program flow of the LabVEIW sequence for field orientation measurement scan.

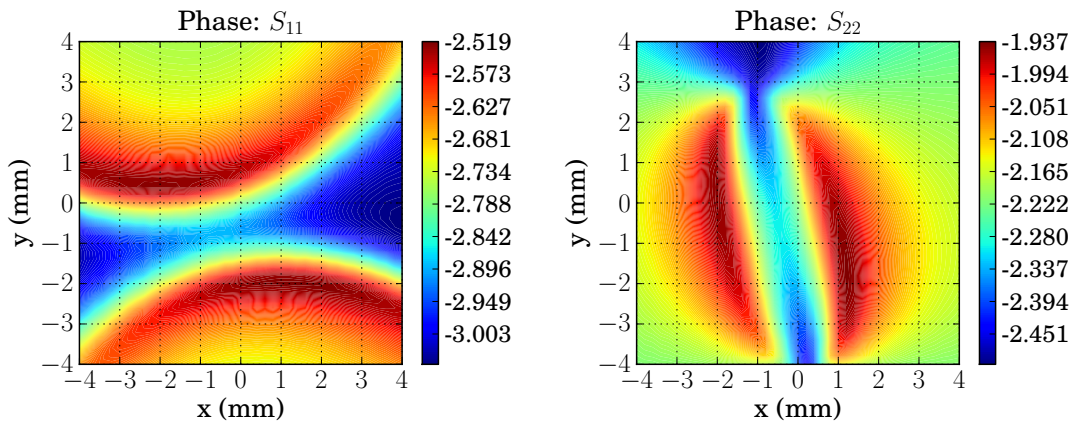
The mover was then moved along x -axis by specified step size, and S-parameters were recorded at each step. After covering the position range along x -axis, the mover was moved along y -axis by specified step size. The mover was now moved in $-x$ -direction until it covers the range along x -axis. In this way, the positions along x -axis were scanned at each position steps along y -axis, until the range along y -axis was covered, and S-parameters were recorded at each position step.

To process the exported S-parameter files, a python code was written which was operated in the parallel mode on the RHUL cluster. The list of the data files was divided into the smaller sub-lists. At a time a master process sent one sub-list to each of the slave processors to analyse. The communication between the processes was performed

through the message passing interface (MPI) system. Each slave process determined the peak frequency and amplitude, or the signal phase at a specific frequency, from all S-parameter files in the sub-list. The extracted results were then sent back to the master process, which wrote them into an output file.

To measure the orientation of the dipole field, the mover was moved from -4 to +4 mm along the x and y axes. In total 1600 S-parameter files were recorded per scan. In each file, all sixteen S-parameters were recorded within frequency range of 6370 to 6380 MHz, with the frequency resolution of ~ 4 kHz. The S-parameters were recorded in the raw (complex smith-chart) format to provide flexibility during post processing. Rather than recording the S-parameter over the bandwidth, measurement at only the peak frequency, or the phase at the unperturbed peak frequency should give the same results. The S-parameters were recorded over the bandwidth to cross compare the results from phase, frequency and amplitude variation. The field orientation of the dipole and quadrupole modes were recorded separately.

Fig. 5.25(a) and 5.25(b) show the phase of the reflected signals at the unperturbed resonant frequencies of the dipole modes coupled to Port-1 and Port-2, measured for different bead positions. The phase contour plot for S_{22} agreed well to an extent with the simulated contour plots in Fig. 5.10(d), except it was not oriented parallel to the



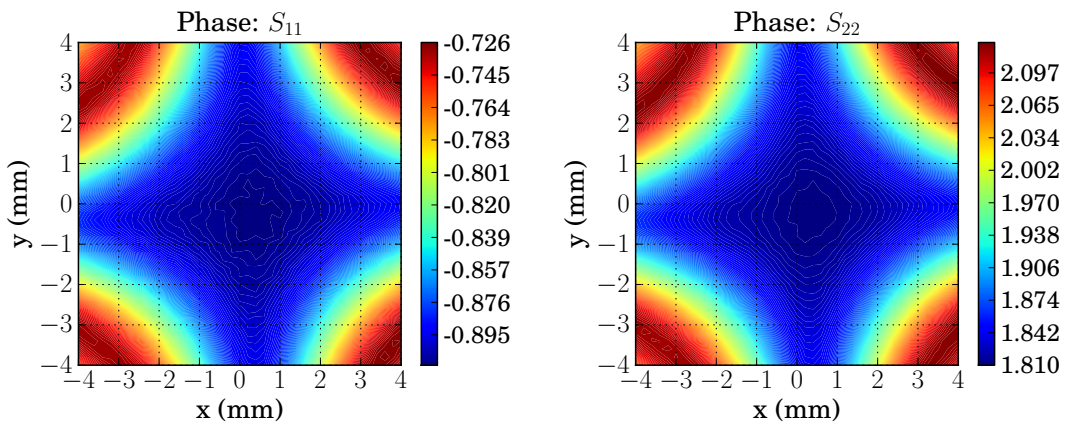
(a) Orientation of the dipole mode field coupled to Port-1.

(b) Orientation of the dipole mode field coupled to Port-2.

Figure 5.25: Measurement of dipole field orientation using phase of the reflected signal.

y -axis. The shape of the phase contours from the S_{11} was different from that for the S_{22} , and it also was not oriented parallel to the x -axis. The angle of rotation, calculated using the phase gradient, was 12.7° .

Fig. 5.26(a) and 5.26(b) show the phase of the reflected waves at the quadrupole frequency for different bead positions, measured at Port-1 and Port-2 respectively. The shape of phase contours agreed well with the simulated contours plotted in Fig. 5.13(c). The quadrupole modes were found to be rotated by 2.9° from the x and y axes.



(a) Orientation of the quadrupole mode field coupled to the Port-1.

(b) Orientation of the quadrupole mode field coupled to the Port-2.

Figure 5.26: Measurement of quadrupole field orientation using phase of the reflected signal.

The field orientation plots created using amplitude of the S-parameter peaks agreed well with the plots created using phase. The change in the resonant frequency for the small plastic bead was very small, resulting in plots without sensible field shapes. The corresponding $x - y$ isolation I_{x-y} for a rotation angle $\Delta\Theta$ of the dipole field can be predicted using,

$$I_{x-y} = 20 \times \ln(\cot \Delta\Theta). \quad (5.17)$$

For $\Delta\Theta = 12.7^\circ$, the $x - y$ isolation should be 13 dB, which agrees well with the isolation calculated from the S-parameters in section 5.5.2. The study of field orientation explained the poorer values of $x - y$ isolation observed during S-parameter measurements. The fields may be rotated because of any unknown asymmetry in the CBPM geometry, due to fabrication errors. The possible reasons for rotation of fields and

their effects on the performance of the BPM were studied, which are presented in the following sections.

5.6 Study of fabrication errors by simulation reconstruction

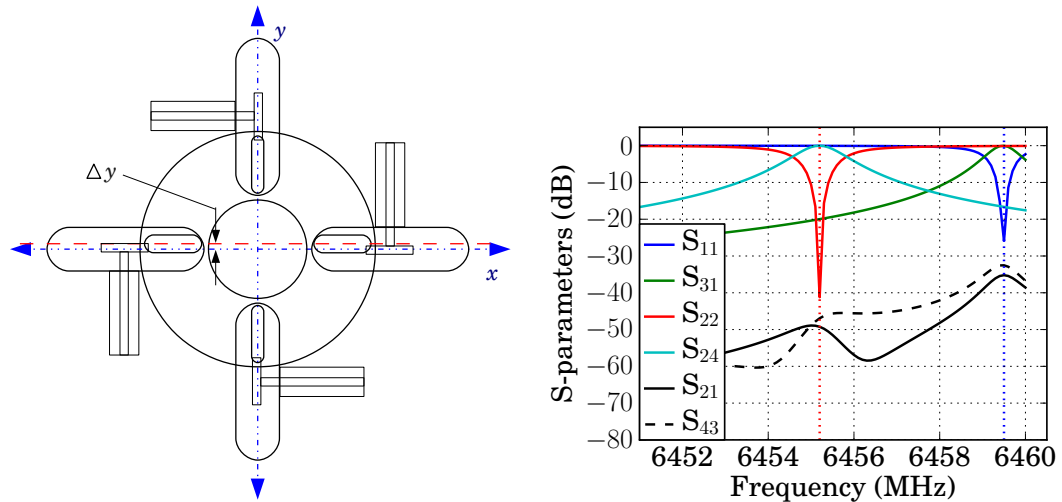
The cavities were fabricated with low tolerances in the sensitive areas such as slots. Even with the specified low tolerances, the resonant frequencies of the dipole modes were lower by 83 MHz from the simulated resonant frequencies. The transmitted signals received at the coupled ports were attenuated more than 8 dB and the $x - y$ isolation was lower than 15 dB. The possible errors in fabrication which can change the cavity parameters are studied using simulation.

The coupling and isolation between the ports should be the most sensitive to the fabrication errors in the slots. With the copper as a cavity material, the modern computer numerical control (CNC) machines can machine and measure geometry with accuracy well below $100 \mu\text{m}$. As the cavity is fabricated with tolerances well below $100 \mu\text{m}$, it can be set as the upper limit for the errors in machining of the slots. An other possible source of error can be the nonuniform fitting of the cavity enclosure cap. Different scenarios were simulated with different fabrication error sizes and their effects on the cavity parameters were studied.

5.6.1 Coupling slots shifted from its axis

If the slots are shifted towards either side of the axes, the magnetic field from the orthogonal dipole mode should cross-couple into the slots and decrease the $x - y$ isolation. Fig. 5.27(a) shows a diagram of a cavity BPM with two of its slots shifted by amount dy , from the x -axis. All other dimensions were kept unchanged.

The CBPM geometries with two slots shifted by different position offsets dy were simulated using S3P in the dipole frequency region. The S-parameters were simulated with



(a) Drawing representing simulation model to study the effects of the slots shifted from its ideal position.

(b) Simulated S-parameters of a CBPM model with two slots offset by $100 \mu\text{m}$ along y -axis.

Figure 5.27: Simulation of S-parameter response of CBPM models with two slots shifted from their ideal positions.

frequency resolution of 100 kHz, which is 10 points within the 3 dB bandwidth of the dipole modes. The ports and boundary conditions were assigned similar to the model of the ideal geometry.

Fig. 5.27(b) shows the S-parameters for a CBPM with slots shifted by $100 \mu\text{m}$. When slots were shifted along y -axis, the trace S_{21} examined the case where the slots along x -axis were shifted towards the slot along $+y$ -axis, and S_{43} examines the case when the slots were shifted away from the slot along $-y$ -axis. The slots were shifted over 0 to $100 \mu\text{m}$ in three steps.

The simulation results for different amount of shifts are summarised in Table 5.12. The resonant frequencies of the dipole modes changed by less than 200 kHz. The signals received at the coupled (opposite) ports were attenuated by less than 0.1 dB. For slots offset by $100 \mu\text{m}$, the isolation degraded up to 32 dB, which was not as low as 13 dB observed during S-parameter measurements. The fabrication errors due to slot offset alone did not alter the cavity parameters by the amounts observed from the RF measurements.

Table 5.12: Variation in frequency and isolation of the CBPMs with slots shifted by different position offsets.

Slot offset $\Delta y(\mu\text{m})$	Peak frequency (MHz)		$x - y$ isolation (dB)	
	S_{42}	S_{31}	$S_{31} - S_{21}$ & $S_{31} - S_{43}$	$S_{42} - S_{21}$ & $S_{42} - S_{32}$
0.0	6455.24	6459.69	51.13 & 52.37	59.01 & 55.58
33.0	6455.10	6459.50	51.63 & 38.50	49.11 & 48.89
66.0	6455.10	6459.60	40.04 & 28.79	35.61 & 35.80
100.0	6455.20	6459.50	35.20 & 32.51	46.94 & 49.24

5.6.2 Performance degradation due to rotated slots

Similar to shifted slots, an another possible scenario can be that the slots are rotated around the cavity axis (z -axis). If the slots are not perfectly aligned to the x or y axes, the axial symmetry is broken, which changes the orientation of the resonance modes. Due to rotation of the field, the amount of cross-coupled magnetic field from the orthogonal dipole mode increases, reducing the $x - y$ isolation.

An example drawing of a CBPM, showing the slots along x -axis been rotated by an angle $\Delta\theta$ around z -axis, is shown in Fig. 5.28(a). The other two slots, along y -axis, were kept at the same position. The slots were rotated by different angles up to 2° , and the transmission and reflection characteristics of the CBPMs were simulated using S3P. The S-parameters calculated for the slot rotation of 1° are plotted in the Fig. 5.28(b). The results of the simulations are listed in the Table 5.13. The $x - y$ -isolation reduced to 23.7 dB when slots were rotated by 1° and further up to 16.5 dB for the rotation of 2° . However the resonance frequencies of the coupled modes varied within 300 kHz from their ideal values. The attenuation of the transmitted signals were less than 0.2 dB for all simulations.

This study replicates a scenario in which a CBPM would have been moved after machining two of the four slots, and then re-installed to cut the remaining two. The standard way to re-align would be to scan a plane outer surface, for example a waveguide surface

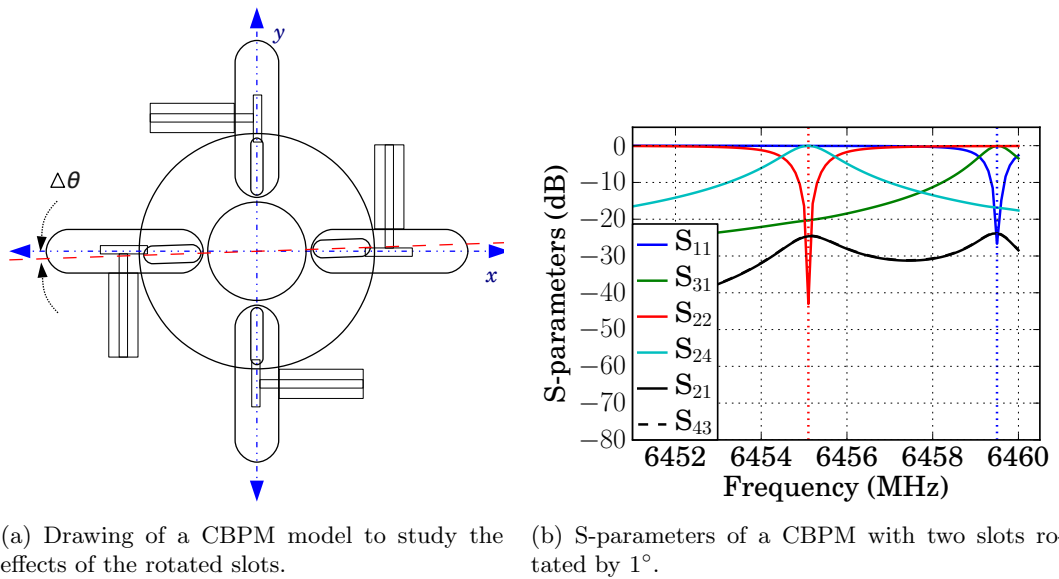


Figure 5.28: Effect slots rotated around cavity axis.

parallel to the x -axis, using an alignment gauge. If the cavity is at an angle $\Delta\theta$ to the x -axis, the gauge at distance x , would have a variation of $x \tan(\Delta\theta)$, which is noted in the second column of Table 5.13. Even for a rotation angle of only 0.33° , the linear variation at the end of the waveguide is $230 \mu\text{m}$, which is well above the detection resolution of a typical position gauge.

The variations in the simulated resonance frequencies and transmission attenuation

Table 5.13: Change in frequency and $x - y$ isolation for slots rotated by different angles.

Slot angle $\Delta\theta$	Arc length (at $x=40$ mm) (mm)	Peak frequency (MHz)		$x - y$ isolation (dB)	
		S_{42}	S_{31}	$S_{31} - S_{21}$ & $S_{31} - S_{43}$	$S_{42} - S_{12}$ & $S_{42} - S_{32}$
0.00	0.00	6455.24	6459.69	51.13 & 52.37	59.01 & 55.58
0.33	0.23	6455.00	6459.50	25.04 & 25.16	27.04 & 27.52
0.66	0.46	6455.20	6459.50	26.95 & 27.13	28.28 & 28.19
1.00	0.70	6455.10	6459.50	23.82 & 23.71	24.50 & 24.60
1.50	1.05	6455.00	6459.70	17.76 & 17.82	19.41 & 19.32
2.00	1.40	6454.90	6459.80	16.55 & 16.62	17.69 & 17.83

were not large enough to explain the observations of RF measurements. Based on the simulations, the rotation of the slots should neither lower the resonance frequencies nor degrade the $x - y$ isolation as much as observed during the S-parameter measurements.

5.6.3 performance degradation due to misalignment of the enclosing cap

The resonant cavity was fabricated in two pieces. As shown in Fig. 5.29, the opened end of the cavity cylinder was enclosed using a metallic cap. The metallic cap was fitted and then brazed to the cavity. During the heating cycle of the brazing, it is possible that a thin gap of uneven thickness could have been created between the cavity and cap due to the thermal expansion and contraction of the copper. In addition, it is possible that the brazing material did not fill the gap uniformly around the cavity.

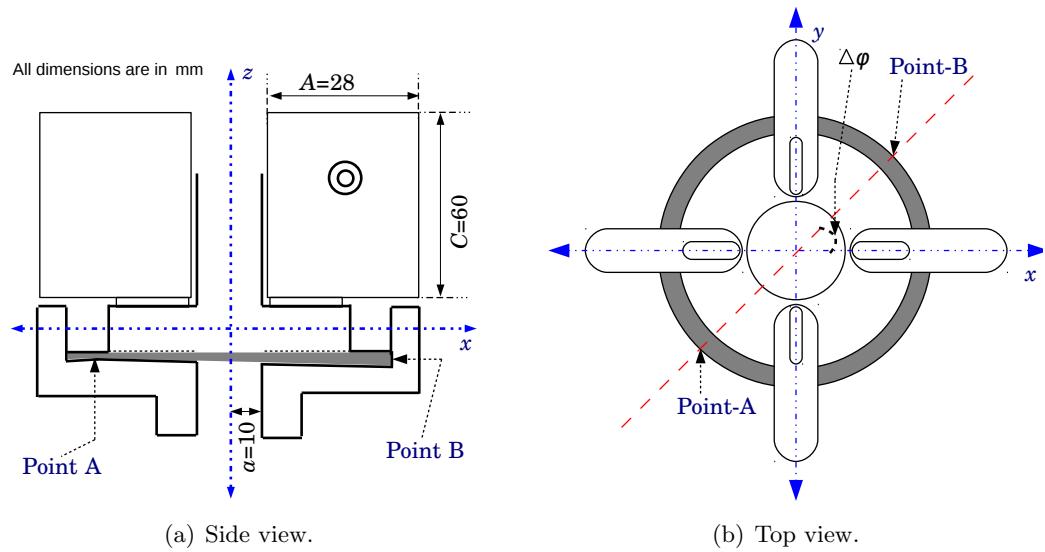


Figure 5.29: Simplified drawings of a CBPM showing an uneven gap between cavity and enclosing cap in a simulation model to reconstruct the fabrication errors.

As shown in Fig. 5.29(a) and 5.29(b), a gap was considered which has a minimum height near Point-A, and the height is maximum at the other end of the diameter, marked as Point-B. The vector \overrightarrow{AB} points in the direction of positive height gradient. The gap can be formed such that the \overrightarrow{AB} is at any angle $\Delta\phi$ with the x -axis.

An uneven cylindrical gap of diameter 62 mm, height of 100 μm at Point-A and 250 μm at Point-B, was inserted into the simulation model at different angles $\Delta\phi$. The height at the Point-A is referred as the height of the gap for rest of this section. A CBPM models with the cap rotated by different angles $\Delta\phi$ were simulated using the Eigenmode solver in GdfidL. GdfidL was used because the gap could not be meshed accurately using Cubit for the ACE3P solvers. It should be possible to mesh the model using Cubit, but it is easier to control the mesh in the GdfidL because of its explicit control on the mesh parameters.

Fig. 5.30(a) and 5.30(b) shows the equi-amplitude contours of the electric fields of the two dipole modes, when the cavity cap was rotated by 45° . Unlike the dipole fields in an ideal CBPM geometry (shown in Fig. 5.10(c) and 5.10(d)), the dipole fields in a cavity with misaligned cap were not aligned to the coupling slots. The rotation of the cavity cap, disorients the dipole fields from the slots along x and y axes. The rotation angle of the cap was scanned between 0 to 180° and the rotation of the dipole field was determined from the simulation results. As plotted in Fig. 5.31(a), the field rotation angle $\Delta\Theta$ increased with the cap rotation angle $\Delta\phi$. When the cap was rotated by 90° ,

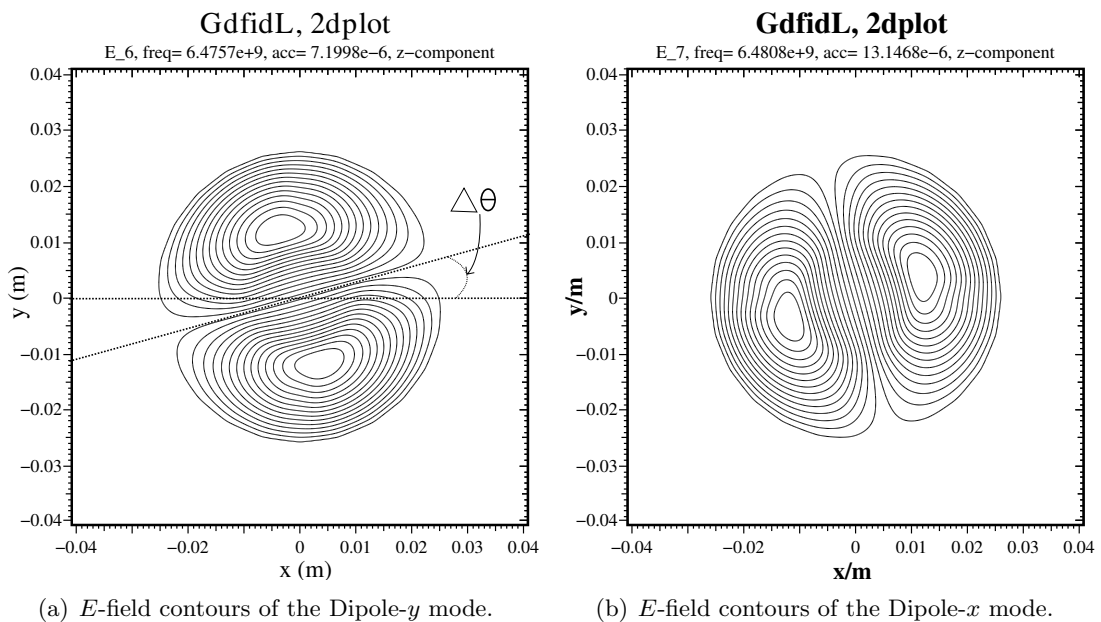
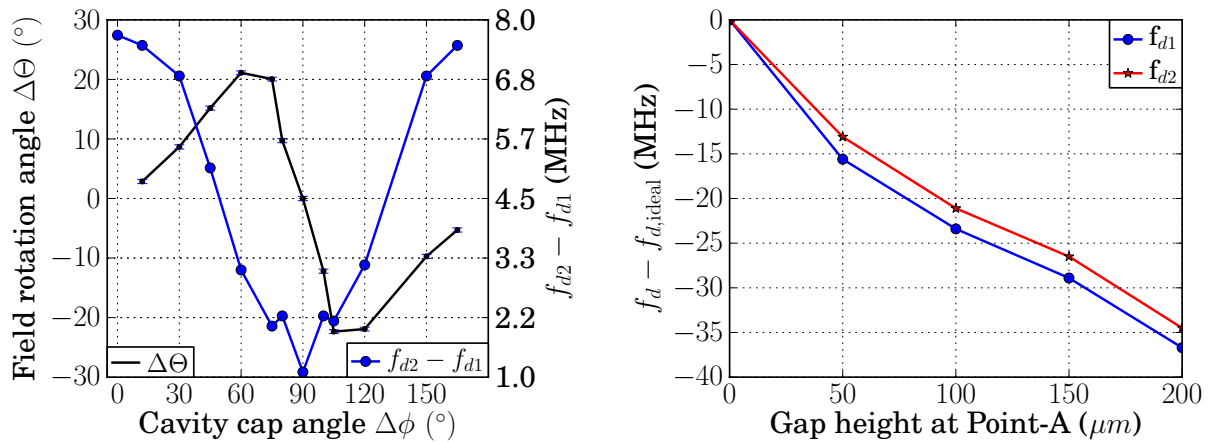


Figure 5.30: Rotation of the dipole fields due to the enclosing cap rotated by angle $\Delta\phi = 45^\circ$.

the modes were realigned to the slots. The cap rotation of more than 90° acted as a supplementary angle, and rotated the modes in the opposite direction.

In addition to the rotation of fields, the frequency separation ($f_{d2} - f_{d1}$) between the two dipole modes also changed with the rotation of cap. When the angle $\Delta\phi$ was increased, the thicker end of the gap at Point-B moved towards the narrower slots along y -axis. The thicker gap reduced the frequency f_{d2} , but increased the frequency f_{d1} of the dipole mode coupled through the wider slots along x -axis.

To study the effect of different gap height, it was scanned from 50 to 200 μm , with cap rotated by angle $\Delta\phi$ of 45° . The change in resonance frequencies ($f_d - f_{d,\text{ideal}}$) of the dipole modes for gaps of different height are shown in Fig. 5.31(b). The resonance frequencies of the dipole modes in absence of the gap, shown in Fig. 5.10(c) and 5.10(d), was used as an ideal frequencies $f_{d,\text{ideal}}$. The resonance frequencies decreased by more than 35 MHz for a gap of 200 μm height.



(a) Rotation angle of the dipole mode fields and frequency separation between the dipole modes for different cap rotation angle $\Delta\phi$.

(b) Change in the resonance frequencies of the dipole modes with gap heights

Figure 5.31: Results from Eigenmode simulations to study the effects of a misaligned cavity cap on the field orientation and resonance frequencies of the dipole modes

The simulation studies showed that any additional asymmetry in the cavity will disorient the dipole mode fields from the slots. The asymmetry can be in the form of the cavity cap rotated by angle $\Delta\phi$, or the asymmetric filling of the brazing material in

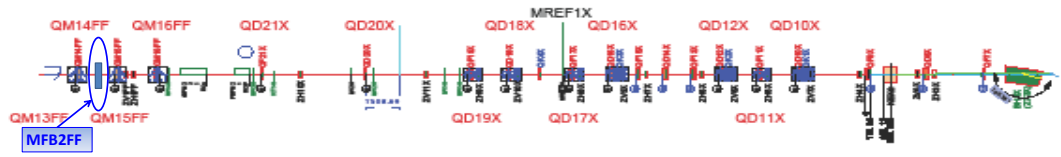
the gap of a constant height. The resonance frequencies of the modes decreased with increase in the gap height, and a gap of appropriate height should be able to decrease the resonance frequencies by the observed difference. The difference in the cavity parameters can be due to a combined influence of more than one type of fabrication errors, and it is difficult to carry any detailed experimental study as the cavity has already been brazed.

5.7 Beam testing at ATF2 beam line

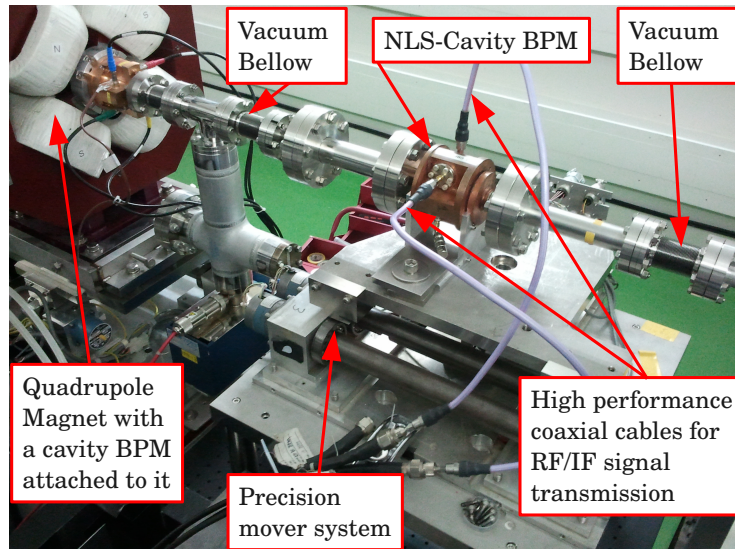
To test the beam coupling strength of the CBPMs, three of the four cavities were installed at the Diamond Light Source, while the cavity tested at Royal Holloway was installed at ATF2 extraction line at KEK in Japan. An existing operational cavity BPM system and shorter bunches were the additional benefits in testing the CBPM at ATF2. The typical bunch length at ATF2 is 8 mm, compared to 90 mm at Diamond

The design and operation of the ATF machine and ATF2 beam line were explained in Section 4.1. As explained in the Section 4.1, a low emittance beam of relativistic electrons was transferred through ATF2 beam line. The ATF2 beam line already had an operational cavity BPM system, reading bunch positions using 36 cavities in the C- and S-bands.

Fig. 5.32 shows the location of the prototype CBPM on a block diagram of ATF2 beam line, the installation setup, and near by machine components on the extraction line. The NLS-cavity was installed on an existing precision mover system, labeled as MFB2FF, which was fixed on a girder. The mover was able to scan position in the transverse plane with position resolution of $1 \mu\text{m}$. The vacuum bellows on both sides suppressed any stress due to cavity movement, and enabled to move the cavity independently of the neighbouring components. One of the neighbour cavities is shown fixed to a quadrupole magnet. The new CBPM can use the electronics system from one of the neighbor CBPMs.



(a) Block diagram of machine components of the ATF2 beam line section, and the new CBPM installed on MFB2FF mover.



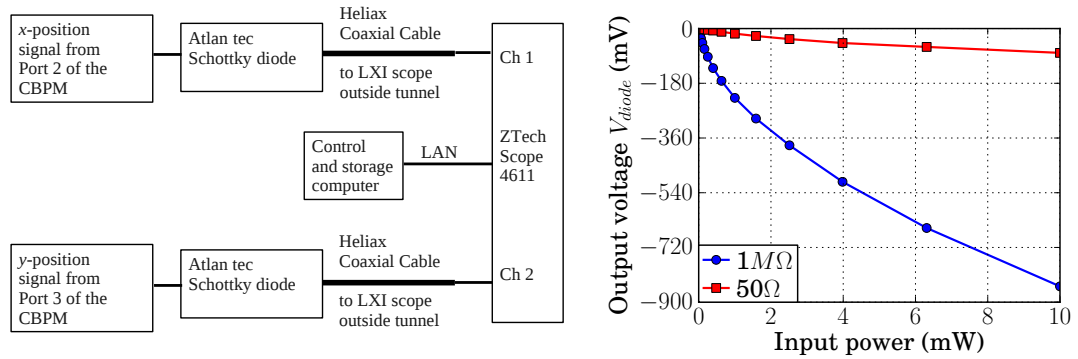
(b) NLS cavity installation setup showing cavity, precision movers and neighboring machine components.

Figure 5.32: NLS cavity installation at ATF2.

5.7.1 Cavity response measurements using diode

As a first check, the RF output signals from the cavity were detected using the self biased Schottky barrier diodes. Block diagram of a connection scheme for the beam testing with the CBPM and diodes is shown in Fig. 5.33(a). The output from the two cavity ports, one port each for x and y position measurement, were connected to the diodes through high frequency cables. The output signals of the diodes were transferred through the Heliax cables to outside of the accelerator tunnel. There the signals were digitised for further processing. A digital oscilloscope, model ZT4611 from ZTEC instruments, was used as a digitiser.

In the laboratory setups, the Schottky barrier diode is operated in the square law region. Its output is detected across a high load impedance of value more than $1\text{ M}\Omega$



(a) Block diagram of a setup for measurement of cavity response using diode.

(b) Calibration of a diode with output load of 1 MΩ and 50 Ω.

Figure 5.33: Block diagram of a connection setup for beam measurement of the CBPM with diode, and diode sensitivity at different load impedances.

for maximum sensitivity. As the characteristic impedance of the transmission cable was 50 Ω, the diode output signal was getting reflected from the 1 MΩ load impedance of the digitiser. Multiple signals were observed while detecting with the digitiser load impedance of 1 MΩ due to multiple reflections between the digitiser impedance and detector diode.

To avoid multiple reflections, the output of the diode was digitised with the load impedance of 50 Ω. To check the diode sensitivity with the two load impedances, a diode was calibrated with the load impedances of 1 MΩ and 50 Ω. As shown in Fig. 5.33(b), for any input power, the output of the diode voltage across 50 Ω was considerably lower than when measured across 1 MΩ. The calibration data was used to calculate the input RF power from the output voltage of the diode.

A typical cavity output signal detected with a diode is plotted in Fig. 5.34(a). In absence of any frequency filter, the power coupled out from the higher order modes of the CBPM will also reach the diode input. The amplitude oscillations at the beginning of the signal could be because of the higher order modes. An exponential function was fitted to determine the amplitude decay constant for the x and y position signals, which were found to be 124 ± 2.4 ns and 133 ± 2.7 ns respectively. The input power to the diode was calculated from the output voltage, using the calibration curve for the diode, plotted in Fig. 5.34(b). Signal attenuation of 1.5 dB in various cables was

accounted while calculating the output power and voltage at the cavity output ports.

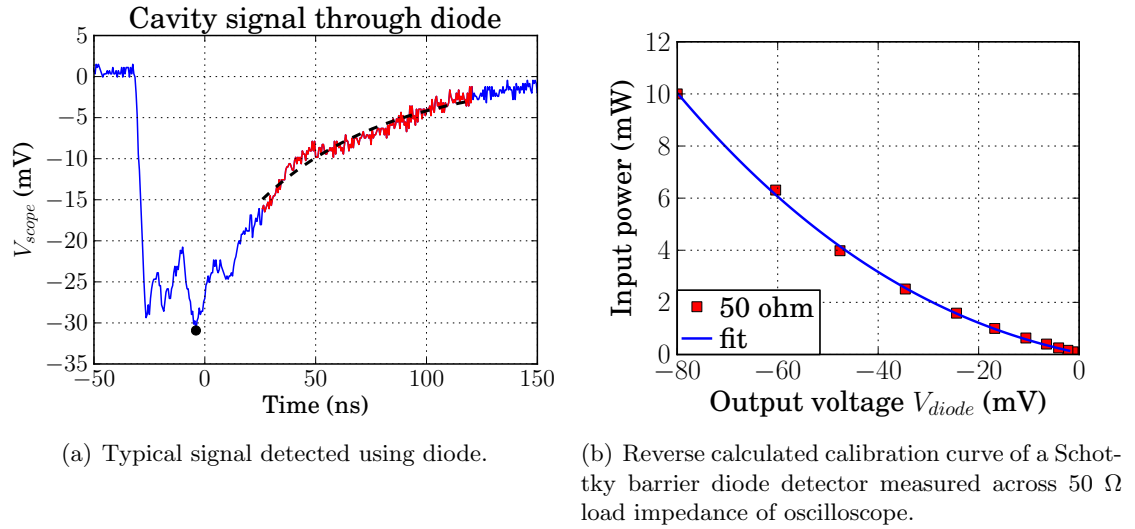


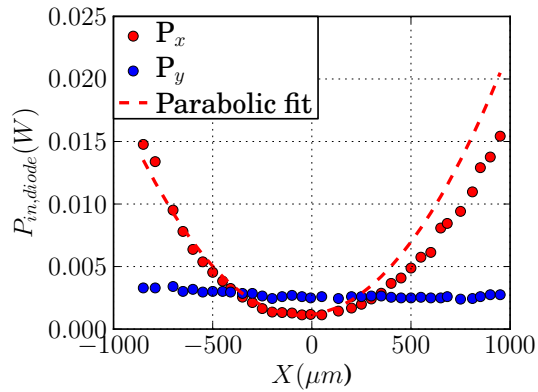
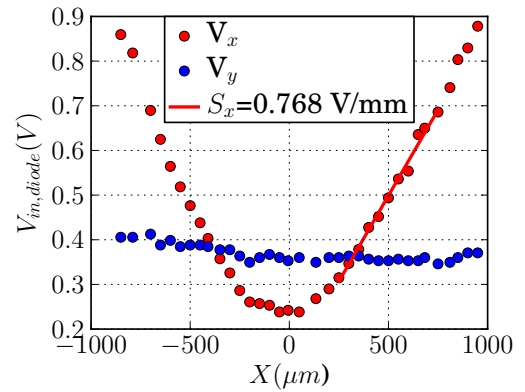
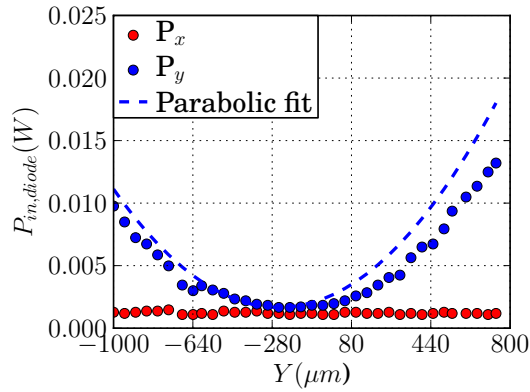
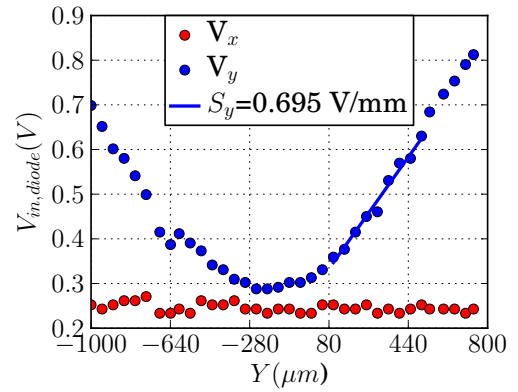
Figure 5.34: Typical cavity output signal detected using diode and reverse calibration curve for diode.

To determine the position sensitivities S_x and S_y of the CBPM, the cavity position was scanned along x and y axes using the precision mover, and at each position a CBPM signal from diode was recorded. While the cavity was scanned along x -axis, the scope was triggered at a peak voltage of y position signal, and vice versa. Triggering the scope at peak voltage of the other channel should reduce the effect of the charge fluctuations.

The peak power and voltage, at the cavity output, at different mover positions during calibration scans along the x and y axes are shown in Fig. 5.35. The voltage V_x , coupled through the wider slots along the y -axis, should be higher than V_y , which was coupled through the narrower slots along x -axis. The position sensitivities S_x and S_y for the x and y positions measurements were 0.768 and 0.695 V/mm respectively, which were around 10% more than the voltage sensitivity predicted by inserting the cavity parameters from the RF measurements and simulations, into the Eqn. 2.18.

In Table. 5.14, the amplitude decay constant (τ) and position sensitivity (S_x and S_y) derived from the calibration are compared to the same calculated from the RF measurements.

Even if the cavity was moved along one axis, for example x -axis as plotted in Fig. 5.35(b),

(a) Cavity output power measured during position scan along x -axis.(b) Cavity output voltage measured during position scan along x -axis.(c) Cavity output voltage measured during position scan along y -axis.(d) Cavity output voltage measured during position scan along y -axis.Figure 5.35: Calibration of CBPM along x and y axes, the cavity outputs were detected using Schottky barrier diodes.

the output voltage V_y for the y -position signal also changed because of the cross coupling. The voltage change in the cross coupled signal is more visible in Fig. 5.35(b)

Table 5.14: Results of beam measurements with signal detection using diodes.

Direction	From RF Measurements		From diode measurements	
	Decay time (ns)	Sensitivity (V/mm)	Decay time (ns)	Sensitivity (V/mm)
x	77	0.69	124 ± 2.4	0.76
y	93	0.62	133 ± 2.6	0.69

compared to Fig. 5.35(d), because the cavity was kept at a higher constant position offset along y -axis while scanning along x -axis. A cross-coupled sensitivity $S_{\text{cross-coupled}}$ can be calculated from the normal sensitivity as,

$$S_{\text{cross-coupled}} = S [\sin(\Delta\Theta) / \cos(\Delta\Theta)], \quad (5.18)$$

where $\Delta\Theta$ is the dipole field rotation angle measured using bead perturbation method, S is the normal sensitivity of CBPM derived from calibration in the corresponding direction. The cosine term compensates for the error in the measurement of the normal position sensitivity, due to the field rotation. The cross-coupling sensitivity, calculated using S and field rotation angle $\Delta\Theta$ of 12.9° in the above equation, should be 0.174 and 0.158 V/mm for the x and y position signals respectively. It was not possible to calculate conclusive numbers of cross-coupling sensitivity from the recorded scans, because of the smaller signal levels and the presence of the position and charge jitter. As the data was not acquired synchronously, it was not possible to remove the charge and position jitter.

5.8 Summary

As presented in this chapter, new concepts to design an efficient CBPM system on a large scale have been studied. A cylindrical CBPM has been designed with two dipole modes separated and pre-aligned to improve the $x - y$ isolation without mechanical tuning. The EM behavior of different CBPM designs were simulated using Eigenmode, S-parameter and time domain solvers. The simulations showed that it was possible to align and separate the dipole modes using coupling slots of different width along x and y axes. The S-parameters, Q values and orientations of the resonance modes were measured using RF bench top measurement setups. Possible sources of difference have been studied, including slot displacement, rotation and end cap tilt. The end cap tilt showed the most promise in describing the observed dipole mode frequency shift and cross-coupling. The beam position sensitivity of a CBPM was tested on ATF2 extraction line, by detecting the cavity output signals using diodes as a preliminary test. The cavity output voltage should be studied in detail, using filters and heterodyne detec-

tion, in synchronisation with the charge and position measurements on other CBPMs. Overall the sensitivity agreed with expectations as measured at the ATF, although the cross-coupling could not be verified.

Conclusions and discussion

A set of studies carried to design a large scale RF cavity BPM system for electron accelerators with closely spaced bunches are presented in this thesis. The required key topics, such as a simpler cavity design, the effects of signal overlapping and effects of ambient temperature variation, were identified. Each of these topics were examined in detail on operational accelerators through collaboration projects. A simplified and more efficient CBPM design for large scale production and operation was studied through a CBPM design project in collaboration with the Diamond Light Source. The effects of temperature variation and signal overlapping due to a shorter bunch spacing were studied on the CBPM system operational at ATF2 in KEK, Japan. The outcomes of the studies are summarized as follows.

6.1 Summary of multi-bunch signal processing study

A digital processing method, based on a signal subtraction algorithm, has been developed to remove the signal pollution from the previous bunches, when the temporal bunch separation is small. The performance of the code was tested on the CBPM signals from beam as well as the simulated signals. A code was written to simulate the CBPM signals from a bunch train with user defined parameters. To study the performance of the algorithm with actual beam, ATF was operated in a multi-train mode.

The code was tested with two and three bunches, and for different bunch separations. After signal subtraction, the error in the bunch position measurement was reduced from 67% to less than 2%. The jump in IQ phase, was studied with different bunch separations, and it was due to the difference between the resonance frequencies of dipole and reference cavities. The signal subtraction algorithm was tested with different CBPMs. The beam jitter in position measurement from a CBPM was subtracted using the SVD based correlation with two neighbor CBPMs. As listed in Table 6.1, after SVD based beam position jitter subtraction, the measurement error in y position were reduced to 1.08 and 1.81 μm for bunch 1 and 2 respectively.

Table 6.1: Error in position measurement after SVD based beam position jitter subtraction.

CBPMs	Error in position measurement (μm)			
	x position		y position	
	Bunch 1	Bunch 2	Bunch 1	Bunch 2
MQM11FF	2.18 ± 0.62	2.15 ± 0.74	1.97 ± 0.47	3.01 ± 0.87
MQM12FF	1.53 ± 0.27	2.37 ± 0.68	1.03 ± 0.20	1.81 ± 0.46
MQM13FF	4.08 ± 1.13	7.29 ± 2.90	1.24 ± 0.34	1.74 ± 0.49

6.2 Summary of CBPM design study

As discussed in Chapter 5, a cavity has been designed with its dipole modes pre-aligned to the coupling slots and separated in frequency to improve the $x - y$ isolation without mechanical tuning. The dipole modes were forced to align by breaking cavity symmetry using the coupling slots of different widths in the x and y planes. A simpler geometry model was simulated with different slot widths, which showed that the dipole frequencies are more sensitive and prone to fabrication errors with the narrow slots than with wider slots.

A waveguide adapter has been designed which is less sensitive to the fabrication errors. Inserting an additional conductor bead at the end of the central conductor probe increased its capacitance, which allowed to increase the gap between the conductor probe

and waveguide wall from a typical value of $0.2 \mu\text{m}$ to 3.5 mm . Larger gap made it less sensitive to the fabrication errors. Simulations showed that adding the conductor bead also increased the frequency bandwidth of the adapter by more than 1 GHz and made the transmission attenuation equal over the frequency range of the cavity dipole modes.

The EM response of the CBPM design was predicted by simulations using the Eigenmode, S-parameter and time domain solvers of ACE3P. The simulation results from different solvers were cross-compared, and they confirmed that the two dipole modes were aligned to the coupling slots and separated in frequency by 4.5 MHz . The reflection at the peak frequencies were lower than -45 dB , while the $x - y$ isolation was better than 51 dB . The time domain simulation predicted the output signal sensitivity, from an electron bunch at ATF2, to be $3 V_{pp}$.

Out of the four cavities fabricated, RF parameters of one cavity were measured at Royal Holloway. The S-parameter measurements using VNA showed that the dipole modes were separated in frequency by 5.5 MHz , which is better than the simulation predictions. On other hand, the transmission loss was up to -10.3 dB , while the maximum reflection was -8.3 dB at one of the ports. The resonant frequencies of the dipole modes were lower by more than 80 MHz , than those predicted by EM simulations. The Q values were calculated using the transmission as well as an impedance method. Q_L of both dipole modes agreed with the Eigenmode simulation, but the calculated Q_0 were lower than the simulated values. To understand the reasons for lower values of $x - y$ isolation, the orientation of the EM fields of the dipole and quadrupole modes were measured using a dielectric perturbation technique. The study revealed that the two dipole modes were not aligned to the coupling slots, but were rotated by 12.7° . The rotation of fields explained, and agreed well with, the measured $x - y$ isolation of 13 dB .

Different fabrication errors, which can degrade the $x - y$ isolation and rotate the fields, were studied by simulation. The isolation was sensitive to the rotation of the coupling slots, but it did not decrease the resonant frequencies by 80 MHz . The perturbations due to misaligned cavity cap showed the most of the observed parameter variations, such as the field rotation and reduction in resonant frequency. Because the cavity has

been brazed, it was not possible to experimentally verify the simulation results, without destroying the cavity. The simulation studies gave good estimation of the influence of different fabrication errors on the performance of a CBPM.

One of the four CBPMs was installed on the ATF2 extraction line to verify its beam sensitivity. The output signal from the cavity was detected using Schottky diodes and digitised for further processing. The cavity was calibrated by moving it along the x and y axes using a precision mover. The CBPM showed sensitivity of 0.76 and 0.69 V/mm for x and y position offsets respectively, which were in agreement with the values predicted using the cavity parameters determined from the RF measurements.

The issues of ambient temperature variation and signal overlapping were studied using the existing CBPM system at ATF2. The variation in the dipole frequency of an S-Band cavity was noted when the cavity was at different temperatures. The dipole frequency decreased with increase in the temperature at the rate of -36 kHz/°C. If the cavity temperature changes, the variation in the dipole frequency can be estimated using this study, and it can be taken in to account while calculating the beam position.

Overall, an economic and efficient design of cylindrical CBPM with separated dipole modes was created, simulated, fabricated, and tested for RF and beam response. The methods for simulation and testing were studied in detail. Deeper understanding of the working principle of a CBPM was developed by comparing different simulations, RF measurements and beam measurements, which can be used to predict its beam response based on the bench top RF measurements. The study of signal subtraction technique showed that the algorithm removes the large systematic error in the position measurement due to the signal pollution from previous bunches. The signal subtraction technique extended the application of the CBPM systems, with relatively higher Q cavities, to the accelerators with shorter bunch separation, which was not earlier possible. It also made it possible to apply the calibration coefficients derived from system calibration in single bunch mode, to calculate the position of any bunch in a bunch train with known bunch separation. The studies presented in this thesis serve as a set of essential studies for design and operation of a large scale cavity BPM system on the electron accelerators with challenging beam parameters.

6.3 Discussion of open research questions

Even though the research topics identified at the beginning of the projects are studied in detail, new topics of interest appeared during the course of their studies, which could not be examined due to limited time. To study the effects of digital and analog filters on the CBPM signals from multiple bunches and performance of the signal subtraction method, more CBPM signals should be recorded at different bunch separations. The effects of analog filters and non-linearity in the electronic components should be included in the signal simulation code. Even though it should be straight away possible to apply the signal subtraction technique to any CBPM signal at a harmonic of the bunch arrival frequency, and processed in a homodyne mode; it should be studied further in detail to apply it on the CBPM signals at other frequencies, higher to be digitised accurately by the available digitiser systems.

The effects of fabrication errors should be checked experimentally using a set of cavity components, with its different parts kept together using a clamp or holder setup and conducting paste, without brazing. Different errors can be recreated and their effects can be studied through RF measurements. The beam coupling and $x - y$ isolation of the new CBPM installed on ATF2 should be studied in detail, same as the other CBPMs, using the electronic and digital signal processing. The position readouts from new CBPM should be correlated with the position readout of the other CBPMs, and the error due to beam jitter should be removed to determine the system resolution.

Multibunch Signal calculation

Considering a CBPM with dipole at an angular resonance frequency of ω_d and amplitude decay constant τ_d . The bunches are separated in time by Δt_b . The signal extracted from the CBPM after passage of the first bunch can be written as,

$$\begin{aligned} V(t_{s,1}) &= A_{1,\text{peak}} e^{-\frac{t_{s,1}-t_{b,1}}{\tau_d}} e^{i[\omega_d(t_{s,1}-t_{b,1})]} \\ &= A_1 e^{i(\omega_d t_{s,1} - \phi_{d,1})} \end{aligned} \quad (\text{A.1})$$

where $A_{1,\text{peak}}$ is the initial peak amplitude of the signal induced by the first bunch and $t_{b,1}$ is the arrival time of the first bunch,

$$A_1 = A_{1,\text{peak}} e^{-\frac{t_{s,1}-t_{b,1}}{\tau_d}},$$

and

$$\phi_{d,1} = \omega_d t_{b,1}.$$

Now considering $t_{s,j} - t_{s,j-1} = \Delta t_b$ for simplicity of calculation, the net signal after

passage of the second bunch can be written in a similar way as,

$$\begin{aligned}
V(t_{s,2}) &= A_{1,\text{peak}} e^{-\frac{t_{s,2}-t_{b,1}}{\tau_d}} e^{i[\omega_d(t_{s,2}-t_{b,1})]} + A_{2,\text{peak}} e^{-\frac{t_{s,2}-t_{b,1}-\Delta t_b}{\tau_d}} e^{i[\omega_d(t_{s,2}-t_{b,1}-\Delta t_b)]} \\
&= A_1 e^{-\frac{\Delta t_b}{\tau_d}} e^{i(\omega_d t_{s,2}-\phi_{d,1})} + A_2 e^{i(\omega_d t_{s,2}-\phi_{d,1}-\Delta\phi_d)} \\
&= B_2 e^{i(\omega_d t_{s,2}-\theta_{d,2})}.
\end{aligned} \tag{A.2}$$

If the resonance frequency of a cavity is not integer multiple of the bunch repetition frequency ω_b , then there will be a certain phase difference $\Delta\phi_d$ between the signals induced by consecutive bunches, otherwise the phase difference will be zero.

To find the amplitude and phase of the signal by the process of frequency down conversion, the raw signal is mixed with an LO signal of unit amplitude and of frequency same as that of the CBPM signal. The mixed signal is then filtered through low pass filter to remove the high frequency signal component. The processed signal can be written as,

$$\begin{aligned}
V(t_{s,2}) &= A_1 e^{-\frac{\Delta t_b}{\tau_d}} e^{-i\phi_{d,1}} + A_2 e^{-i(\phi_{d,1}+\Delta\phi_d)} \\
&= B_2 e^{-i\theta_{d,2}}.
\end{aligned} \tag{A.3}$$

As shown in the above equation that the net signal from the two bunches is a vector addition of the two signals induced by the individual bunches, whose net amplitude and phase can be calculated as,

$$B_2 = \sqrt{\left(A_1 e^{-\frac{\Delta t_b}{\tau_d}} \cos \phi_{d,1} + A_2 \cos(\phi_{d,1} + \Delta\phi_d) \right)^2 + \left(A_1 e^{-\frac{\Delta t_b}{\tau_d}} \sin \phi_{d,1} + A_2 \sin(\phi_{d,1} + \Delta\phi_d) \right)^2} \tag{A.4}$$

and

$$\theta_2 = \tan^{-1} \left(\frac{A_1 e^{-\frac{\Delta t_b}{\tau_d}} \sin \phi_{d,1} + A_2 \sin(\phi_{d,1} + \Delta\phi_d)}{A_1 e^{-\frac{\Delta t_b}{\tau_d}} \cos \phi_{d,1} + A_2 \cos(\phi_{d,1} + \Delta\phi_d)} \right). \tag{A.5}$$

Similar to the Eqn. A.3 for two bunches, the signal induced by three bunches can be

calculated as,

$$\begin{aligned}
V(t_{s,3}) &= A_1 e^{-\frac{2\Delta t_b}{\tau_d}} e^{-i\phi_{d,1}} + A_2 e^{-\frac{2\Delta t_b}{\tau_d}} e^{-i(\phi_{d,1}+\Delta\phi_d)} + A_3 e^{-i(\phi_{d,1}+2\Delta\phi_d)} \\
&= A_3 e^{-i(\phi_{d,1}+2\Delta\phi_d)} + B_2 e^{-\frac{\Delta t_b}{\tau_d}} e^{-i\theta_{d,2}} \\
&= B_3 e^{-i\theta_{d,3}},
\end{aligned} \tag{A.6}$$

where

$$B_3 = \sqrt{\left(A_3 \cos(\phi_{d,3} + 2\Delta\phi_d) + B_2 e^{-\frac{\Delta t_b}{\tau_d}} \cos\theta_{d,2} \right)^2 + \left(A_3 \sin(\phi_{d,3} + 2\Delta\phi_d) + B_2 e^{-\frac{\Delta t_b}{\tau_d}} \sin\theta_{d,2} \right)^2} \tag{A.7}$$

and

$$\theta_3 = \tan^{-1} \left(\frac{A_3 \sin(\phi_{d,3} + 2\Delta\phi_d) + B_2 e^{-\frac{\Delta t_b}{\tau_d}} \sin\theta_{d,2}}{A_3 \cos(\phi_{d,3} + 2\Delta\phi_d) + B_2 e^{-\frac{\Delta t_b}{\tau_d}} \cos\theta_{d,2}} \right). \tag{A.8}$$

From Eqn. A.6 the signal induced by only third bunch can be calculated by subtracting the decayed signal sampled during second bunch as,

$$A_3 e^{-i(\phi_{d,1}+2\Delta\phi_d)} = B_3 e^{-i\theta_{d,3}} - B_2 e^{-\frac{\Delta t_b}{\tau_d}} e^{-i\theta_{d,2}} \tag{A.9}$$

Eqn. A.9 shows that the signal pollution due to all previous bunches can be removed by subtracting the phasors sampled during only the immediate previous bunch. The phasors sampled during bunch 1 and bunch j will have phase difference of $j \cdot \Delta\phi_d$.

Bibliography

- [1] M. S. Livingston, J. P. Blewett, “Particle accelerator”, McGraw Hill, New York, USA, (1962).
- [2] E. O. Lawrence and M. S. Livingston, “The production of high speed light ions without the use of high voltages”, *Physical Review*, 40, pp 19, (1932).
- [3] E. J. Lofgren, “Experiences with the BEVATRON”, UC Radiation Lab Document UCRL-3369, (1956).
- [4] CMS Experiment (CERN), “Observation of a new particle with a mass of 125 GeV”, <http://cms.web.cern.ch/news/observation-new-particle-mass-125-gev>, CMS news, July 4, 2012.
- [5] ATLAS Experiment (CERN), “Latest results from ATLAS Higgs search”, <http://www.atlas.ch/news/2012/latest-results-from-higgs-search.html>, ATLAS news, July 4, 2012.
- [6] Edward J. N. Wilson, “An introduction to particle accelerators”, Oxford University Press, ISBN 978-0198508298, Oxford, UK, (2001).
- [7] P. Raimondy, M. Ross et al., “SLC-The end game”, SLAC-PUB-9724, California, USA, April 2003.
- [8] Edited by N. Phinney, N. Toge, N. Walker, “Accelerator”, ILC reference design report, 3, August 2007.

-
- [9] The CLIC study team, “A 3 TeV e^+e^- linear collider based on CLIC technology”, CERN-2000-008, CERN, Geneva, Switzerland, (2000).
- [10] M. Battaglia, A. De Roeck, J. Ellis, D. Schulte, “Physics at the CLIC multi-TeV linear collider”, CERN-2004-005, CERN, Geneva, Switzerland, (2004).
- [11] Edited by L. Linssen, A. Miyamoto, M. Stanitzki, H. Weerts, “Physics and Detectors at CLIC: CLIC Conceptual Design Report”, CERN-2012-003, CERN, Geneva, Switzerland, (2012).
- [12] Edited by H. Schmickler, P. Lebrun, N. Toge, N. Phinney, T. Garvey, P. Burrows, K. Peach, M. Draper, M. Aicheler, “A Multi-TeV Linear Collider based on CLIC technology: CLIC Conceptual Design Report”, CERN-2012-007, CERN, Geneva, Switzerland, (2012).
- [13] E. Jensen et al., “Normal Conducting CLIC Technology”, CLIC Note 641, CERN-AB-2005-056, CERN, Geneva, Switzerland, (2005).
- [14] H. Braun, et al., “CLIC 2008 parameters”, CERN-OPEN-2008-021, CLIC-Note-764, CERN, Geneva, Switzerland, (2008).
- [15] H. Wiedemann, “Particle accelerator physics”, 3rd edition, Springer-Verlag, ISBN 978-3540490432, Berlin, Germany, (2007).
- [16] P. Kowina, W. Kaufmann, et al., “Optimisation of Shoe-box type beam position monitors using the finite element methods”, POM033, DIPAC 2005, Lyon, France (2005).
- [17] P. Forck, “Lecture notes on beam instrumentation and diagnostics”, http://www-bd.gsi.de/conf/juas/juas_script.pdf, JUAS, Archamps, France, January-March 2011.
- [18] F. Hinode, H. Hayano et al., “A beam test of button type beam position monitor for the ATF damping ring”, IEEE trans., 4, pp 2604, (1996).
- [19] D. M. Pozar, “Microwave engineering”, 3rd edition, ISBN 978-0470009826, John Wiley & Sons, USA, (2005).

-
- [20] P. R. Carmel, G. D. Colef, R. L. Camisa, “Introduction to electromagnetic and microwave engineering”, ISBN 978-0471177814, John Wiley & Sons, USA, (1998).
- [21] A. Lyapin, PhD thesis: “Beam position monitor for TESLA spectrometer”, Technische Universität Berlin, Berlin, Germany, (2003).
- [22] S. Walston, S. Boogert et al., “Performance of a high resolution cavity beam position monitor system”, Nuclear Instruments and Methods in Physics Research A, 578, pp 1, (2008).
- [23] V. Balakin, A Bazel et al., “Experimental results from a microwave cavity beam position monitor”, Proceedings of PAC’99, pp 461, New York, (1999).
- [24] V. Sargsyan, H.J. Schreiber et al., “Test measurement of a new TESLA cavity beam position monitor at the ELBE linac”, TESLA internal report, TESLA 2004-14, DESY, Germany, (2004).
- [25] M. Slater et al., “Cavity BPM system tests for the ILC energy spectrometer”, Nuclear Instruments and Methods in Physics Research A, 592, pp 201, (2008)
- [26] S. Boogert et al., “Cavity beam position monitor system for ATF2”, TUPC161, Proceedings of IPAC 2011, St. Sebastian, Spain, (2011).
- [27] H. Maesaka et al., “Development of the RF cavity BPM of XFEL/SPRING-8”, MOPD07, DIPAC 2009, Basel, Switzerland, (2009).
- [28] Y. Honda et al., “Development of a high-resolution cavity-beam position monitor”, PRST-AB, 11, 062801, (2008).
- [29] P. N. Burrows et al., “The FONT4 ILC intra-train beam-based digital feedback system prototype”, SLAC Publication, SLAC-PUB-12759, SLAC, USA, (2007).
- [30] T. Schilcher et al., “Global orbit feedback system for the SLS storage ring”, ICALEPCS, pp299, (1999).
- [31] T. O. Raubenheimer “Estimates of emittance dilution and stability in high-energy linear accelerators”, PRST-AB, 3, 121002, (2000).
- [32] Kiyoshi Kubo, “Estimation of orbit change and emittance growth due to random misalignment in long linacs”, PRST-AB, 14, 014401, (2011).

-
- [33] C. E. Adolphsen “Beam-based alignment technique for the SLC linac”, SLAC-PUB-4902, SLAC, USA, (1989).
- [34] J. Niedziela , C. Montag, and T. Satog “Quadrupole beam-based alignment at RHIC”, Proceedings of the 2005 Particle Accelerator Conference, pp 3493, Knoxville, USA, (2005).
- [35] G. R. White et al., “Beam-based alignment, tuning and beam dynamics studies for the ATF2 extraction line and final focus system”, MOPP039, Proceedings of EPAC08, Genoa, Italie, (2008).
- [36] S.R. Smith et al., “Commissioning and Performance of LCLS Cavity BPMs”, proceedings of PAC09, pp 754, (2009).
- [37] ATF Collaboration, “ATF2 proposal”, Vol 1 & 2, KEK, Japan, (2006).
- [38] “Final focus test beam, project design report”, SLAC-376, Stanford University, California, USA, (1991).
- [39] X. J. Wang et al., “Challenges for operating a photo-cathode RF gun injector”, TH4043, LINAC98, Chicago, USA, (1998).
- [40] S. Takeda et al., “Status of 1.54 GeV ATF Linac”, proceedings of PAC97, 1, pp 587, Vancouver, Canada, (1997).
- [41] K. Kubo et.al., “Beam development in ATF damping ring”, MOP03D, EPAC98, Stockholm, Sweden, (1998).
- [42] J. Urakawa et al., “KEK/ATF damping ring”, proceedings of PAC97, 1, pp 444, Vancouver, Canada, (1997).
- [43] T. Naito et al., “Timing system for multi-bunch/multi-train operation at ATF-DR”, ATF internal report.
- [44] A. Seryi et al., “ATF2 commissioning”, SLAC-PUB-13765, SLAC, California, USA (2009).
- [45] J. Alabau-Gonzalvo, C. Blanch Gutierrez et al., “Optical transition radiation system for ATF2”, SLAC-PUB-14566, SLAC, California, USA, (2012).

-
- [46] L. Deacon, S. Boogert et al., “ATF extraction line Laser-wire system”, THOAC01, proceedings of PAC07, Albuquerque, USA, (2007).
- [47] T. Yamanaka et al., “Status of the first commissioning of the Shintake monitor for ATF2”, TH6REP062, proceedings of PAC09, Vancouver, Canada, (2009).
- [48] R.J. Collier and A.D. Skinner, “Microwave measurements”, 3rd edition, IET, ISBN 978-0863417351, Herts, UK, (2007).
- [49] B. Razavi, “RF microelectronics”, ISBN 0138875715, Prentice hall PTR, NJ, USA, (1998).
- [50] L. B. Jackson, “Digital filters and signal processing”, 3rd edition, ISBN 978-1441951533, Springer, (1995).
- [51] Guido van Rossum, “Python tutorial, Release 2.7.3”, Python Software Foundation, March 2013.
- [52] J. Irwin, C. X. Wang et al., “Model-Independent Beam Dynamics Analysis”, Physical Review Letter, 82, pp 1684, (1999).
- [53] W. H. Press, et al., “Numerical recipes in C: The art of scientific computing”, 2nd edition, ISBN 978-0521431088, Cambridge University Press, UK, (1992).
- [54] NLS team et.al., “New Light Source (NLS) Project: Conceptual design report”, <http://www.newlightsource.org/documents/NLS%20CDR%20Consolidated%20Final.pdf>, STFC, UK, (2010).
- [55] M. W. Poole, J. A. Clarke, et al., “Evolution of the Diamond Light Source”, TUODF102, EPAC, Viena, Austria, (2000).
- [56] “<http://www.diamond.ac.uk/Home/Science.html>”, Retrieved in September 2011.
- [57] “<http://www.diamond.ac.uk/Home/Technology.html>”, Retrieved in September 2011.
- [58] C. Cristou et.al., “The pre-injector linac for the DIAMOND Light Source”, MOP21, LINAC, Lubeck, Germany, (2004).

-
- [59] V. C. Kempson et.al., “Commissioning of the booster synchrotron for the DIAMOND Light Source”, THPLS029, EPAC, Edinburgh, Scotland, (2006).
- [60] B. Singh et.al., “Beam dynamics effect of insertion devices at DIAMOND storage ring”, THPE088, IPAC10, Kyoto, Japan, (2010).
- [61] R. P. Walker et.al., “Commissioning and status of the DIAMOND storage ring”, TUYMA03, APAC’07, Indore, India (2007).
- [62] R. Bartolini et.al. “Turn-by-turn data acquisition and post-processing for the diamond booster and storage ring”, TUPCH044, EPAC, Edingburgh, (2006).
- [63] T. Blacker et al., “CUBIT 13.1 User Documentation”, Computational Simulation Infrastructure Department (Org. 1543), Sandia National Laboratories.
- [64] W. Bruns, “GdfidL v2.1: Syntax and Semantics”, (2010).
- [65] K. Ko et al, “Advances in Parallel Electromagnetic Codes for Accelerator Science and Development”, SLAC-PUB-14349, SLAC, California, USA, (2010).
- [66] R. Lee, K. N. Sjobaek et al., “<https://confluence.slac.stanford.edu/display/AdvComp/ACDTool>”, workshop material, CW10, (2010).
- [67] Lie-Quan Lee, “Omega3P: A Parallel Finite-Element Eigenmode Analysis Code for Accelerator Cavities”, SLAC-PUB-13529, SLAC, California, USA, (2009).
- [68] “ParaView User’s Guide”, http://paraview.org/Wiki/ParaView/Users_Guide/Table_of_Contents, Retrieved on 14 September, 2012).
- [69] A. Morgan et al., “Simulation of a cavity BPM for high resolution single pass beam position measurements”, TUPSM026, BIW 10, Santa Fe, New Maxiko, USA, (2010).
- [70] Rohde & Schwarz International, “RS-ZVB20 data-sheet and Operation manual”, (2010).
- [71] National Instruments Corporation, “LabVIEW 8.2 Help”, NI Part Number 371361B-01, August 2006.
- [72] Edward Ginzton. “Microwave Measurements”, pp 448, McGraw-Hill, (1957).